TECHNISCHE
UNIVERSITÄT
WIEN

Institut für Energiesysteme
und Elektrische Antriebe

DIPLOMARBEIT

Design and Characterization of a high-speed Active Magnetic Bearing System

ausgeführt zur Erlangung des akademischen Grades eines
Diplom-Ingenieurs (Dipl.-Ing.) am

Institut für Energiesysteme und Elektrische Antriebe,
Fakultät für Elektrotechnik und Informationstechnik
der Technischen Universität Wien

unter der Anleitung von

O.Univ.Prof. Dipl.-Ing. Dr.techn. Manfred Schrödl
Dipl.-Ing. Dr.techn. Markus Hutterer, BSc
Dipl.-Ing. Dr.techn. Dominik Wimmer, BSc

durch

Markus Sonnleitner
Matr.Nr. 0326193
1040, Wien

Wien, 22.05.2025

Für Sabine, Aurelia, und Jonathan

Acknowledgement

Die Diplomarbeit ist das Ergebnis zahlreicher Ideen, Gespräche und wertvoller Diskussionen.
Mein besonderer Dank gilt O.Univ.-Prof. Dipl.-Ing. Dr. techn. Manfred Schrödl, der die Durchführung dieser Diplomarbeit am Institut für Energiesysteme und Elektrische Antriebe ermöglicht hat.
Für die Idee und die wissenschaftliche Unterstützung im Bereich der Rotordynamik danke ich Dipl.-Ing. Dr. techn. Markus Hutterer, BSc. Dank seiner fachlichen und persönlichen Kompetenz war es mir überhaupt erst möglich, in dieses Fachgebiet einzusteigen.
Ich darf Dipl.-Ing. Dr. techn. Dominik Wimmer, BSc, für die vielen Anregungen und Diskussionen danken. Insbesondere seine Erfahrung in den Bereichen Firmware, Leistungselektronik und Sensorik war während des Designs und des praktischen Aufbaus sehr wertvoll.
Ein großer Dank ergeht auch an Thomas Hufnagel. Er hat in der Institutswerkstätte exzellente Arbeit geleistet und mir wertvolle Anregungen für das Design des mechanischen Aufbaus gegeben.

Mein ganz persönlicher Dank ergeht an meine Familie für die Unterstützung und vor allem für die Geduld, die sie mir entgegengebracht hat.

Kurzfassung

Aktive Magnetlager nutzen geregelte elektromagnetische Kräfte, um Rotorwellen ohne jeglichen physischen Kontakt zu lagern. Im Vergleich zu herkömmlichen Lagern bieten aktive Magnetlager bei Hochgeschwindigkeitsanwendungen Systemvorteile. Der berührungslose Betrieb macht Verschleiß und Schmierung überflüssig und minimiert die Reibung. Daher haben sich diese Lager in kommerziellen Anwendungen wie Turbokompressoren, Schwungrad-Energiespeichersystemen und Turbomolekularpumpen bewährt. Aufgrund ihrer inhärenten Instabilität müssen aktive Magnetlager jedoch zur Stabilisierung in einen Regelkreis integriert werden, was die Komplexität und Baugröße dieser Systeme erhöht. Darüber hinaus kann der Betrieb von Hochgeschwindigkeitsmaschinen eine Herausforderung darstellen und erfordert die Implementierung fortschrittlicher Regelalgorithmen.

Diese Arbeit konzentriert sich auf den Entwurf und die experimentelle Validierung eines Prüfstands für ein aktives Magnetlagersystem, um eine Plattform für zukünftige Untersuchungen zu Rotordynamikeffekten und fortschrittlichen Regelalgorithmen zu schaffen. Der Schwerpunkt liegt dabei insbesondere auf einem möglichst modularen Prüfstand, um Flexibilität für unterschiedliche Forschungsziele zu erreichen. Bei der Konstruktion, dem Layout und der Ausrichtung der einzelnen Komponenten werden mechanische und elektromagnetische Aspekte berücksichtigt. Die Herausforderung besteht darin, nicht nur eine einwandfreie Funktionalität zu erreichen, sondern auch ein möglichst lineares Systemverhalten zu gewährleisten. Dies ermöglicht den Einsatz einfacher, linearer Regelalgorithmen zur Stabilisierung der Rotorwelle.

Eine begleitende Validierung stellt sicher, dass das Magnetlager die gewünschten Anforderungen erfüllt und eine Übereinstimmung mit dem mathematischen Modell gegeben ist. Dabei wird insbesondere auf die Kraft-Strom- und Kraft-Weg-Eigenschaften des aktiven Magnetlagers geachtet. Die Funtionalität des Prüfstandes wird anhand einer ersten modellbasierten Positionsregelung für die Rotorwelle gezeigt.

Dafür werden Messungen mit der schwebenden Rotorwelle durchgeführt. Die Messung der Ausgangssensitivität zeigt, dass eine robuste Positionsregelung einer beispielhaften Rotorwelle mit einfachen, linearen Regelstrukturen möglich ist.

Abstract

Active magnetic bearings use controlled electromagnetic forces to support rotor shafts without any physical contact. Compared to conventional bearings, active magnetic bearings offer system advantages in high-speed applications. The contact-free operation eliminates wear, the need for lubrication and minimizes friction. Therefore, these bearings have proven successful in commercial applications such as turbo compressors, flywheel energy storage systems, and turbomolecular pumps. However, due to their inherent instability, active magnetic bearings must be integrated into a control loop for stabilization, increasing the complexity and size of these systems. Additionally, operating high-speed machines can be challenging and requires the implementation of advanced control algorithms.

This thesis focuses on designing and experimentally validating a test stand of an active magnetic bearing system to provide a platform for future investigations on rotor dynamic effects and advanced control algorithms. In particular, the emphasis is also on a test stand that is as modular as possible in order to achieve flexibility for different research objectives. The design, layout, and alignment of the individual components will take mechanical and electromagnetic aspects into account. The challenge is to not only achieve flawless functionality but also to ensure a system behavior as linear as possible. This enables the use of simple, linear control algorithms to stabilize the rotor shaft. Accompanying validation ensures that the magnetic bearing meets the desired requirements and corresponds to the mathematical model. In particular, attention is paid to the force-current and force-displacement characteristics of the active magnetic bearing. Additionally, a mathematical model of the rotor is created, and model-based position control is implemented.

Finally, measurements are taken with the levitating rotor shaft. Notably, measuring the output sensitivity shows that robust position control of an exemplary rotor shaft is possible with simple, linear control structures.

Contents

Acronyms

ADC	analog digital converter
AMB	active magnetic bearing
BLDC	brushless DC motor
CAD	computer-aided design
COG	center of gravity
DOF	degree of freedom
DSP	digital signal processor
EMF	electromotive force
FEM	finite element method
FOC	field-oriented control
IM	induction machine
ISO	International Organization for Standardization
MIMO	multiple input multiple output
MTPA	maximum torque per ampere
PD	proportional-derivative
PI	proportional-integral
PMSM	permanent magnet synchronous machine
PWM	pulse width modulation
RPM	revolutions per minute
SCI	serial communications interface
SISO	single input single output
SynRM	synchronous reluctance machine

1 Introduction

Active magnetic bearings are a non-contact bearing system that uses actively controlled electromagnetic forces to suspend and stabilize rotors. Unlike conventional ball, roller or sliding bearings, active magnetic bearings eliminate physical contact and thus friction, wear and the need for lubrication. This opens up a whole new range of applications where the use of greases would be undesirable or impossible. These include medical devices and operation in clean rooms, high vacuum, extreme temperatures, and aggressive or high purity process gases. Active magnetic bearings are also essential for high-speed machines such as turbo compressors, flywheel energy storage systems and turbomolecular pumps.

The main disadvantage of active magnetic bearings compared to conventional ball bearings is their inherent instability. Therefore, active magnetic bearings must be integrated into a control loop for stabilization, which increases the system's complexity. The basic active magnetic bearing system consists of position sensors, a control unit, power amplifiers, and electromagnetic actuators, arranged around the rotor shaft (see Figure 1.1). The controller processes the sensor feedback of the rotor shaft displacement. The coil currents act as control variables, generating magnetic forces that center the rotor shaft and suppress external disturbances.

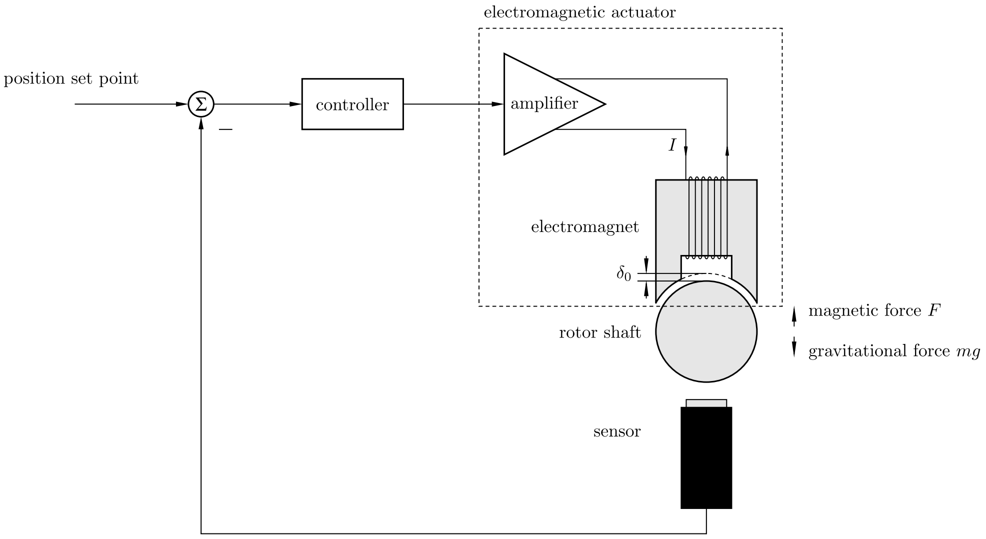

Figure 1.1: Basic position feedback control loop for an active magnetic bearing system.

Operating high-speed machines can be challenging because the gyroscopic effect and unbalance forces of the rotor shaft increase with rising rotor speeds [1]. This requires advanced control strategies and unbalance compensation.

The main objective of this thesis is the design and characterization of a test stand for the analysis of rotor dynamic effects in the high-speed range. The main specifications of the test stand are:

rotor speed	20 000 to 30 000 rpm
maximum rotor shaft weight	$\leq 5\,\mathrm{kg}$
total static load capacity	$\geq 50\,\mathrm{N}$
use of safety extra low voltage	$\leq 60\,\mathrm{VDC}$

The test stand will be designed from scratch with a modular structure to allow for easy modification. This will enable the test stand to adapt to different requirements. Since the individual components interact with each other, they must be selected and engineered to optimize the performance of the complete system and to meet the required specifications. Additionally, the rotor shaft should be stabilizable with simple linear control structures. This means, that the electromagnetic actuator and sensors should exhibit nearly linear behavior. The development of the drive unit is relatively straightforward because it builds on the research group's previous work [2]. However, the topology and arrangement of the active magnetic bearings are not specified yet, and the goal is to obtain a nearly linear force-current characteristic and an optimal interaction with the position sensors. Commercially available eddy current sensors are used as position sensors. However, the question arises as to whether the use of these sensors is possible with the desired rotor shaft design (which does not include position sensor target discs) in terms of the required linearity, and what adjustments to the measurement signals are necessary.

In addition to the mechanical design, electronics are also being developed to control the test stand and adjust the rotor speed. For the final characterization and accompanying validation of the design, it is also necessary to develop a firmware. This lays the groundwork for implementing advanced control algorithms and unbalance compensation in future studies.

The thesis is structured as follows: Chapter 2 briefly summarizes the fundamentals, required for active magnetic bearing engineering and the position controller synthesis. The design of the drive unit, the magnetic bearing, the mechanical structure, and the hardware and firmware architecture are described in Chapter 3. The magnetic bearing design is validated by comparing calculations, simulations, and measurements of several performance characteristics. In Chapter 4, the final measurements with the levitating rotor are summarized. These measurements are intended to evaluate the design. Chapter 5 concludes this thesis and a short outlook is given.

2 Fundamentals

The purpose of this introductory chapter is to provide the reader with the basic principles that are considered essential for understanding the remainder of the work.

Both, the active magnetic bearing and the drive unit of the test stand utilize the *Reluctance Force*. Therefore, the electromagnetic fundamentals of reluctance force generation are derived from the Maxwell stress tensor and the magnetic field's energy gradient.

Due to the nonlinear and unidirectional nature of the reluctance force, a special actuator topology is required in active magnetic bearings. The section on *Reluctance Actuators* explains how double reluctance actuators overcome those drawbacks. This creates an unidirectional force that is approximately linear around a specific operating point.

The section *Development of Active Magnetic Bearings* discusses the development and different structures of active magnetic bearings. The integration of active magnetic bearings into a control loop is also briefly demonstrated.

Finally, the basic principles of *Rigid Rotor Dynamics* are outlined. These dynamics are important for controller design and allow the active magnetic bearing to be integrated into a mechatronic system.

2.1 Reluctance Force

Magnetic bearings apply forces of magnetic origin to support bodies without the need for contact. Unlike alternative actuation methods, including Lorentz actuators and piezoelectric devices, reluctance actuators offer several distinct advantages. In particular, their high force density makes them ideal for integration into complex mechatronic systems where robust performance and precise control are essential [3].

Reluctance-based actuation has a wide range of applications. Initial studies of electromagnetic relays and reluctance motors laid the groundwork for establishing design principles and performance benchmarks. Recent advances in materials science, control theory, and power electronics have significantly improved the performance and reliability of these actuators [1].

The magnetic bearings of this test stand will use reluctance-based forces due to the high power density.

The following subsections describe two possible approaches to the analytical derivation. First, the focus is on the force exerted on bodies by the Maxwell stress tensor. Second, the derivation of the force from the magnetic field's energy gradient is demonstrated.

2.1.1 Maxwell Stress Tensor

The following derivation of the reluctance force is based upon [4] and [5]. There, a detailed derivation of the force exerted on bodies in a magnetic field is presented. This section focuses on the key points and results. The starting point is the global balance equation of the momentum for a spatially stable volume $\mathscr{V}$, which reduces to a conservation equation for the whole system:

$$-\dot{\mathbf{G}}(\mathscr{V}) = \mathbf{P}(\partial\mathscr{V}). \tag{2.1}$$

Equation 2.1 postulates that the rate of decline of the momentum content $\mathbf{G}(\mathscr{V})$ over time is equivalent to the momentum flow $\mathbf{P}(\partial\mathscr{V})$ through the envelope of $\mathscr{V}$, i.e. $\partial\mathscr{V}$.

Substituting the global quantities for the integral forms of the density, while making sure that the envelope $\partial\mathscr{V}$ is completely inside the material-free region, results in the local expression of the conservation equation. The rate of change of the total momentum of the body over time is also known as the resulting force $\mathbf{F}_\mathrm{R}$ acting on the body

$$\dot{\mathbf{G}}(\mathscr{V}) = \frac{\mathrm{d}}{\mathrm{d}t}\int\limits_{\mathscr{V}} \rho_\mathrm{m}\mathbf{v}\,\mathrm{d}V = \mathbf{F}_\mathrm{R} = -\int\limits_{\partial\mathscr{V}} \mathbf{n}\cdot\underset{\sim}{\boldsymbol{p}}^\mathrm{e}\,\mathrm{d}A = -\mathbf{P}(\partial\mathscr{V}) \tag{2.2}$$

with the mass density of the body ρ_m, the velocity field $\mathbf{v}$, the second-level tensor $\underset{\sim}{\boldsymbol{p}}^e$ of the pulse flux density (Maxwell stress tensor), and the normal vector $\mathbf{n}$ to the infinitesimally small area $\mathrm{d}A$, which is part of the entire envelope $\partial\mathscr{V}$.

This thesis considers magnetic field strengths to be more important than electric field strengths. In this so-called dominant magnetic field system, the integrand from (2.2) is given by

$$\mathbf{n}\cdot\underset{\sim}{\boldsymbol{p}}^\mathrm{e} = \frac{1}{\mu_0}\left[\frac{1}{2}B^2\mathbf{n} - (\mathbf{n}\cdot\mathbf{B})\mathbf{B}\right], \tag{2.3}$$

with the vector of the magnetic flux density $\mathbf{B}$ and the permeability of free space μ_0. The force of electromagnetic origin on a body (for a dominant magnetic field system) can be determined solely from the magnetic field $\mathbf{B}$ at a suitably chosen envelope $\partial\mathscr{V}$. The term has been chosen to make it clear that $\partial\mathscr{V}$ must extend entirely through empty space and encompass only the body of interest. In fact, it may coincide with the body's surface.

Figure 2.1a illustrates the basic field configuration with two bodies. Regardless of the origin of the magnetic field $\mathbf{B}_\mathrm{g}$, a resulting force $\mathbf{F}_\mathrm{R}$ is observed between the two bodies.

The geometric interpretation of (2.3) is illustrated in Figure 2.1b. Projecting the Maxwell stress tensor $\underset{\sim}{\boldsymbol{p}}^\mathrm{e}$ onto the normal vector $\mathbf{n}$ of an infinitesimal surface reveals the force acting on that surface.

According to the boundary conditions of electrodynamics, the following conclusions can be drawn regarding the magnetic field strength $\mathbf{H}$,

$$\mathbf{n}\times(\mathbf{H}_2 - \mathbf{H}_1) = \mathbf{j}_\mathrm{S}, \tag{2.4}$$

where $\mathbf{H}_1$ and $\mathbf{H}_2$ denote the magnetic field strength in front of and behind the boundary, respectively. Therefore, at a boundary with normal vector $\mathbf{n}$, the tangential component of the magnetic field strength $\mathbf{H}$ across the boundary is discontinuous by an amount equal to the magnitude of the surface current density $\mathbf{j}_\mathrm{S}$. In the absence of a surface current density, the tangential component of the magnetic field strength is continuous

$$\mathbf{H}_1^{||} = \mathbf{H}_2^{||}. \tag{2.5}$$

It is important to consider the particular case of a boundary transition between air ($\mu_\mathrm{r} \approx 1$) and a highly permeable material ($\mu_\mathrm{r} \rightarrow \infty$[1]), as this occurs in both the drive unit and the magnetic bearing. The following discussion will explore this topic in more detail (see Figure 2.1a).

Within the boundaries of an ideally magnetically permeable body, the magnetic field strength undergoes a complete dissolution, resulting in a state where $\mathbf{H} \rightarrow \mathbf{0}$. From the Equation 2.5 and the material law ($\mathbf{B} = \mu_0 \mathbf{H}$) it can be concluded that the tangential components of the magnetic field strength and flux density at the surface of these bodies are zero. Therefore, the field lines of the magnetic flux density $\mathbf{B}$, are shown to be perpendicular to these bodies under all conditions[2].

This precondition has the effect that $\mathbf{n}$ and $\mathbf{B}$ are either parallel or antiparallel ($\mathbf{B} = \pm B\mathbf{n}$) at the surface of the body, which simplifies (2.3) to

$$\mathbf{n} \cdot \underset{\sim}{\boldsymbol{p}}^{\mathrm{e}} = -\frac{B^2}{2\mu_0}\mathbf{n}. \tag{2.6}$$

Consequently, this results in the simplification of (2.2) to the following form

$$\mathbf{F}_\mathrm{R} = \int\limits_{\partial \mathscr{V}} \frac{B^2}{2\mu_0}\mathbf{n}\,\mathrm{d}A. \tag{2.7}$$

The geometric interpretation implies that a unidirectional tensile stress is exerted along the magnetic flux tubes. To overcome this drawback and achieve bidirectional force, a special actuator topology is required. The Section 2.2 deals with the application of this force, which is generated at interfaces with different magnetic permeability and shows a commonly used topology [1].

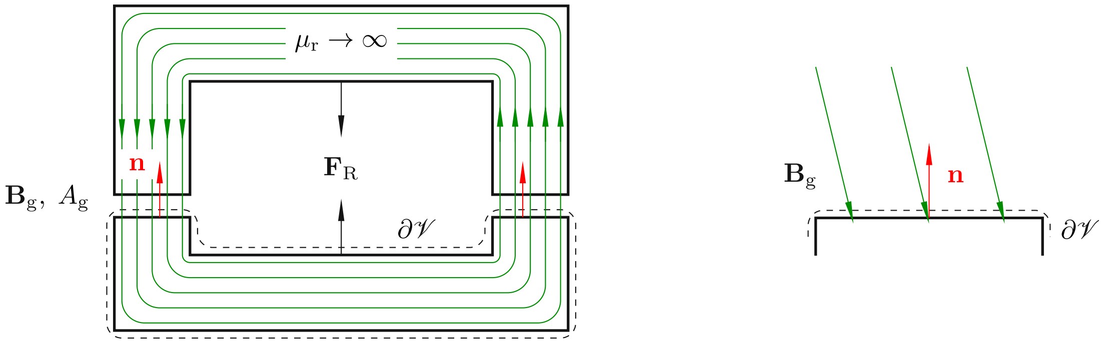

(a) Simple arrangement to visualise the effect of force in the magnetic field.

(b) Field conditions $\mathbf{B}_\mathrm{g}$ at the body surface $\partial\mathscr{V}$ for a general case.

Figure 2.1: Force effect on bodies in the dominant magnetic field system.

Neglecting the stray flux[3] and assuming a homogeneous magnetic flux density $\mathbf{B}_\mathrm{g}$ in the air gap, the

---

[1] In the present work, this approximation is made for all unsaturated materials.

[2] An ideally permeable body ($\mu_\mathrm{r} \rightarrow \infty$) is a prerequisite

[3] This approximation is usually permissible due to the small air gap lengths that occur in active magnetic bearing (AMB) applications.

integral in (2.7) is reduced to a multiplication by the (total) area of the air gap ($= 2A_\mathrm{g}$)

$$\mathbf{F}_\mathrm{R} = \frac{B_\mathrm{g}^2\, A_\mathrm{g}}{\mu_0}\mathbf{n}. \tag{2.8}$$

In addition, this equation allows a preliminary estimate of the actuator load capacity for a given maximum air gap flux density (saturation limit of the mover and/or stator).

2.1.2 Magnetic Field's Energy Gradient

Another approach to analytically derive the force $\mathbf{F}_\mathrm{R}$ in a reluctance actuator (see Figure 2.2) is based on the fact that the actuator's force output is directly related to the change in magnetic energy[4], stored in its magnetic circuit, as a function of the mover position. In the case of the actuator in Figure 2.2, which is considered as an inductor (with a dependence on the air gap length δ_g) and operating at constant current, the following derivation is commonly made

- the stored magnetic energy is expressed as a function of the inductance and current;
- the mechanical force corresponds to the derivative with respect to the degree of freedom;
- the inductance is related to magnetic reluctance and is differentiated accordingly.

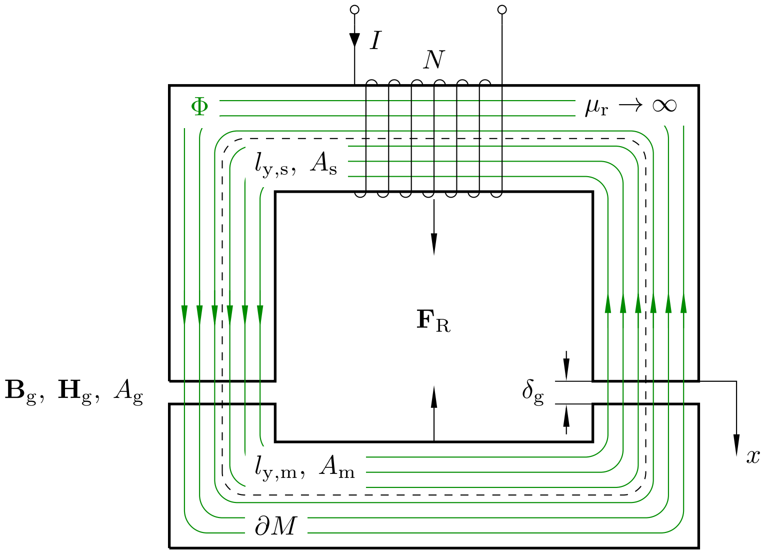

Figure 2.2: Schematic of a reluctance actuator (stator coil with N windings) to illustrate the force effect.

---

[4] In many derivations, it is convenient to use the concept of magnetic co-energy (which, for linear systems, is equal to magnetic energy) because it simplifies the derivation with respect to displacement.

2.1.2.1 Energy in the magnetic field

The energy stored in the magnetic field of a linear inductor, whose inductance is a function of displacement x, can be calculated in the following way[5]

$$E(x) = \frac{1}{2} I^2 L(x), \tag{2.9}$$

where

- $L(x)$ is the inductance, which is a function of the position x of the movable part, and
- I is the current through the coil.

2.1.2.2 Energy gradient

The force exerted on the moving part can be calculated by taking the derivative of the magnetic energy with respect to the displacement x. In particular, this gives the component of the force $\mathbf{F}_\mathrm{R}$ in the x-direction

$$F_\mathrm{R,x} = -\frac{\mathrm{d}}{\mathrm{d}x} E(x). \tag{2.10}$$

The negative sign in the equation reflects the fact that the force acts to reduce the reluctance and energy content of the magnetic field. Therefore, if the mover is displaced in the positive x-direction, the energy in the magnetic circuit increases at a constant magnetic flux of Φ and the force component $F_\mathrm{R,x}$ acts in opposition to this displacement.
Substituting the expression for $E(x)$ yields

$$F_\mathrm{R,x} = -\frac{\mathrm{d}}{\mathrm{d}x}\left[\frac{1}{2} I^2 L(x)\right] = -\frac{1}{2} I^2 \frac{\mathrm{d}}{\mathrm{d}x} L(x). \tag{2.11}$$

This equation shows that the force is directly proportional to the square of the current and the rate at which the inductance of the actuator changes with position. The concept of reluctance is now used to calculate the self-inductance of the actuator.

2.1.2.3 Hopkinson's Law

Hopkinson's Law is a fundamental principle in magnetic circuit analysis that plays a role analogous to Ohm's Law in electrical circuits. It facilitates the establishment of a relationship between the magnetic "driving force" and the magnetic flux passing through a circuit. This provides a simplified approach to understanding and designing devices that depend on magnetic fields. The fundamental principle of Hopkinson's Law is the establishment of a relationship between three key quantities in the context of magnetic circuits [3]:

---

[5] The fundamental relationship governing the energy stored in a magnetic field is derived from the work expended to establish that magnetic field.

- **Magnetomotive Force ($\mathscr{F}$):** This is the force that drives magnetic flux through a circuit, typically produced by an electric current flowing through coils. It can be compared to voltage in an electrical circuit.
- **Magnetic Flux (Φ):** The magnetic flux is comparable to the electric current that flows through an electrical circuit.
- **Magnetic Reluctance ($\mathscr{R}$):** The opposition, or "resistance", to the creation of magnetic flux in a given material or circuit is analogous to the concept of electrical resistance.

Mathematically, Hopkinson's Law is expressed as

$$\Phi = \frac{\mathscr{F}}{\mathscr{R}}, \tag{2.12}$$

with the magnetomotive force being defined by Ampère's law

$$\mathscr{F} = \oint\limits_{\partial M} \mathbf{H} \cdot \mathrm{d}\mathbf{l} = NI. \tag{2.13}$$

The interpretation of the equation can be observed in Figure 2.2. The integration of the magnetic field strength's component in path direction is to be performed along the area's edge ∂M (dashed line), including all windings (N). The reluctance is defined as

$$\mathscr{R} = \frac{l_\Phi}{\mu A_\Phi}, \tag{2.14}$$

with the material's permeability $\mu = \mu_0 \mu_\mathrm{r}$[6], the length of the magnetic path l_Φ, and the cross-sectional area of the magnetic core A_Φ[7].

The composition of magnetic circuits is such that they generally consist of sections that vary in cross section, length, and permeability. This phenomenon results in a network of reluctances and sources for calculating the unknown fluxes.

As shown by the simple example in Figure 2.2, accurate calculation of the individual reluctance components can be challenging. Straight sections with homogeneous and orthogonal field distribution with respect to the cross section can be calculated easily. However, in the corners it is necessary to know the exact field distribution in order to calculate their reluctance.

If the "corner effect" is neglected[8], this will result in the total reluctance of the magnetic circuit shown in Figure 2.2

$$\mathscr{R} = \mathscr{R}_\mathrm{m} + \mathscr{R}_\mathrm{s} + \mathscr{R}_\mathrm{g} = \frac{l_\mathrm{y,m}}{\mu_0 \mu_\mathrm{r} A_\mathrm{m}} + \frac{l_\mathrm{y,s}}{\mu_0 \mu_\mathrm{r} A_\mathrm{s}} + \frac{2\delta_\mathrm{g}}{\mu_0 A_\mathrm{g}}. \tag{2.15}$$

As previously mentioned, it is reasonable to suppose that the paths within the ferromagnetic material are magnetically ideal conducting ($\mu_\mathrm{r} \to \infty$, $\mathscr{R} \to 0$), which simplifies Equations 2.13 and 2.15

$$\mathscr{F} = NI \approx H_\mathrm{g} 2\delta_\mathrm{g} \tag{2.16}$$

---

[6] In this thesis, the ferromagnetic circuits of the magnetic bearings are usually operated below their saturation limit. Therefore, the assumption that $\mu_\mathrm{r} \to \infty$ is a reasonable approximation. This causes the reluctance of these sections to disappear completely.

[7] Strictly speaking, this is the cross section that is perpendicular to the flux [3].

[8] It is hypothesized that the increased path length is offset by the increased cross section.

$$\mathscr{R} \approx \mathscr{R}_{\mathrm{g}} = \frac{2\delta_{\mathrm{g}}}{\mu_0 A_{\mathrm{g}}}. \tag{2.17}$$

The calculation of the magnetic flux Φ, is derived from the results presented in (2.12)

$$\Phi = B_{\mathrm{g}} A_{\mathrm{g}} \approx \frac{NI}{\mathscr{R}_{\mathrm{g}}} = \frac{NI\mu_0 A_{\mathrm{g}}}{2\delta_{\mathrm{g}}}. \tag{2.18}$$

The self-inductance of the actuator is defined as the proportionality factor between the current I and the resulting linkage flux, given by the equation $\Psi = N\Phi$

$$\Psi = N\Phi \approx I\frac{N^2\mu_0 A_{\mathrm{g}}}{2\delta_{\mathrm{g}}} \tag{2.19}$$

$$L(x) \approx \frac{N^2\mu_0 A_{\mathrm{g}}}{2x} = \frac{N^2}{\mathscr{R}_{\mathrm{x}}}, \quad L(x)\Big|_{x=\delta_{\mathrm{g}}} \approx \frac{N^2\mu_0 A_{\mathrm{g}}}{2\delta_{\mathrm{g}}} = \frac{N^2}{\mathscr{R}_{\mathrm{g}}}. \tag{2.20}$$

Equation 2.20 shows how the inductance of the magnetic circuit is related to its reluctance. Taking the derivative of the inductance with respect to the variable x gives the following equation

$$\frac{\mathrm{d}}{\mathrm{d}x}L(x) = \frac{\mathrm{d}}{\mathrm{d}x}\left(\frac{N^2}{\mathscr{R}_{\mathrm{x}}}\right) = -\frac{N^2}{\mathscr{R}_{\mathrm{x}}^2}\frac{\mathrm{d}\mathscr{R}_{\mathrm{x}}}{\mathrm{d}x}. \tag{2.21}$$

Substituting this back into the force expression and differentiating the reluctance with respect to the displacement in x-direction, we get

$$F_{\mathrm{R,x}} = \frac{1}{2}I^2\frac{N^2}{\mathscr{R}_{\mathrm{x}}^2}\frac{\mathrm{d}\mathscr{R}_{\mathrm{x}}}{\mathrm{d}x} = \left(\frac{NI}{x}\right)^2\frac{\mu_0 A_{\mathrm{g}}}{4}, \tag{2.22}$$

and with the air gap from Figure 2.2 ($x = \delta_{\mathrm{g}}$)

$$F_{\mathrm{R,x}}\Big|_{x=\delta_{\mathrm{g}}} = \left(\frac{NI}{\delta_{\mathrm{g}}}\right)^2\frac{\mu_0 A_{\mathrm{g}}}{4}. \tag{2.23}$$

In practice, this derivation assumes that the magnetic materials are linear and ignores effects such as saturation and fringing. In more sophisticated models, the presence of nonlinear material properties and complex geometries may require the implementation of numerical methods or corrections to this basic analysis.

The verification of this hypothesis can be easily achieved by formulating the magnetic energy in integral form. First, the magnetic energy density u at a given point in the magnetic field is calculated by integrating the magnetic field strength $\mathbf{H}$ over the flux density $\mathbf{B}$

$$u = \int_0^{B_{\mathrm{xyz}}} \mathbf{H}\cdot\mathrm{d}\mathbf{B}. \tag{2.24}$$

In the case of a linear medium ($\mathbf{H} = \mathbf{B}/\mu_0$ for free space or $\mathbf{H} = \mathbf{B}/(\mu_0\mu_{\mathrm{r}})$ in a magnetic material with constant relative permeability μ_{r}), this integral yields the well-known quadratic dependence, which for free space leads to the following equation

$$u = \frac{1}{2}\frac{B_{\mathrm{xyz}}^2}{\mu_0} = \frac{1}{2}H_{\mathrm{xyz}}^2\mu_0. \tag{2.25}$$

Integrating this energy density over the total volume V_Φ in which the magnetic field exists yields the total magnetic energy [3]

$$E = \int_0^{V_\Phi} \frac{1}{2}\frac{B_{\mathrm{xyz}}^2}{\mu_0}\,\mathrm{d}V. \tag{2.26}$$

Referring to Figure 2.1a and 2.2, it is evident that under the aforementioned assumption ($\mu_\mathrm{r} \to \infty$), the ferromagnetic material itself does not store magnetic energy. Instead, it is stored in the two air gaps, as outlined by Prechtl in [4]. Assuming a homogeneous magnetic flux density $\mathbf{B}_\mathrm{g}$ in the air gap, the total stored magnetic energy is given by (2.26)

$$E(x) = \frac{1}{2}\frac{B_\mathrm{g}^2}{\mu_0}A_\mathrm{g}2x = \frac{\mu_0 A_\mathrm{g}}{4x}(NI)^2 = \frac{1}{2}I^2\frac{N^2\mu_0 A_\mathrm{g}}{2x} = \frac{1}{2}I^2L(x). \tag{2.27}$$

The equivalence with the assumptions presented in (2.9) is emphasised by this.

2.2 Reluctance Actuators

Reluctance actuators are central components within magnetic bearing systems, responsible for generating the forces, required to suspend and control a rotor without the need for mechanical contact. The primary function of these components is to generate a magnetic flux across a narrow air gap, which then interacts with the rotor to generate stabilizing forces.

Magnetic bearings are designed to provide high, controllable forces with low losses and precise force generation. The design of these systems relies on the appropriate selection and arrangement of magnetic materials, the optimisation of magnetic circuits and the use of techniques such as differential drive/winding and permanent magnet biasing to achieve the desired performance in AMB systems.

2.2.1 Double Reluctance Actuator

In many precision mechatronic applications, a single reluctance actuator - where $F \propto I^2$ and $F \propto x^{-2}$ - suffers from unidirectional force and strong nonlinearity, as already derived in (2.22). The double reluctance actuator overcomes these limitations by pairing two identical reluctance elements on either side of a common mover, with currents I_1 and I_2 in their coils (see Figure 2.3).

Equation 2.22 can now be utilised to calculate the resulting force on the moving part

$$F_{\mathrm{R,x}} = F = F_1 - F_2 = \left(\frac{NI_1}{\delta_1}\right)^2\frac{\mu_0 A_\mathrm{g}}{4} - \left(\frac{NI_2}{\delta_2}\right)^2\frac{\mu_0 A_\mathrm{g}}{4} = \frac{N^2\mu_0 A_\mathrm{g}}{4}\left(\frac{I_1^2}{\delta_1^2} - \frac{I_2^2}{\delta_2^2}\right). \tag{2.28}$$

The key features of this double reluctance actuation are the following [3]:

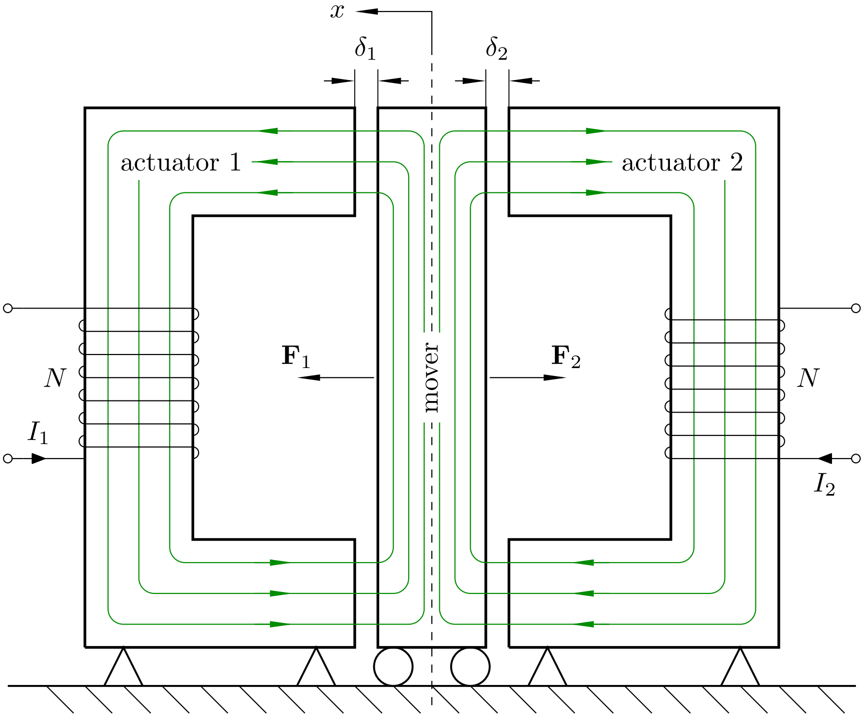

Figure 2.3: Double reluctance actuator (differential driving mode): the dual actuator (1 and 2) segments act in opposing directions on the pivotal movable element (mover), thereby generating a linear force to current ratio at the central position.

- **Differential operation for bidirectional linearity:** The introduction of a so-called bias current I_0 and a differential control current I_c with $I_1 = I_0 + I_c$ and $I_2 = I_0 - I_c$, leads to a simplification of the resulting force (Equation 2.28) with the mover in the center position ($\delta_1 = \delta_2 = \delta_0$):

$$F = \frac{N^2 \mu_0 A_g}{4} \left[\frac{(I_0 + I_c)^2 - (I_0 - I_c)^2}{\delta_0^2} \right] = \frac{N^2 \mu_0 A_g}{4} \left(\frac{4 I_0 I_c}{\delta_0^2} \right), \tag{2.29}$$

$$k_I = \frac{\mathrm{d}F}{\mathrm{d}I_c} = \frac{I_0 N^2 \mu_0 A_g}{\delta_0^2}. \tag{2.30}$$

  Thus, around the center position of the mover, $F \approx k_I I_c$ is a linear function of the differential current I_c - even though each half alone is quadratic in I.

- **Adjustable gain via bias current:** It has been shown that increasing I_0 increases the slope of the $F - I_c$ line (force-current factor k_I), hence the effective force constant k_I is proportional to the bias current I_0.

- **Zero net force at zero differential current:** In the case of $I_1 = I_2$ (i.e. $I_c = 0$) the two reluctance forces cancel exactly, resulting in $F = 0$. This symmetry allows true bidirectional actuation without the need for mechanical springs.

- **Residual nonlinearities and stiffness:** Away from the exact center, the smaller half-gap begins to dominate, and perfect linearity is no longer apparent.

  The assembly has an inherent negative stiffness, characterized by a tendency to exert a pulling force on the mover in one of two directions, toward one pole or the other. In order to mitigate this effect, it is essential to implement a stabilization process by means of feedback control.

- **Applications and control:** The double reluctance topology can deliver a linear, bidirectional force using just one control variable (I_c). This makes it easy to integrate into linear controllers, since extensive lookup tables or nonlinear compensators are not required. Such integration is particularly important where high force density is required over a reduced stroke length.

The actuator exhibits optimal linear behavior when $\delta_1 = \delta_2 = \delta_0$. If the mover is positioned off-center by a displacement of x, a more complex situation is obtained. Substituting $\delta_1 = \delta_0 - x$ and $\delta_2 = \delta_0 + x$ into the (2.28) results in the following equation

$$F = \frac{N^2 \mu_0 A_\mathrm{g}}{4} \left[\frac{(I_0 + I_\mathrm{c})^2}{(\delta_0 - x)^2} - \frac{(I_0 - I_\mathrm{c})^2}{(\delta_0 + x)^2} \right], \tag{2.31}$$

emphasizing the dependence of the force (and the force-current factor k_I) on the mover position.

The linearization of this equation around the operating point ($I_\mathrm{c} = 0,\ x = 0$) allows a simplified representation of the force and enables linear control strategies. The force-current factor, denoted by k_I (see Equation 2.30), and the force-displacement factor (or stiffness of the magnetic bearing), denoted by k_x, are of particular importance for the AMB design.

Equation 2.31 has to be differentiated with respect to the control current I_c and with respect to the displacement x. The evaluation at the operating point yields the factors k_I and k_x

$$\begin{aligned} k_\mathrm{I} &= \left[\frac{\partial}{\partial I_\mathrm{c}} F(I_\mathrm{c}, x) \right] \Bigg|_{I_\mathrm{c}=0,\ x=0} \\ &= \frac{N^2 \mu_0 A_\mathrm{g}}{4} \left\{ \frac{\mathrm{d}}{\mathrm{d}I_\mathrm{c}} \left[\frac{(I_0 + I_\mathrm{c})^2}{\delta_0^2} - \frac{(I_0 - I_\mathrm{c})^2}{\delta_0^2} \right] \right\} \Bigg|_{I_\mathrm{c}=0} \\ &= \frac{N^2 \mu_0 A_\mathrm{g}}{4} \left\{ \frac{2(I_0 + I_\mathrm{c})}{\delta_0^2} + \frac{2(I_0 - I_\mathrm{c})}{\delta_0^2} \right\} \Bigg|_{I_\mathrm{c}=0} \\ &= \frac{I_0 N^2 \mu_0 A_\mathrm{g}}{\delta_0^2} \end{aligned} \tag{2.32}$$

$$\begin{aligned} k_\mathrm{x} &= \left[\frac{\partial}{\partial x} F(I_\mathrm{c}, x) \right] \Bigg|_{I_\mathrm{c}=0,\ x=0} \\ &= \frac{N^2 \mu_0 A_\mathrm{g}}{4} \left\{ \frac{\mathrm{d}}{\mathrm{d}x} \left[\frac{I_0^2}{(\delta_0 - x)^2} - \frac{I_0^2}{(\delta_0 + x)^2} \right] \right\} \Bigg|_{x=0} \\ &= \frac{N^2 \mu_0 A_\mathrm{g}}{4} \left\{ \frac{2I_0^2}{(\delta_0 - x)^3} - \frac{-2I_0^2}{(\delta_0 + x)^3} \right\} \Bigg|_{x=0} \\ &= \frac{I_0^2 N^2 \mu_0 A_\mathrm{g}}{\delta_0^3} \end{aligned} \tag{2.33}$$

and this leads to the following important equation for an AMB

$$F\Big|_{x=0,\ I_\mathrm{c}=0} = \frac{\partial F(I_\mathrm{c},x)}{\partial I_\mathrm{c}} I_\mathrm{c} + \frac{\partial F(I_\mathrm{c},x)}{\partial x} x = k_\mathrm{I} I_\mathrm{c} + k_\mathrm{x} x. \tag{2.34}$$

2.2.2 Driving Mode and Linearization

The findings from the previous chapter (particularly Equation 2.34) show that combining a constant bias field with a control field and the suitable topology results in an almost linear, bidirectional force-current characteristic. This section examines the various methods of generating and combining the bias and control fields within a double reluctance actuator.

- **Differential (sum-and-difference) drive:** Two opposing pole pairs per axis are fed from two amplifier outputs (see Figure 2.3) carrying $I_1 = I_0 + I_\mathrm{c}$ and $I_2 = I_0 - I_\mathrm{c}$, with the constant bias current I_0 and the control variable I_c. The choice of I_0, which causes the bearings to operate at a preloaded point on the $F - I_\mathrm{c}$ parabola, combined with driving one coil with the sum and the opposite coil with the difference, results in an approximate linearity of the resulting force in I_c.
  The main drawback of this approach is the need for two amplifiers, a limitation that may be considered of minor importance due to advances in power electronics.
  The simplicity of the resulting magnetic circuit and winding arrangement makes this configuration the optimal design for the test stand[9] [1], [6].
- **Differential-winding bias:** Instead of using two separate amplifiers, each pole pair is equipped with a permanent "bias" winding (all in series, carrying I_0) in addition to a control winding (in series in pairs, carrying $\pm I_\mathrm{c}$). The combination of bias and control flux results in addition in one pole and subtraction in the opposite pole, thereby achieving a linearized $F - I_\mathrm{c}$ response with a single amplifier and a single DC current source. This approach is accompanied by increased copper losses compared to the differential drive mode, if $I_\mathrm{c} \neq 0$ [1], [6].
- **Permanent-magnet biasing:** The bias field is provided entirely by the permanent magnets (hybrid reluctance actuator); the control winding modulates this stored field to provide a bidirectional force around the permanent magnet set load point. This approach has been shown to effectively reduce bias-related losses, thereby increasing the efficiency of thermal management in high-power machines. Furthermore, the reluctance of the bias field is dominated by the permanent magnet itself when using a permanent magnet material with a relative permeability of approximately 1. It is evident that the inherent negative stiffness of the reluctance actuator is reduced in this configuration [3]. However, the mechanical design of the magnetic circuit is complex.

2.3 Development of Active Magnetic Bearings

Active magnetic bearings are an integral part of modern high-speed and high-performance machinery. The principle of contactless magnetic suspension was initially explored in the field of experimental physics,

---

[9] As will be demonstrated later, it is even possible to use the stator kit of a permanent magnet synchronous machine (PMSM) or induction machine (IM) for the magnetic bearing.

with its beginnings dating back to the mid-20th century. Conventional bearings have inherent limitations, including friction, wear, and the need for lubrication. As these limitations became more apparent, the potential benefits of a non-contact bearing system were recognized, leading to further research in this area. Initial implementations focused on basic electromagnetic configurations capable of supporting rotor systems by utilizing static magnetic fields. However, the integration of active control systems was a real breakthrough. The development of a AMB was made possible by advances in sensor technology, digital signal processing, and power electronics. These systems are designed to continuously monitor the rotor position and adjust the electromagnetic forces in real time, providing precise control of the rotor dynamics. This dynamic control has been shown to have two main functions. First, it has been shown to reduce vibration and instability. Second, it has been shown to allow for customizable stiffness and damping characteristics. These features greatly expand the range of possible applications. These applications include turbomachinery, flywheel energy storage, aerospace and high precision instrumentation [6] [1].

2.3.1 Types of Magnetic Bearings

2.3.1.1 Heteropolar magnetic bearings

Heteropolar magnetic bearings are a subset of active magnetic bearings in which the stator poles alternate in polarity in a given plane of rotation (for example, in a sequence such as -S-N-N-S-S-N-N-S-, see Figure 3.7b). This alternating configuration is similar to that used in conventional electric motor design, allowing the bearing to generate forces in two orthogonal radial directions. A notable advantage of a heteropolar structure is its simplicity and reduced cost, as it typically requires only a single stator lamination stack, thereby simplifying and reducing the economic burden of manufacturing.

However, due to the significant variation in the magnetic field experienced by the rotor as it rotates, heteropolar designs have been shown to have higher iron losses in the rotor. To minimize these losses, the rotor is therefore often constructed from laminated ferromagnetic sheets that are electrically insulated from each other. Conversely, homopolar bearings - where all poles in a plane of rotation have the same polarity - result in significantly reduced eddy current losses, a factor that is particularly important in applications such as vacuum systems where heat dissipation is limited, but at the cost of increased complexity and cost. The primary advantages of heteropolar magnetic bearings are a simplified and less expensive design due to the use of a single lamination stack, and improved integration with active control systems that have the ability to dynamically adjust stiffness and damping.

These trade-offs mean that while heteropolar bearings are often selected for their lower cost and simple design, designers must consider the additional eddy current losses in high-speed or thermally sensitive applications by ensuring appropriate rotor design and lamination [6] [1].

2.3.1.2 Homopolar magnetic bearings

Homopolar magnetic bearings are those in which all stator poles in a given plane of rotation have the same polarity (e.g., N-N-N-N), with the required polarity alternation occurring axially rather than circumferentially. This is in contrast to heteropolar bearings, where the poles alternate in a north-south direction around the rotor.

The key features of homopolar designs are reduced rotor losses and the straightforward implementation of permanent magnet biasing. The primary disadvantages associated with the proposed design are increased manufacturing costs and complex assembly.

In a variety of designs, the choice between heteropolar and homopolar configurations is ultimately determined by a balance between efficiency (rotor losses) and system complexity/cost. Homopolar structures are particularly effective in situations where low rotor heating is a priority, justifying their more complex design.[6] [1].

2.3.2 Magnetic Bearing as Mechatronic System

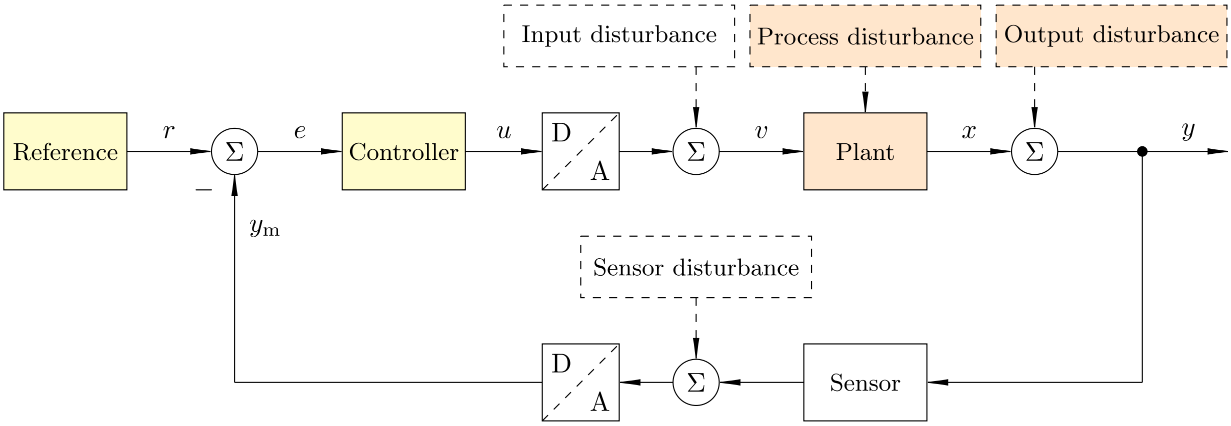

Figure 2.4: Minimal variant of an AMB control loop, emphasizing the mechatronic nature of these systems.

The interdisciplinary nature of magnetic bearing technology, which integrates electromagnetics, control theory, and mechanical design, has been essential to its success. Modern AMBs are considered advanced mechatronic devices in which the role of software is as critical as that of hardware components.

The fundamental element of the AMB functionality is an active control loop (see Figure 2.4): sensors monitor the rotor position y_m, which is compared with the reference signal r. The result is the control error e, which is then used by the controller to determine the necessary corrections via the control effort u. After the digital-to-analog conversion, the signal v is applied to the plant. The plant itself may be subject to some disturbance and consists of an amplifier, the magnetic bearing, and the rotor. The figure distinguishes between the rotor position x and the measured rotor position y to account for potential output disturbances. It is important to note that the analog sensor signal is also subject to unavoidable noise. This signal is converted from analog to digital and fed back, closing the feedback loop.

The color coding helps distinguish areas or blocks that exchange information (yellow) from those that exchange energy (orange).

This active control not only stabilizes the rotor, but also allows fine-tuning of the AMB's stiffness and damping characteristics, which are essential for managing vibration and improving overall performance. In addition, active magnetic bearings can compensate for potential rotor unbalance.

2.4 Eddy Current Effect

Eddy currents are only a minor aspect of this thesis. This section briefly describes their causes and possible countermeasures. They are important to understand the operating principle of the position sensors and the lamination process of the rotor packages.

2.4.0.1 Overview of eddy currents

Eddy currents are defined as loops of electric current induced in conductors by a varying magnetic field, according to Faraday's law of electromagnetic induction. These currents were found to flow in closed loops in planes perpendicular to the magnetic field. These loops are responsible for the creation of secondary magnetic fields, which in turn produce an counteracting effect to that of the original field.

2.4.0.2 Physical principles

According to Faraday's law, the temporal variation of magnetic flux through a conductive medium results in the induction of an electromotive force (EMF) within any closed loop present in the conductor. Lenz's Law states that the direction of the induced eddy current will be such that its own magnetic field will oppose the original flux change that created it.

2.4.0.3 Significance and effects, applications

Eddy currents have noticeable effects, including the generation of heat when they encounter the electrical resistance of the material. They also create magnetic drag forces that retard the motion of conductive materials and can cause unwanted energy dissipation in transformers and electrical machines unless special measures (e.g., lamination) are taken. At the same time, engineers have developed the expertise to utilize their properties for beneficial applications. These include smooth, wear-free braking systems on trains, industrial induction heaters, non-destructive testing equipment capable of detecting cracks beneath a metal surface, and distance sensors.

2.4.0.4 Measures to reduce eddy currents

First, the parameters affecting eddy currents must be identified.

- **Frequency:** Eddy current losses are proportional to the square of frequency. This is in contrast to the hysteresis loss, which increases linearly with frequency.
- **Flux density:** In this instance, too, a quadratic relationship is observed between flux density and eddy currents[10].
- **Resistivity:** The utilisation of magnetic materials with reduced conductivity, such as silicon steel, can effectively mitigate the formation of eddy currents.

---

[10] The frequency and flux density are typically predetermined by the application, with minimal or no scope for manipulation.

- **Lamination thickness:** An analytical approach shows that eddy current losses increase quadratically with sheet thickness. This is illustrated, for instance, in the work of Huang [7]. However, Bitsi et al. [8] were able to demonstrate that losses increase at a slightly lower rate than quadratically using 3D finite element method (FEM) simulations and field conditions equivalent to those of a salient pole synchronous machine rotor. In any case, to minimise core losses, it is necessary to ensure that the laminations are as thin as possible.

2.5 Rigid Rotor Dynamics

Rigid rotor dynamics is the branch of mathematics dealing with the motion of a rotating body for which the elastic (bending) deformations can be neglected, i.e. its own elastic deformations are negligible. This simplification is valid when the operating speed and the control bandwidth is well below the first bending (flexural) natural frequency of the rotor shaft, ensuring that it behaves like a rigid body rather than an elastic beam.

2.5.1 Rigid Body Kinetics

Rigid body kinetics is the branch of mechanics that establishes the relationship between the forces and moments exerted on a rigid body and its translational and rotational motion.

A rigid body is characterized by six degrees of freedom (DOF), which are made up of three translational and three rotational DOF. The derivation of the equations of motion begins with the momentum theorem (Newton's second law) and the angular momentum law. Using a body-fixed reference system, located in the body's center of gravity (COG) results in a set of equations of motion, also known as Euler equations. These are coupled nonlinear differential equations which describe the motion of the rotor shaft.

However, the rotor shaft considered in this thesis is a special case. It is rotationally symmetrical and rotates (with speed $\dot{\gamma} = \Omega$) around its axis of symmetry (z-axis, see Figure 2.5). Hence, the moments of inertia of the remaining two degrees of rotational freedom are equal and as a consequence, a spatially-fixed coordinate system can be used for modelling. This further simplifies Euler's equations. A comprehensive derivation of the equations of motion can be found in, for example, [9] and [10].

2.5.2 Equations of Motion

As described in the introduction, Euler's equations can be derived and simplified for a spatially-fixed coordinate system, located in the body's COG. However, it is essential for the position controller used that the axial and radial movements of the rotor shaft are decoupled from each other. This is possible under the following preconditions:

- the rotor is rotationally symmetrical and rigid
- rotor displacements from the reference position are small compared to the length of the rotor
- the forces are assumed to be conservative

- if the rotor is in the reference position, the spatially- and body-fixed coordinate systems are the same and are located at the rotor's COG
- the angular velocity Ω is assumed to be constant or to change slowly in comparison to the dynamics of the system

The above conditions are met in this thesis due to the design of the test stand and the fact that the rotor speed Ω can be considered to be set by the drive unit. This simplifies the generally nonlinear and coupled Euler equations and yields the linear equations of motion of the rotor shaft (with the axial and radial rotor shaft movements decoupled) in a spatially-fixed coordinate system

$$\begin{aligned} m\ddot{x} &= F_\mathrm{x} \\ m\ddot{y} &= F_\mathrm{y} \\ m\ddot{z} &= F_\mathrm{z} \\ \Theta_\mathrm{x}\ddot{\alpha} + \Theta_\mathrm{z}\Omega\dot{\beta} &= M_\mathrm{x} \\ \Theta_\mathrm{x}\ddot{\beta} - \Theta_\mathrm{z}\Omega\dot{\alpha} &= M_\mathrm{y} \\ \Theta_\mathrm{z}\dot{\Omega} &= M_\mathrm{z}, \end{aligned} \tag{2.35}$$

with rotor shaft mass m, angular velocity Ω and moment of inertia Θ_z around the z-axis, and the equal moments of inertia around the x- and y-axes, denoted by $\Theta_\mathrm{x} = \Theta_\mathrm{y}$.

The generalized coordinates x, y and z are used to describe the translational motion of the body's COG. The rotation angle of the body around the x-, y- and z-axes is described by the angles α, β and γ, respectively.

Lines four and five in this set, as well as the matrix $\mathbf{G}(\Omega)$ (see Equation 2.36), demonstrate the gyroscopic effect, which is defined as the coupling of the rotational DOF. Additionally, these equations are parameter-variant due to the gradual change in angular velocity Ω.

The careful design of the rotor lamination package of the radial magnetic bearings (excluding overhung and underhung scenarios) results in self-stabilization along the z-axis. Therefore, the equations of motion in the axial direction (third and sixth lines of Equations 2.35) are not necessary for describing the radial movement of the rotor shaft (due to the decoupling of the axial and radial movement) and a thrust bearing is not required.

The remaining four equations describe the radial motion of the rotor shaft by superposition of the translational and rotational motions

$$\underbrace{\begin{bmatrix} \Theta_\mathrm{x} & 0 & 0 & 0 \\ 0 & m & 0 & 0 \\ 0 & 0 & \Theta_\mathrm{x} & 0 \\ 0 & 0 & 0 & m \end{bmatrix}}_{\mathbf{M}} \underbrace{\begin{bmatrix} \ddot{\beta} \\ \ddot{x} \\ \ddot{\alpha} \\ \ddot{y} \end{bmatrix}}_{\ddot{\mathbf{q}}} + \underbrace{\begin{bmatrix} 0 & 0 & -\Theta_\mathrm{z}\Omega & 0 \\ 0 & 0 & 0 & 0 \\ \Theta_\mathrm{z}\Omega & 0 & 0 & 0 \\ 0 & 0 & 0 & 0 \end{bmatrix}}_{\mathbf{G}(\Omega)} \underbrace{\begin{bmatrix} \dot{\beta} \\ \dot{x} \\ \dot{\alpha} \\ \dot{y} \end{bmatrix}}_{\dot{\mathbf{q}}} = \underbrace{\begin{bmatrix} M_\mathrm{y} \\ F_\mathrm{x} \\ M_\mathrm{x} \\ F_\mathrm{y} \end{bmatrix}}_{\mathbf{F}} \tag{2.36}$$

which can be presented in a more compact matrix form

$$\mathbf{M}\ddot{\mathbf{q}} + \mathbf{G}(\Omega)\dot{\mathbf{q}} = \mathbf{F}, \tag{2.37}$$

with the mass matrix $\mathbf{M}$, the vector of the generalized coordinates $\mathbf{q}$, the matrix of the gyroscopic effect $\mathbf{G}(\Omega)$, and the vector of forces and moments $\mathbf{F}$.

Like the generalized coordinates $\mathbf{q}$, the forces and moments in the vector $\mathbf{F}$ refer to the rotor's COG. Figure 2.5 shows the configuration of the magnetic bearings and position sensors relative to the rotor shaft. This illustrates that the bearing forces must be transformed into forces and moments relative to the rotor's COG.

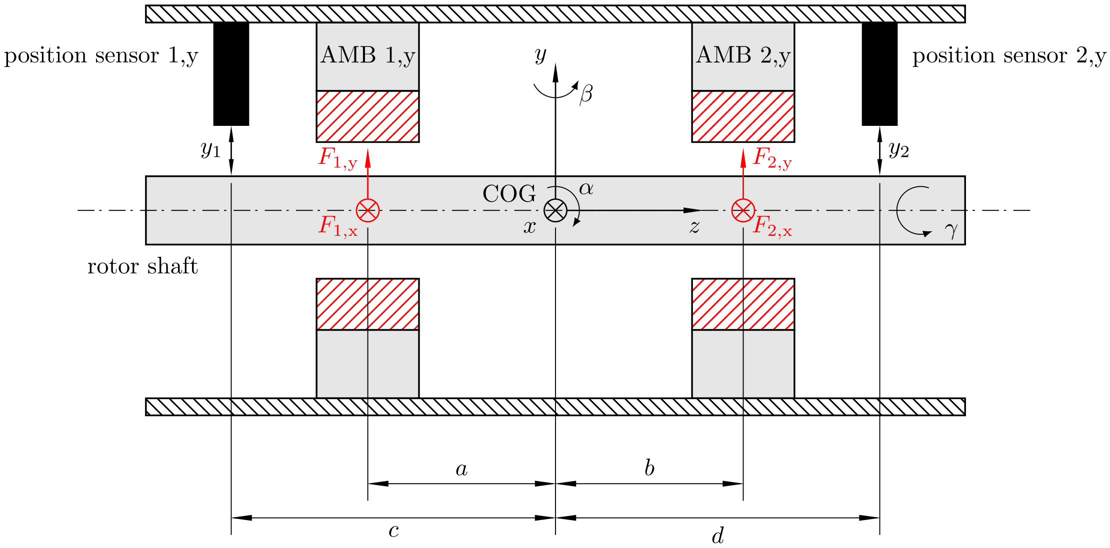

Figure 2.5: Cross-sectional view of the test stand along the y-z plane. It shows the position sensors and AMBs' electromagnetic actuators of the y-direction.

Based on the dimensions and forces shown in Figure 2.5, the following results are obtained for the forces and moments relative to the COG

$$\begin{aligned} F_{\mathrm{x}} &= F_{1,\mathrm{x}} + F_{2,\mathrm{x}} \\ M_{\mathrm{y}} &= -aF_{1,\mathrm{x}} + bF_{2,\mathrm{x}} \\ F_{\mathrm{y}} &= F_{1,\mathrm{y}} + F_{2,\mathrm{y}} \\ M_{\mathrm{x}} &= aF_{1,\mathrm{y}} - bF_{2,\mathrm{y}}. \end{aligned} \tag{2.38}$$

Therefore, the radial motion of the mechanical system can be described as follows

$$\underbrace{\begin{bmatrix} \Theta_{\mathrm{x}} & 0 & 0 & 0 \\ 0 & m & 0 & 0 \\ 0 & 0 & \Theta_{\mathrm{x}} & 0 \\ 0 & 0 & 0 & m \end{bmatrix}}_{\mathbf{M}} \underbrace{\begin{bmatrix} \ddot{\beta} \\ \ddot{x} \\ \ddot{\alpha} \\ \ddot{y} \end{bmatrix}}_{\ddot{\mathbf{q}}} + \underbrace{\begin{bmatrix} 0 & 0 & -\Theta_{\mathrm{z}}\Omega & 0 \\ 0 & 0 & 0 & 0 \\ \Theta_{\mathrm{z}}\Omega & 0 & 0 & 0 \\ 0 & 0 & 0 & 0 \end{bmatrix}}_{\mathbf{G}(\Omega)} \underbrace{\begin{bmatrix} \dot{\beta} \\ \dot{x} \\ \dot{\alpha} \\ \dot{y} \end{bmatrix}}_{\dot{\mathbf{q}}} = \underbrace{\begin{bmatrix} -aF_{1,\mathrm{x}} + bF_{2,\mathrm{x}} \\ F_{1,\mathrm{x}} + F_{2,\mathrm{x}} \\ aF_{1,\mathrm{y}} - bF_{2,\mathrm{y}} \\ F_{1,\mathrm{y}} + F_{2,\mathrm{y}} \end{bmatrix}}_{\mathbf{F}} . \tag{2.39}$$

The following transformation matrix[11] $\mathbf{B}$, which maps the vector of the magnetic bearing forces $\mathbf{F}_{\mathrm{AMB}}$ to the vector $\mathbf{F}$, is introduced

$$\underbrace{\begin{bmatrix} M_{\mathrm{y}} \\ F_{\mathrm{x}} \\ M_{\mathrm{x}} \\ F_{\mathrm{y}} \end{bmatrix}}_{\mathbf{F}} = \underbrace{\begin{bmatrix} -a & b & 0 & 0 \\ 1 & 1 & 0 & 0 \\ 0 & 0 & a & -b \\ 0 & 0 & 1 & 1 \end{bmatrix}}_{\mathbf{B}} \underbrace{\begin{bmatrix} F_{1,\mathrm{x}} \\ F_{2,\mathrm{x}} \\ F_{1,\mathrm{y}} \\ F_{2,\mathrm{y}} \end{bmatrix}}_{\mathbf{F}_{\mathrm{AMB}}} . \tag{2.40}$$

This facilitates compact matrix representation of the equation

$$\mathbf{M}\ddot{\mathbf{q}} + \mathbf{G}(\Omega)\dot{\mathbf{q}} = \mathbf{B}\,\mathbf{F}_{\mathrm{AMB}}. \tag{2.41}$$

2.5.3 Dynamics of Magnetically Levitated Rotors

Equation 2.36 describes the dynamics of a rotationally symmetric body to which a force $\mathbf{F}$ is applied, in general. To combine the electromagnetic and mechanical systems Equation 2.34 is substituted into (2.41) and this yields the electromechanical system equation for a magnetically levitated rotor shaft

$$\mathbf{M}\ddot{\mathbf{q}} + \mathbf{G}(\Omega)\dot{\mathbf{q}} = \mathbf{B}(\mathbf{K}_{\mathrm{x}}\mathbf{B}^{\mathrm{T}}\mathbf{q} + \mathbf{K}_{\mathrm{I}}\mathbf{i}), \tag{2.42}$$

with the matrices

$$\mathbf{K}_{\mathrm{x}} = \begin{bmatrix} k_{\mathrm{x1,x}} & 0 & 0 & 0 \\ 0 & k_{\mathrm{x2,x}} & 0 & 0 \\ 0 & 0 & k_{\mathrm{x1,y}} & 0 \\ 0 & 0 & 0 & k_{\mathrm{x2,y}} \end{bmatrix}, \ \mathbf{K}_{\mathrm{I}} = \begin{bmatrix} k_{\mathrm{I1,x}} & 0 & 0 & 0 \\ 0 & k_{\mathrm{I2,x}} & 0 & 0 \\ 0 & 0 & k_{\mathrm{I1,y}} & 0 \\ 0 & 0 & 0 & k_{\mathrm{I2,y}} \end{bmatrix}, \ \mathbf{i} = \begin{bmatrix} i_{1,\mathrm{x}} \\ i_{2,\mathrm{x}} \\ i_{1,\mathrm{y}} \\ i_{2,\mathrm{y}} \end{bmatrix}. \tag{2.43}$$

The entries in the matrices $\mathbf{K}_{\mathrm{I}}$ and $\mathbf{K}_{\mathrm{x}}$ can be calculated using Equations 2.32 and 2.33. However, these values are not constant. Instead, they depend on the operating point, which includes the actuator bias current (I_0) and air gap (δ_0), as well as the control current $\mathbf{i}$ and rotor displacement $\mathbf{q}$. The effects of possible saturation in the electromagnetic actuators and rotor lamination stacks are neglected. The entries in the current vector $\mathbf{i}$ are the AMBs' (1 and 2) control currents in the x- and y-directions. Note that the electrical subsystem is not included in the system described by (2.42). The relevant details are provided in the Chapter 3.2.3 of the *Active Magnetic Bearing* design.

Position sensors are required in order to close the output feedback loop (see Figure 2.4). Similar to the AMB forces, measured distance values must be transformed from their respective sensor coordinate systems into a spatially-fixed coordinate system (into the generalized coordinates). The system's output equation is as follows

$$\mathbf{y} = \mathbf{C}\mathbf{q} \tag{2.44}$$

---

[11] The entries in the transformation matrix $\mathbf{B}$ are the respective distances of the AMBs 1 and 2 from the rotor's COG (see Figure 2.5).

with the matrices:

$$\mathbf{C} = \begin{bmatrix} -c & 1 & 0 & 0 \\ d & 1 & 0 & 0 \\ 0 & 0 & c & 1 \\ 0 & 0 & -d & 1 \end{bmatrix}, \quad \mathbf{y} = \begin{bmatrix} x_1 \\ x_2 \\ y_1 \\ y_2 \end{bmatrix}. \tag{2.45}$$

As shown in Figure 2.5, the entries in the output matrix **C** represent the respective distances of the sensor planes 1 (c) and 2 (d) from the rotor's COG, while the entries of vector $\mathbf{y}$ are the measured distance values.

3 Test Stand Design

This chapter describes the development and design of the test stand, which is subdivided into five elements: drive unit, actuators (electromagnet and amplifier combination), position sensors, mechanical construction, and firmware.

Figure 3.1 shows the CAD sketch of the complete test stand assembly, designed during the course of this thesis. The housings for the auxiliary bearings, active magnetic bearings, and the synchronous reluctance machine (SynRM) are screwed onto the base plate, and an additional top plate stiffens the housings. Mounting brackets attach the position sensors to the two magnetic bearing housings.

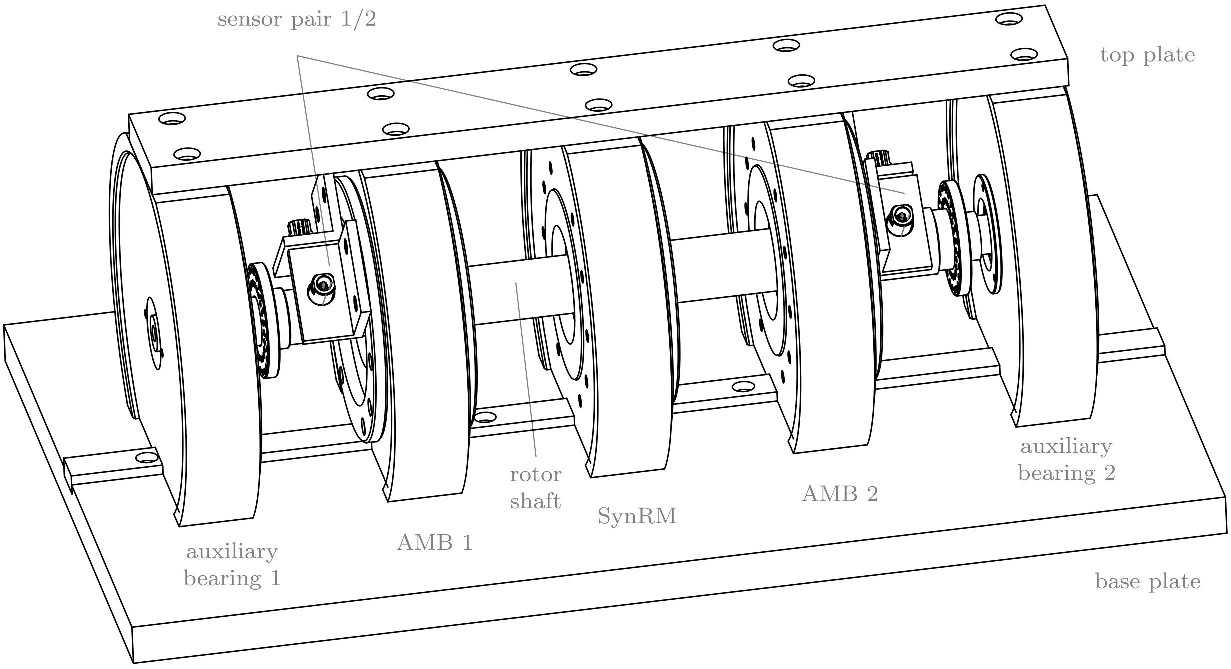

Figure 3.1: computer-aided design (CAD) sketch of the complete test stand assembly, designed during the course of this thesis. The mechanical design is carried out in SolidWorks®.

A SynRM is used to drive the rotor shaft, as a corresponding bachelor thesis [2] has already been carried out at the Institute for Energy Systems and Electrical Drives, TU Wien. The findings of this work are slightly modified, which is outlined in the first section *Drive Unit*.

The integral design of the electromagnet-amplifier combination and the verification of its mathematical and FEM model are presented in the section *Active Magnetic Bearing*.

Due to the inherent instability of AMBs, they must be integrated into a position control loop for stabilization. The *Position Sensors* are one of the most critical components of this position control loop. Therefore, a separate section is devoted to remarks on the basic operating principle, linearity, and necessary recalibration, as their specifications have a direct impact on the performance of the test stand.

Another critical element of the test stand is the *Mechanical Design* itself. The challenges caused by manufacturing tolerances and component alignment are addressed, as they have a significant impact on the functionality and usability of the test stand.

The *Hardware and Firmware Architecture* section provides an overview of the individual hardware components, the communication, safety mechanisms and position controller.

3.1 Drive unit

The following subsections provide brief descriptions of the primary components of the drive unit. Figure 3.2 shows the configuration, which includes the motor controller, the inverter, and the SynRM.

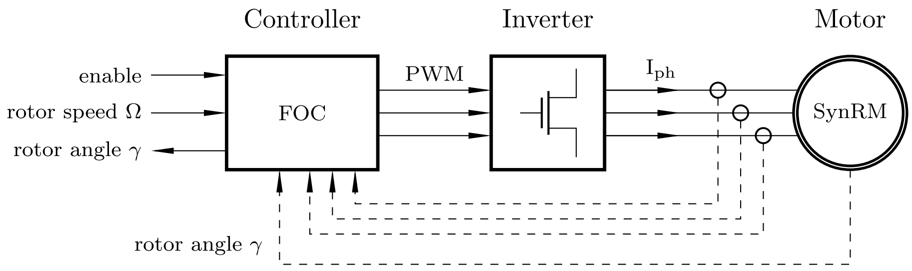

Figure 3.2: Schematic of the test stand's drive unit. A field-oriented control (FOC) is implemented in a digital signal processor (DSP) to drive the SynRM via a B6 bridge inverter.

3.1.1 Motor Controller

A FOC of the motor is implemented on a C2000™ DSP, a TMS320F28069 from Texas Instruments Incorporated[1]. This controller receives an enable command and the user-specified reference rotor speed Ω from the test stand control unit and returns the rotor angle γ. In addition to the reference speed Omega, the controller uses the rotor angle γ from the position sensor[2] and the motor phase currents to calculate the required control signals pulse width modulation (PWM) for the inverter.

3.1.2 Motor Inverter

The motor is powered by a three-phase B6 bridge inverter with a DC link voltage source. For simplicity, a commercially available inverter is used.

---

[1] Texas Instruments Incorporated; P.O. Box 655474, MS 3999; Dallas, Texas 75265

[2] AS5047P; ams AG, Tobelbader Strasse 30, 8141 Premstaetten, Austria-Europe

At this stage of the design process, the required torque of the drive unit should be known. It depends mainly on the eddy current losses of the magnetic bearing and the air friction losses of the rotor. Both depend on the angular velocity, but estimating them can be a challenging task. The achievable torque of a SynRM is determined by the phase current and the rotor design (reluctance difference) [11], [2].
Therefore, the most appropriate approach would be to perform a FEM analysis to determine the required torque in order to systematically find a suitable inverter/SynRM-rotor combination.
To simplify things, the DRV8323[3] BoosterPack™ from Texas Instruments Incorporated was chosen as a first step because of its compatibility with the DSP used.

3.1.3 Synchronous Reluctance Machine

A SynRM was chosen for the drive unit of the test stand because of its simplicity - the rotor contains neither windings nor permanent magnets and is therefore robust and inexpensive to build. In addition, a SynRM intended for use in a magnetic bearing has previously been developed by Spießberger as part of a bachelor thesis in [2].
The basic function of a SynRM is independent of the specific rotor design. The operation is based on the periodic change of the magnetic resistance (reluctance) of the air gap along the circumference of the machine. Due to this reluctance difference between adjacent poles, the rotor experiences an aligning tangential pulling force in the stator magnetic field. Rotor regions with minimal reluctance will seek to align with regions characterized by high air gap field strength. As the stator magnetic field moves, the rotor is pulled along, resulting in synchronous motion [11].

3.1.3.1 Stator design

The design of the drive unit was initiated by [2], where the development of a SynRM is demonstrated. This machine incorporates a distributed stator winding system designed to reduce torque ripple in conjunction with a salient pole rotor.
However, given that torque ripple is not a concern for the test stand application, the use of a commercially available stator with concentrated windings is considered the optimal choice. This decision is primarily driven by economic considerations and the limited number of manufacturers that specialize in distributed winding systems.
The purpose of the stator's rotating field winding, whether concentrated or distributed, is to generate radial magnetic field strength within the air gap. When a rotating current ($\mathrm{I_{ph}}$) is supplied by the inverter, a rotating magnetic field strength is generated in the machine's air gap. The relationship between the angular velocity of this field (Ω) and the rotating current (Ω_{el}) is as follows

$$\Omega = \frac{\Omega_{\mathrm{el}}}{p} \tag{3.1}$$

with the number of pole pairs p. The synchronization between the rotating field and the rotor itself leads to

$$\Omega = \Omega_{\mathrm{mech}}. \tag{3.2}$$

---

[3] Maximum DC link voltage $\mathrm{U_{DC}} = 54\,\mathrm{V}$, maximum continuous phase current $\mathrm{I_{ph,rms}} = 15\,\mathrm{A}$

Therefore, the higher the number of pole pairs p, the higher the angular velocity of the rotary current Ω_{el} at a desired mechanical speed Ω_{mech}.
This angular velocity Ω_{el} also determines the minimum required switching frequency of the inverter. So for this high-speed application with rotor speeds Ω_{mech} in the order of $2\pi{\cdot}400\,\mathrm{s}^{-1}$, the rotor shape already defined in [2] (see Figure 3.4b) with $p = 2$ and $2p = 4$ (number of poles) seems to be a reasonable starting point for further FEM analysis.
The stator magnetic field is also 4-pole, and the number of required stator teeth (or slots) Q is calculated as follows

$$Q = 2p \cdot m \cdot q = 4 \cdot 3 = 4 \cdot 3 \cdot 1 = 12 \tag{3.3}$$

with the number of winding strands $m = 3$ (B6 bridge three-phase inverter) and the number of slots per pole and strand $q = 1$ [11].
The necessary specifications for the stator and its winding are determined by the inverter's maximum phase current and the required number of stator teeth Q.
The stator from the NH1-D100 frameless motor kit manufactured by NIDEC®[4] - specifications can be found in Table 3.1 and the CAD drawing in Figure 3.3b - seems to be suitable for this application. Extensive FEM simulations were carried out before a prototype motor with this stator was built.
The NH1-D100 stator is designed for use in a brushless DC motor (BLDC) machine. Therefore, it was necessary to adapt the winding scheme by means of a circuit board located directly on the lead end side of the stator (Figure 3.3a). The configuration is shown in Figure 3.3, which clearly shows the 4-pole structure with three phases (L_1, L_2, L_3), spatially offset by an angle of 120°.

Part Number	NH1-D100
standard bus voltage (Vdc)	48
stack heights (mm)	32
rated current (Arms)	23
peak current (Arms)	57.5
stator insulation rating (°C)	155
R (ph-ph) (Ohm)	0.1
L (ph-ph) (mH)	0.33
outer diameter (mm)	100.18 ±0.025
inner diameter (mm)	59
number of coils/teeth	12
number of turns	25

Table 3.1: Stator specifications of the frameless motor kit NH1-D100.

3.1.3.2 Rotor design

As mentioned above, periodic modulation of the air gap reluctance is essential for the basic operation of the SynRM. How this reluctance difference is achieved is of secondary importance. Possible rotor designs

---

[4] NIDEC® CORPORATION, 338 Kuzetonoshiro-cho, Minami-ku, Kyoto 601-8205, JAPAN

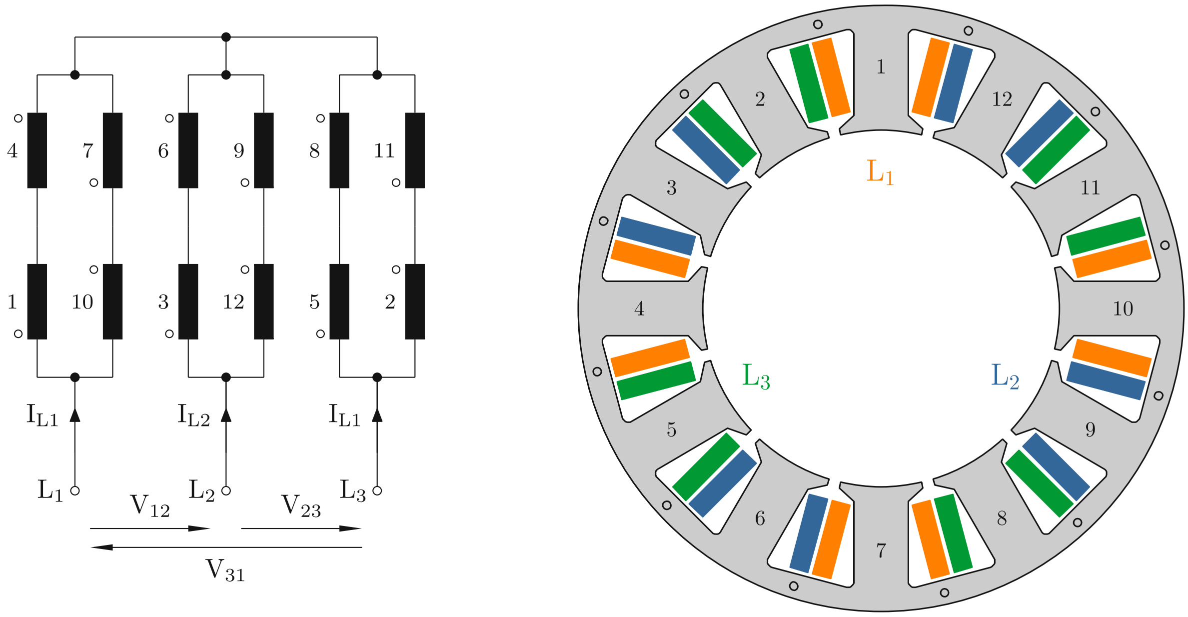

(a) SynRM winding scheme

(b) SynRM stator with coils

Figure 3.3: CAD drawing of the stator from the BLDC frameless kit NH1-D100 with 12 coils (dots mark the direction of winding). The three phase, four branch winding scheme is adapted for use in a SynRM.

are shown in Figure 3.4.

In the left rotor design (Figure 3.4a), the reluctance difference is achieved by the use of so-called flux barriers. The rotor has a low reluctance in the direction of the d-axis. Conversely, flux conduction in the q-axis direction is hindered by these barriers, resulting in increased magnetic resistance.

Figure 3.4b shows the double salient pole rotor that has been optimized for the use within a distributed winding system as described in [2]. The rotor's configuration creates a reluctance difference by modulating the air gap around the machine's circumference. In the direction of the d-axis the resulting air gap is minimal, while in the direction of the q-axis a substantial air gap is formed.

This design is used as the initial template for the rotor in this thesis due to its advantageous simplicity, which is important for the manufacturing process[5]. Figure 3.4c shows the final design of the rotor, used in this work.

3.1.3.3 Simulation Results

The drive unit chapter concludes with a brief overview of the simulation results derived from the FEM analysis.

First, the functionality of the SynRM is demonstrated qualitatively. In Figure 3.5, the magnetic conditions in the SynRM[6] at a certain point in time ($t = 254.54\,\mu\text{s}$[7]), and for the maximum allowable stator phase

---

[5] The high cost of contract manufacturing was a key factor in the decision to make the rotor plate cuts in-house. A metal laser from a rental shop was used for this purpose.

[6] The image shows only a quarter of the machine in its entirety, with the understanding that it is representative for the entire machine with the pole number $2p = 4$.

[7] At a speed of $\Omega = 2880\,\text{rad}\,\text{s}^{-1}$, this time corresponds to a mechanical angle of $\gamma_{\text{mech}} = 42°$ and, due to the number of pole pairs $p = 2$, an electrical angle of $\gamma_{\text{el}} = 84°$.

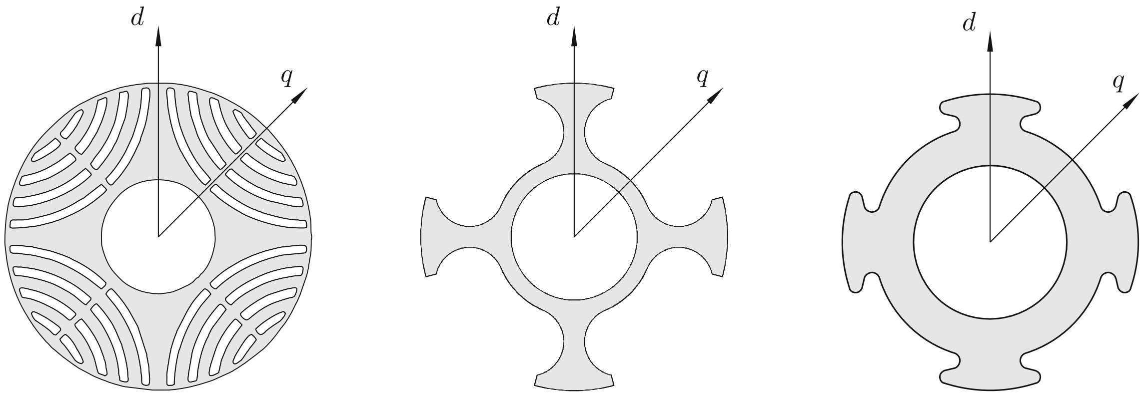

(a) Rotor with flux barriers (b) Rotor utilised in [2] (c) Rotor utilised in this work

Figure 3.4: Different 4-pole rotor designs for the use in a SynRM; due to their double pole pair ($p = 2$) structure, the mechanical angle between the rotors' d- and q-axes is $\gamma_{\mathrm{mech}} = 45°$.

current[8] ($\mathrm{I}_{\mathrm{Lx,rms}} = 23\,\mathrm{A}$) is shown, while the rotor rotates counterclockwise at $\Omega = 2880\,\mathrm{rad\,s^{-1}}$ ($n = 27\,500\,\mathrm{rpm}$[9]).

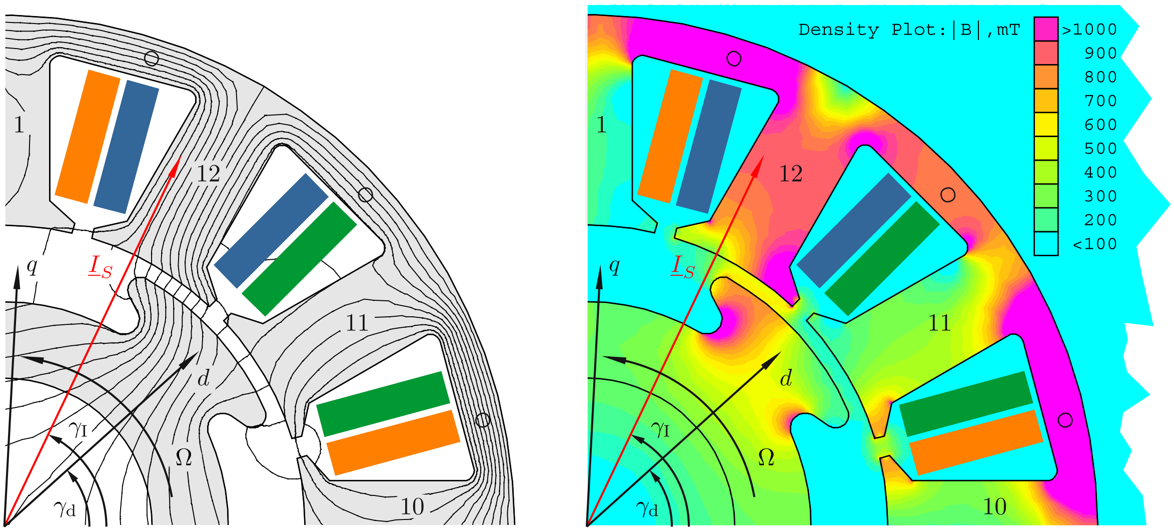

(a) Field line diagram of flux density, $\boldsymbol{B}$ (b) Density plot of flux density, B

Figure 3.5: Magnetic field condition in one pole of the 4-pole SynRM at $t = 254.54\,\mathrm{\mu s}$, $\Omega = 2880\,\mathrm{rad\,s^{-1}}$ and for $\mathrm{I}_{\mathrm{Lx,rms}} = 23\,\mathrm{A}$.

Figure 3.5a shows the field line diagram of the magnetic flux density **B** and Figure 3.5b is a colored plot of the magnetic flux density. Both figures show the occurrence of asymmetry of the magnetic flux density in the air gap along the pole shoe. In the pole shoe's front region is a higher magnetic flux density, expressed by the yellow area in the air gap. Hence, a tangential pulling force occurs at the pole in the direction of higher flux density, generating an electromagnetic torque in the direction of Ω[10]. In order to apply a

---

[8] The operating condition was thus analyzed to identify areas of excessive magnetic saturation.

[9] revolutions per minute (RPM)

[10] As mentioned above, the low reluctance regions (rotor d-axis) try to align with the high magnetic field areas.

motor torque, as in this case, it is necessary that the regions of increased flux density **B** are in front of the pole (more precisely, rotor *d*-axis). To emphasize this fact, the picture also shows the actual position of the *d*- and *q*-axes of the rotor ($\gamma_\mathrm{d} = \gamma_\mathrm{mech} = 42°, \gamma_\mathrm{q} = 87°$) with respect to the stator current phasor $\underline{\mathrm{I}}_\mathrm{S}$ ($\gamma_\mathrm{I} = 64.5°$).

The current phasor $\underline{\mathrm{I}}_\mathrm{S}$ is formed by the phase current in the strings (I_L1, I_L2, I_L3)[11] and represents the distribution (of the fundamental wave) of the magnetic voltage and the magnetic flux density [11].

To achieve maximum torque per ampere (MTPA), the position of the current phasor has to be exactly between the *d*- and *q*-axes of the rotor [11]. Thus, in a mechanical sense, it advances the *d*-axis by $\gamma_\mathrm{I} - \gamma_\mathrm{d} = 22.5°$[12].

This revisits the previously cited motor controller. In the context of FOC, it is important that the controller uses an appropriate voltage pulse pattern. This ensures that the resulting current phasor $\underline{\mathrm{I}}_\mathrm{S}$ is in the correct position relative to the rotor's *d*-axis. Therefore, this control strategy requires knowledge of the rotor's angle γ_d. The underlying (cascaded) control strategy is adopted and has not been developed in the course of this thesis. The control system simply sends the desired speed as a reference to the motor controller and reads back the actual rotor position angle $\gamma_\mathrm{d} = \gamma$.

Finally, simulations were performed to determine the suitability of the selected drive for the intended application. Therefore, the angular velocity is set to the maximum permissible value of the angular position sensor[13]: $\Omega = 2880\,\mathrm{rad\,s^{-1}}$ ($n = 27\,500\,\mathrm{rpm}$). The phase current I_Lx (Figure 3.6c) is gradually increased until the induced phase-to-phase voltage V_xy (Figure 3.6b) reaches the maximum achievable value ($\mathrm{V}_\mathrm{xy,max} = \frac{\mathrm{U}_\mathrm{DC}}{\sqrt{3}} = \frac{54\,\mathrm{V}}{\sqrt{3}} = 31.2\,\mathrm{V}$) with some safety margin.

The simulations show the ability to generate an average torque of about 22 mN m at the maximum possible angular velocity (Figure 3.6a). The amplitude of the phase current is $\hat{\mathrm{I}}_\mathrm{Lx,sim} = 12\,\mathrm{A}$ and that of the phase to phase voltage is $\hat{\mathrm{V}}_\mathrm{xy,sim} = 26.3\,\mathrm{V}$.

The torque ripple is caused by the 12 stator teeth. The minimum torque occurs when the front pole flank of the rotor is geometrically aligned with the front tooth flank of the stator. This is when the magnetic flux has to be passed from one tooth to the next and is therefore almost reduced by the gap between the teeth (see Figure 3.5). In contrast, it was found that the maximum torque is generated when the rear pole flank of the rotor is geometrically aligned with the rear flank of the preceding tooth.

These simulation results were validated through measurements taken on a small prototype motor with ball bearings, which was built specifically for this purpose. At an angular velocity of $\Omega = 2880\,\mathrm{rad\,s^{-1}}$, the measured phase current is $\hat{\mathrm{I}}_\mathrm{Lx,meas} = 12\,\mathrm{A}$ and the phase-to-phase voltage is $\hat{\mathrm{V}}_\mathrm{xy,meas} = 24.52\,\mathrm{V}$.

The comparison with the simulation results emphasizes the good agreement between the simulation model (stator, winding system and rotor) and the real system. In addition, it is reasonable to conclude from this practical test that equally high speeds can be achieved on the test bench[14]. Therefore, the proposed combination of motor inverter (DRV8323 BoosterPack™, Texas Instruments Incorporated), stator (NH1-D100, NIDEC® CORPORATION) and double salient pole rotor design seems promising.

---

[11] For a comprehensive overview of the subject, with detailed references, see [11] and [12].

[12] This is only true for the 4-pole rotor in this work. In general, the phase lead between the stator current phasor and the *d*-axis is 45° in the electrical domain.

[13] AS5047P; ams AG, Tobelbader Strasse 30, 8141 Premstaetten, Austria-Europe

[14] However, braking torque due to eddy current losses and increased air friction due to the longer rotor shaft may reduce the angular speed that can be achieved at the test stand setting.

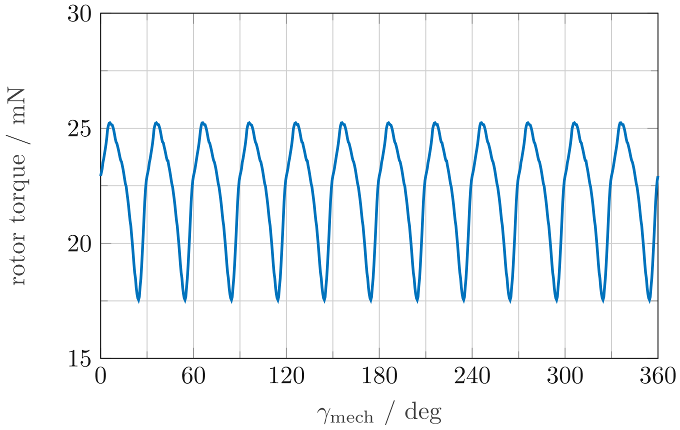

(a) Rotor torque curve; the ripple is caused by the 12 stator teeth.

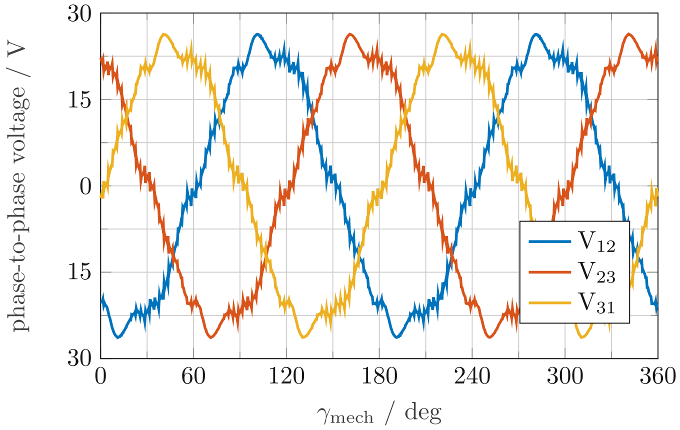

(b) Phase-to-phase voltages; emphasizes the spatial position (120° offset) of the strands.

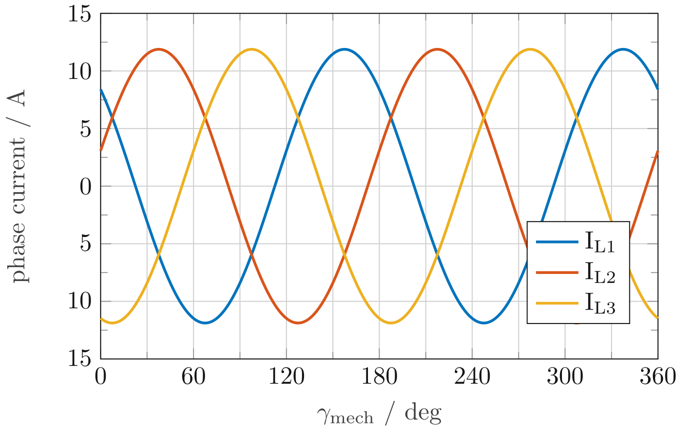

(c) Stator phase currents; three-phase system.

Figure 3.6: Simulation results of the SynRM at an angular speed of $\Omega = 2880\,\mathrm{rad\,s^{-1}}$ ($n = 27\,500\,\mathrm{rpm}$). The figures show the curves of rotor torque, phase-to-phase voltages, and phase currents as the rotor performs one full rotation.

3.2 Active Magnetic Bearing

The central component of the test stand, is the active magnetic bearing. The process of dimensioning an AMB is a multilevel procedure in which both mechanical and electromagnetic aspects as well as control technology have to be taken into account.

The magnetic bearing can be understood as a combined system of an amplifier and an electromagnet. In this integrated setup, the amplifier acts as the critical interface that converts low-power control signals – typically generated by a microprocessor in a sensor feedback system – into high-power currents that can drive the electromagnet. The electromagnet, produces a magnetic field whose strength can be precisely controlled to generate the necessary forces for suspension and stabilization.

The amplifier and the electromagnet are interdependent, so to achieve the desired performance, their design must be considered as a unified process. The first step in the process is to design the electromagnet according to the specified requirements, followed by the development of an appropriate amplifier.

3.2.1 Electromagnet Design

The general workflow for systematically designing the actuator of an active magnetic bearing is outlined in the following steps [1], [6]:

- **Requirements analysis and load definition:** First, the operating conditions, such as rotating masses, speeds, forces and dynamic loads, must be precisely defined. Both static and dynamic loads are considered to determine the necessary holding capacities and safety margins.
- **Magnetic field and force calculations:** The required magnetic forces are determined based on the specified loads. This involves calculating the magnetic field strengths, sizing the actuators (electromagnets) and designing the air gaps. Smaller air gap widths increase force density, but require tighter manufacturing tolerances and more precise control to ensure stability and vibration damping.
- **Consideration of boundary conditions:** Practical challenges include the saturation limits of the magnets, thermal effects, and mechanical resonances. These parameters must be considered in the design to ensure safe operation under all intended load cases.
- **Simulation and verification:** Before implementation, simulations are performed to test the dynamic behavior of the system under real operating conditions. Experimental testing and iterative adjustments help refine the design and achieve the desired key performance indicators.

This recipe-like sequence can hide the fact that the development of an AMB is often an iterative process, as in this case. The lack of specifications regarding static or dynamic loads, desired stiffness, or achievable speeds necessitates the formulation of assumptions in these critical preliminary steps of system design.

The static load is estimated based on the expected rotor shaft mass. This is primarily determined by the length needed to accommodate the rotor packages (magnetic bearings and motor), sensors, and auxiliary bearings. From a manufacturing perspective, the shaft length then requires a minimum shaft thickness (see the specification sheet in Table 3.2[15]).

---

[15] The following requirements are only approximate at this stage.

On the contrary, the dynamic load to be expected depends on the unbalance and the rotor speed. These parameters can only be quantified with the manufactured rotor shaft on the test stand. Therefore, the dynamic load was assumed to be approximately four times the static load.

While this method results in the test stand's electromagnet being oversized[16], it keeps the electromagnet in its more linear regime – a simpler controller architecture can be applied – and allows coverage of a larger test range.

In contrast to the load capacity, other important magnetic bearing parameters can be modified later. The stiffness of the bearing, for example, can be adjusted by the software current controller. It is also possible to add unbalance compensation in the position controller to cope with higher rotor speeds.

In order to minimize the complexity of the mechanical system and to be cost effective, a heteropolar bearing structure is used. The system structure can be further simplified by selecting an appropriate number of poles, e.g. an eight-pole bearing configuration (see Figure 3.7b).

Eight-pole bearings are a special category of AMBs. They are easier to handle because their design naturally decouples the radial force components in two independent, orthogonal directions[17]. Aligning them to the x- and y-axes of the Cartesian coordinate system of the other components (position sensors, shaft's rotary position sensor) simplifies simulation, control design, and sensor measurement, since the system can be linearized in each direction independently, avoiding the inherent coupling problems that arise in configurations with fewer poles. For example, three poles still allows levitation, but becomes much more complex [1].

appr. total rotor weight m (kg)	3 to 4
appr. total static Load $F_{\mathrm{R,stat}}$ (N)	30 to 40
appr. total dynamic Load $F_{\mathrm{R,dyn}}$ (N)	120 to 160
max. air gap flux density B_{g} (T)	0.6
structure	heteropolar
number of poles	8

Table 3.2: AMB requirements sheet

Based on the requirements and the selected topology from Table 3.2, the required pole area can be determined with Equation 2.8. This equation applies to the area of both poles as shown in Figure 2.1a. The result from (2.8) is related to the total area. Thus, the virtual magnetic tensile stress acting orthogonally on the surface can be obtained

$$P_{\mathrm{m}} = \frac{F_{\mathrm{R}}}{2A_{\mathrm{g}}} = \frac{B_{\mathrm{g}}^2}{2\mu_0} = \frac{(0.6\,\mathrm{T})^2}{8\pi\cdot 10^{-7}} = 0.14\cdot 10^6\,\mathrm{Pa} = 0.14\,\mathrm{N\,mm^{-2}}. \tag{3.4}$$

Assuming an almost symmetrical magnetic bearing[18] configuration relative to the rotor COG, it can be concluded that the dynamic load $F_{\mathrm{R,dyn}}$ is equally distributed between both bearings. The minimum total

---

[16] An undersaturated magnet wastes iron, while an undersaturated amplifier wastes capacity [1].

[17] Strictly speaking, this is only true if the rotor is at the center of the magnetic bearing. Otherwise, cross-coupling occurs, as shown in the Section 3.2.4

[18] In this context, symmetrical refers to the distances between the AMBs and the rotor's COG.

area required results in

$$2A_\mathrm{g} = \frac{F_\mathrm{R,dyn}}{P_\mathrm{m}} = \frac{\frac{1}{2}160\,\mathrm{N}}{0.14\,\mathrm{N\,mm^{-2}}} \approx 560\,\mathrm{mm}^2. \tag{3.5}$$

Thus, for a heteropolar magnetic bearing in an 8-pole configuration, the minimum area per pole (at a moderate air gap flux density) is approximately 280 mm^2.

This leads to the question if the stator of the drive unit can be used for the magnetic bearing. The stator in question has 12 poles (see Figure 3.3b), with four pairs of poles oriented orthogonally to each other. This configuration makes the stator well suited for the use as an AMB. As shown in Table 3.3, the key magnetic data of the stator are listed to facilitate the evaluation of its suitability as a magnetic bearing.

pole area A (mm^2)	430
RMS current I (A)	11
peak current I_peak (A)	28
number of turns N	25
presumed air gap width δ_0 (µm)	1100
peak air gap flux density B_peak (T)	0.8

Table 3.3: Stator specification sheet (of the frameless motor kit NH1-D100).

With respect to the required pole area, the stator seems to be usable. The air gap width is also a key design parameter, and is still undetermined. A compromise must be made between two factors: manufacturing tolerances and radial alignment of the components to each other[19] (large air gap width) and low power consumption and heat generation in the magnetic bearings (small air gap width)[20].

With (2.18) the estimation of the maximum achievable magnetic flux density in the air gap B_peak according to the stator specification given in Table 3.3 can be estimated

$$B_\mathrm{peak} = \mu_0 H_\mathrm{peak} \approx \mu_0 \frac{2NI_\mathrm{peak}}{2\delta_0} = \mu_0 \frac{25 \cdot 28\,\mathrm{A}}{1100\,\mathrm{\mu m}} = 0.8\,\mathrm{T}. \tag{3.6}$$

In this context, it is worth considering whether the magnetic bearing can lift the rotor, when it is resting in the auxiliary bearings. This represents the worst case scenario, as the air gap in the upper actuator reaches its maximum value, and this actuator also has to generate the lifting force. Hence, when the resulting air gap is the sum of the mechanical air gap (presumed to be $\delta_\mathrm{mech} = 500\,\mathrm{\mu m}$) in the auxiliary bearings and the nominal air gap in the magnetic bearings ($\delta_0 = 1100\,\mathrm{\mu m}$). The lifting force can be estimated by the Equations 3.6 and 3.5 and results to

$$F_\mathrm{R,lift} = \frac{B_\mathrm{g}^2 A_\mathrm{g}}{\mu_0} = \mu_0 \left(\frac{NI_\mathrm{peak}}{\delta_0 + \delta_\mathrm{mech}}\right)^2 = 4\pi \cdot 10^{-7} \left(\frac{25 \cdot 28\,\mathrm{A}}{1100\,\mathrm{\mu m} + 500\,\mathrm{\mu m}}\right)^2 430\,\mathrm{mm}^2 = 103\,\mathrm{N}. \tag{3.7}$$

Even one actuator of a magnetic bearing would generate enough force to lift the rotor shaft from its lower resting position, given the specified weight of the rotor shaft.

It has been demonstrated that the NH1-D100 stator is well suited to meet the desired magnetic bearing

---

[19] Manufacturing unbalance and eccentricities of the rotor shaft increase its orbit, which may also require a larger air gap width.

[20] After a design iteration, the air gap width was reduced due to two factors. First, the selected amplifier was unable to provide the required peak current. Second, the thermal losses due to the winding resistances were too high.

requirements with some additional safety margins. However, the length of the air gap remains a design parameter that must be verified through appropriate validation, with particular emphasis on the winding temperature of the magnetic bearing.

Figure 3.7 shows the winding diagram and a CAD sketch of the magnetic bearing. Its heteropolar, differential drive mode, 8-pole structure is clearly recognizable.

The coils are connected so that the magnetic bearing rotor package sees the following air gap field sequence: -S-N-N-S-S-N-N-S-. This reduces the eddy current losses experienced by the rotor package.

Two pole pairs form a double reluctance actuator. For example, pole pairs 2/3 and 8/9 form the double reluctance actuator for the x-direction (force direction $F_{1,\mathrm{x}}$), while pole pairs 11/12 and 5/6 are used for the y-direction (force direction $F_{1,\mathrm{y}}$)[21].

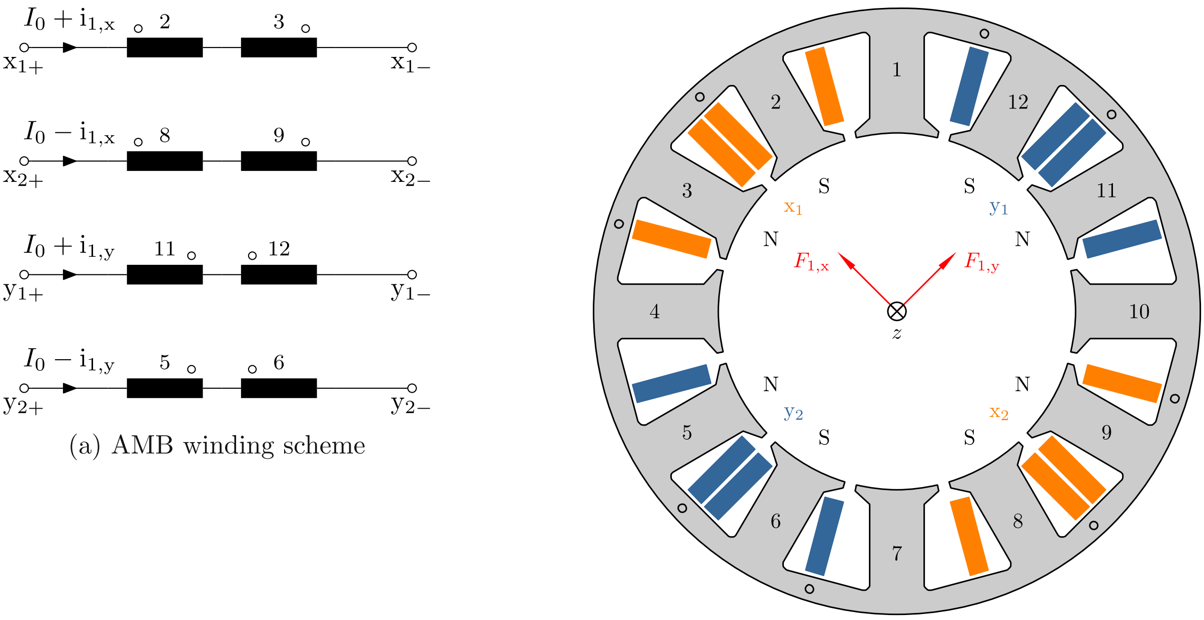

(a) AMB winding scheme

(b) AMB stator with coils

Figure 3.7: CAD drawing of the stator from the BLDC frameless kit NH1-D100 with the 8 coils (dots mark the direction of winding) used for the AMB. The three-phase, four-branch winding scheme is adapted for use in the AMB.

3.2.2 AMB Amplifier

3.2.2.1 Electrical schematic and timing diagram

The magnetic bearing amplifier is responsible for converting the control variable from the controller into a power signal, such as a current (current mode amplifier) or voltage - see Figure 2.4. The use of a switching power amplifier is recommended to minimize power dissipation.

Given the topology and driving mode used, a two-quadrant current controller would suffice because the

---

[21] The force directions ($F_{1,\mathrm{x}}$ and $F_{1,\mathrm{y}}$) shown in the Figure 3.7b correspond to magnetic bearing 1 and the same applies to magnetic bearing 2.

currents in the coil pairs (I_1 and I_2) do not change their sign during operation (see Figure 3.7a and 3.8). However, a commercially available inverter is used here as well. The safety mechanisms to protect against bridge shoot-through, overtemperature and overcurrent are of paramount importance when selecting these inverters. Above all, compatibility with the DSP is also a decisive factor.

The current controller is implemented on a C2000™ DSP, a TMS320F28379D[22] from the company Texas Instruments Incorporated[23]. The DRV8305 BoosterPack™ from Texas Instruments Incorporated appears to be well suited to the requirements in terms of magnetic bearing (current rating) and compatibility with the desired DSP (analog digital converter (ADC) and PWM ports).

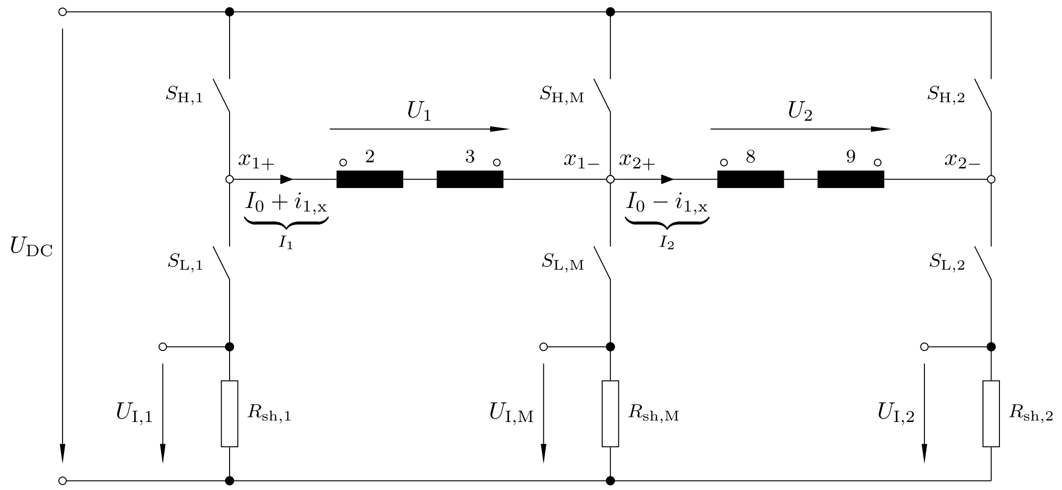

Figure 3.8: B6 bridge of the DRV8305 BoosterPack™ and its use as a current mode magnetic bearing amplifier.

Figure 3.8 provides a schematic representation of the power section of the B6 bridge three-phase inverter. The methodology by which this inverter topology can be used to (differentially) drive the coils of the actuators is explained in [13] and [14]. There, it was shown that a half-bridge can be shared by the coils of one direction of force (a double reluctance actuator) by making appropriate connections.

As shown in Figure 3.8, the two coil pairs 2/3 and 8/9 of a double reluctance actuator (acting in x-direction) are connected between the three bridge branches and share the bridge branch M in the middle. However, contrary to the proposal, the current direction in the coil pairs is chosen in such a way that the bridge branch M only has to carry the differential current between I_1 and I_2, i.e. twice the control current ($I_1 - I_2 = 2i_{1,\mathrm{x}}$). From this it can be concluded that a single inverter is required for each DOF, so a total of four inverters are required for the AMBs.

The following section will explain how to control the individual bridge branches in order to set the currents in the coils accordingly. This is facilitated by the signal curves shown in Figure 3.9.

The three diagrams denoted $S_{\mathrm{H},1}$, $S_{\mathrm{H,M}}$ and $S_{\mathrm{H},2}$ schematically show the upper switch positions. In the presence of a high signal, the upper switches are closed and the lower switches are open. Conversely, for a low signal, the lower switches are closed and the upper ones are open. It can be assumed that the signals schematically represent the respective voltages at the three connection nodes denoted x_{1+}, x_{1-}/x_{2+}, and x_{2-}.

---

[22] This DSP was used due to economic considerations and availability. In addition, its performance simplifies the development process.

[23] Texas Instruments Incorporated; P.O. Box 655474, MS 3999; Dallas, Texas 75265

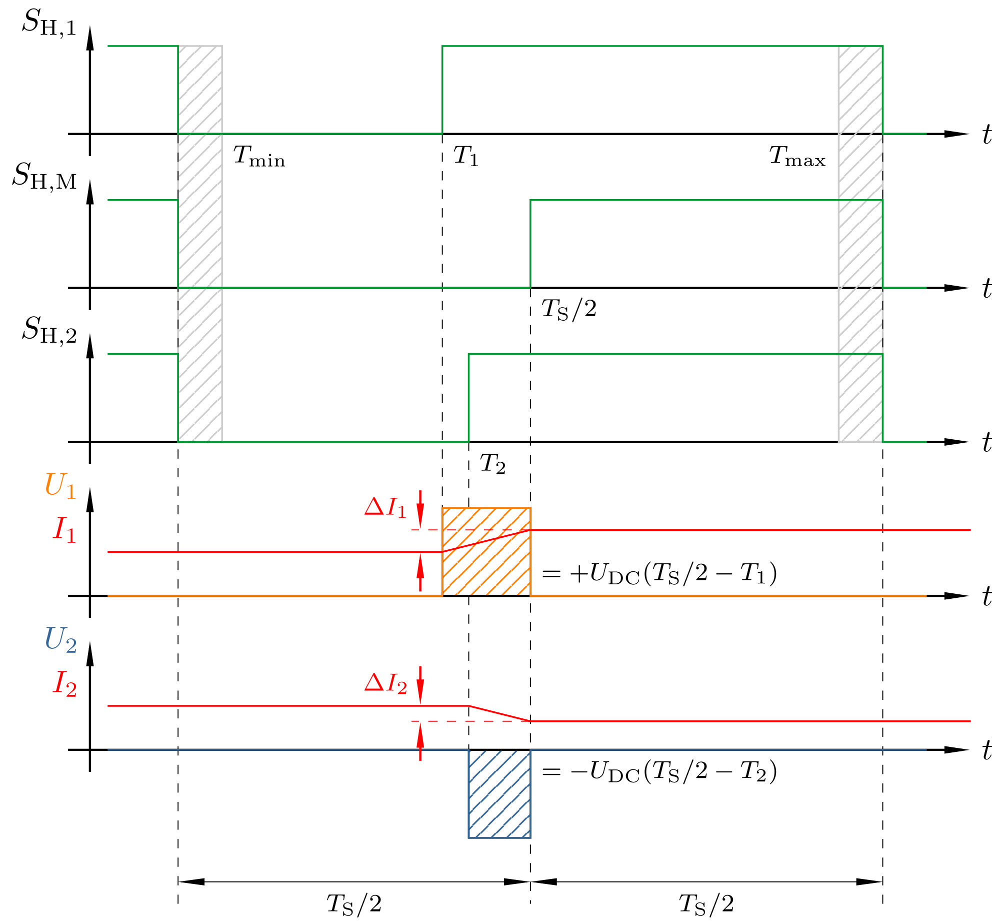

Figure 3.9: Timing diagram of the B6 bridge inverter and the corresponding actuator voltage and current signals. The resistance of the coil pair is assumed to be negligible, resulting in linear current ramps.

The DSP controls the switches via its PWM outputs. The switching time for the middle branch M is constantly set at half the total cycle length, hence $T_\mathrm{S}/2$. This means that with a switching frequency of $f_\mathrm{S} = 50\,\mathrm{kHz}$ and a cycle time of $T_\mathrm{S} = 20\,\mathrm{\mu s}$, the switching time is constant at $t = T_\mathrm{M} = T_\mathrm{S}/2 = 10\,\mathrm{\mu s}$. The other two branches are switched or modulated so that the current is set according to the control variable from the current controller - branch 1 is switched at $t = T_1$ and branch 2 at $t = T_2$.

In the case of $T_1 < T_\mathrm{S}/2$, as shown in Figure 3.9, a positive voltage-time surface $= U_\mathrm{DC}(T_\mathrm{S}/2 - T_1)$ is applied to coil pair 2/3 according to the circuit in Figure 3.8. In accordance with the relationship between voltage and current across an inductor

$$U_1 = L_{(2/3)} \frac{\mathrm{d}I_1}{\mathrm{d}t}, \tag{3.8}$$

the resulting increase in current for an almost ideal inductor ($R_{(2/3)} \approx 0$) can be estimated by the following equation

$$\Delta I_1 = \frac{1}{L_{(2/3)}} U_1 \Delta t = \frac{1}{L_{(2/3)}} U_\mathrm{DC}(T_\mathrm{S}/2 - T_1). \tag{3.9}$$

Due to the opposite connection of the coil pair 8/9, $T_2 < T_\mathrm{S}/2$ (Figure 3.9) results in a negative voltage-time surface $= -U_\mathrm{DC}(T_\mathrm{S}/2 - T_2)$, applied to coil pair 8/9. This leads to a decrease of the current by

$$\Delta I_2 = \frac{1}{L_{(8/9)}} U_2 \Delta t = \frac{1}{L_{(8/9)}} [-U_\mathrm{DC}(T_\mathrm{S}/2 - T_2)]. \tag{3.10}$$

3.2.2.2 Mathematical model

The design of the current controller requires a mathematical model of the amplifier. To derive this model, the branches can be visualized as individual buck converters. The subsequent node voltages are derived by calculating the average of the voltages over the switching period T_S according to the duty cycles

$$\begin{aligned} U_{\mathrm{x}_{1-}} = U_{\mathrm{x}_{2+}} =& \quad U_\mathrm{DC}\frac{T_\mathrm{S}/2}{T_\mathrm{S}} = U_\mathrm{DC}\frac{1}{2} \\ U_{\mathrm{x}_{1+}} =& \quad U_\mathrm{DC}\frac{T_1}{T_\mathrm{S}} = U_\mathrm{DC}\delta_1 \\ U_{\mathrm{x}_{2-}} =& \quad U_\mathrm{DC}\frac{T_2}{T_\mathrm{S}} = U_\mathrm{DC}\delta_2, \end{aligned} \tag{3.11}$$

resulting in the voltages U_1 and U_2 by subtracting the corresponding node voltages

$$\begin{aligned} U_1 =& \quad U_{\mathrm{x}_{1+}} - U_{\mathrm{x}_{1-}} = U_\mathrm{DC}(\delta_1 - \frac{1}{2}), \quad 0 < \delta_1 < 1 \\ U_2 =& \quad U_{\mathrm{x}_{2+}} - U_{\mathrm{x}_{2-}} = U_\mathrm{DC}(\frac{1}{2} - \delta_2), \quad 0 < \delta_2 < 1. \end{aligned} \tag{3.12}$$

In accordance with the explanations given in the introductory chapter on the development of magnetic bearing technology, the amplifier and the magnetic bearing are also considered as a single unit in this context. According to (3.12), the inverter can be modeled as a dynamic-free proportionality factor ($G_\mathrm{B6}(s) = \pm U_\mathrm{DC}$[24]) between the duty cycle and its (mean) output voltage (including an offset of $U_\mathrm{DC}/2$). In contrast, the mathematical model of the electrical subsystem of the magnetic bearing (a pair of coils) can essentially be considered as a resistive inductor from the amplifier's point of view. Its transfer function in the Laplace domain is calculated as follows for a pair of coils (according Figure 3.8)

$$G_\mathrm{AMB,e}(s) = \frac{I(s)}{U(s)} = \frac{1}{R + sL} = \frac{1/R}{1 + s\tau}. \tag{3.13}$$

with the resistance R and inductance L of the coil pair. The parameters per coil pair are as follows: resistance $R \approx 100\,\mathrm{m\Omega}$, inductance (lowest value) $L \approx 750\,\mathrm{\mu H}$. This results in a time constant of $\tau = L/R = 7.5\,\mathrm{ms}$. Since the time constant τ is many times larger than the cycle time T_S, the assumption of linear current ramps in Figure 3.9 is justified.

The inductance of the coil pair is inherently subject to variation with the radial rotor position. The design of the current controller is based on the assumption of minimal inductance[25].

---

[24] The following should be noted with regard to the sign convention: The plus sign applies to the voltage U_1, which increases in proportion to the duty cycle δ_1. Since the voltage U_2 decreases with increasing duty cycle δ_2, the negative sign applies in this case. This must be taken into account when implementing the current controller in the DSP.

[25] This scenario is considered the least favorable in terms of current controller stability.

3.2.3 Current Controller

3.2.3.1 Control loop

The current loop is embedded in the higher-level position loop, i.e. it is a subordinate controller[26]. Consequently, the output of the position controller[27] is the input reference signal r for the current control loop, a concept clearly illustrated in Figure 3.10. The controller analyzes the error signal e and outputs a corresponding pulse pattern u via the PWM outputs of the DSP. This regulates the voltage v across the AMB coils, thereby setting the required current y. From the fundamentals, it is evident that the current generates an air gap field, which consequently exerts a force on the rotor.

The control loop is classified as an output feedback control system, where the output variable y to be controlled (in this case, the current) is measured and fed back. Shunt resistors located in the lower half of the half bridges act as sensors (low-side shunt resistors $R_{\text{sh},1}$, $R_{\text{sh,M}}$, $R_{\text{sh},2}$; see Figure 3.8). The voltages $U_{\text{I},1}$, $U_{\text{I,M}}$ and $U_{\text{I},2}$, which correspond to the currents, are amplified and converted into a digital signal in the DSP by means of an ADC and thus made available to the implemented control loop.

Since the bandwidth of this amplifier is at least one order of magnitude larger than the desired bandwidth of the closed loop, the current sensor can be modeled as a dynamic-free proportionality factor.

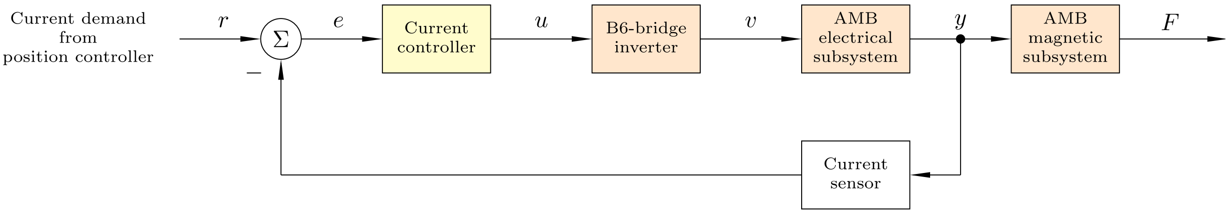

Figure 3.10: Subsidiary control loop of the active magnetic bearing's current.

While the configuration of the current sense resistors is advantageous for a simple voltage measurement, it should be noted that current measurement is only possible as long as the corresponding lower switch is activated. Consequently, at the beginning of each cycle, all the lower switches are active. The measurement of the three currents takes place during the time T_{min} (see the gray shaded area in the corresponding diagrams in Figure 3.9), and only after this protection time has elapsed, the lower switches can be deactivated and the upper switches activated. Thus, the two duty cycles δ_1 and δ_2 are limited by upper and lower values, respectively.

3.2.3.2 Controller structure

The sufficiency of a simple linear current controller is evident given the stability of the system (combination of amplifier and actuator) and the actuator's reasonable approximation to linearity around an operating point. In this thesis, a proportional-integral (PI) controller[28] is chosen for the current control loop.

The controller design according to the frequency characteristic method for sampling systems is described

---

[26] The complete control loop structure is illustrated in the Section 3.5 entitled "Hardware and Firmware Architecture".

[27] According to the prevailing principles of mechanics, the output of the position controller is defined as a force. However, due to the linear conditions that prevail around the operating point, $F \propto I$ applies.

[28] The integral part is required to eliminate a steady-state control error.

in detail in [15]. The determination of the two controller coefficients, $k_{\mathrm{IC,P}}$ and $k_{\mathrm{IC,I}}$, of the discrete PI current controller can be achieved by the use of the system and sensor parameters presented in Table 3.4.

amplifier TF $G_{\mathrm{B6}}(s)$ (V)	U_{DC}
DC link voltage U_{DC} (V)	33
AMB (el. subsys.) TF $G_{\mathrm{AMB,e}}(s)$ ($\mathrm{A\,V^{-1}}$)	$\frac{1/R}{1+s\tau}$
coil pair resistance R (mΩ)	100
coil pair inductance L (µH)	750
time constant τ (ms)	7.5
sampling time T_{S} (µs)	20
current controller P part $k_{\mathrm{IC,P}}$	0.53
current controller I part $k_{\mathrm{IC,I}}$	0.0005

Table 3.4: Specifications of the plant used for the design of the discrete PI current controller.

The difference equation which is implemented in the DSP therefore follows this formulation

$$\begin{aligned} e_{\mathrm{k}} &= r_{\mathrm{k}} - y_{\mathrm{k}} \\ u_{\mathrm{k}} &= k_{\mathrm{IC,I}}\, x_{\mathrm{k}} + k_{\mathrm{IC,P}}\, e_{\mathrm{k}} \\ x_{\mathrm{k+1}} &= x_{\mathrm{k}} + e_{\mathrm{k}}. \end{aligned} \tag{3.14}$$

The error e at the corresponding sampling time k is calculated, then the required manipulated variable u is derived and finally the error is summed (numerical integration) in the internal controller state x.

3.2.4 Design Validation

As mentioned at the beginning of this chapter, validation must be carried out simultaneously or at least at the end of the active magnetic bearing design process to ensure that the requirements are met.

The key parameters of the AMB are thus validated by comparing calculated, simulated and measured values.

3.2.4.1 Temperature measurement

First, a long-term thermal test is performed to evaluate the winding temperature of the magnetic bearing over time under the required static load conditions[29].

For the purpose of this experiment, the actuator for the x-direction (coil pairs x_1 and x_2) and for the y-direction (coil pairs y_1 and y_2) are current fed.

As shown in Figure 3.7b, the actuators are arranged orthogonal to each other. To achieve a more even distribution of the thermal load, they are mounted at a 45° angle with respect to the direction of gravity in the test stand. This means that the static load $F_{\mathrm{R,stat}}$ is distributed evenly[30] and that each of the

---

[29] The heating of the stator induced by eddy currents is not considered in this measurement because the coils are supplied with direct current.

[30] A symmetrical structure would be required for precise distribution.

four actuators only needs to carry a load of $F_{\mathrm{R,stat}}/(2\sqrt{2})$. The theoretical load per actuator amounts to $F'_{\mathrm{R,stat}} = 40\,\mathrm{N}/(2\sqrt{2}) = 14\,\mathrm{N}$ and with (2.34) (at $x = 0$) the coil currents can be estimated. In the two upper winding pairs x_1 and y_1 the theoretically required current is equal and amounts for a certain operating point ($I_0 = 7\,\mathrm{A}$, $\delta_0 = 1100\,\mathrm{\mu m}$) to

$$I_1 = I_0 + I_{1,\mathrm{c}} = I_0 + \frac{F'_{\mathrm{R,stat}}}{k_\mathrm{I}(I_0)} = 7\,\mathrm{A} + \frac{14\,\mathrm{N}}{7\,\mathrm{N\,A^{-1}}} = 9\,\mathrm{A}, \tag{3.15}$$

and in the two lower ones (x_2 and y_2) to

$$I_2 = I_0 - I_{1,\mathrm{c}} = I_0 - \frac{F'_{\mathrm{R,stat}}}{k_\mathrm{I}(I_0)} = 7\,\mathrm{A} - \frac{14\,\mathrm{N}}{7\,\mathrm{N\,A^{-1}}} = 5\,\mathrm{A}. \tag{3.16}$$

The theoretically required current along with the maximum winding temperature[31], reached during the long-term test are shown in Table 3.5 for a variety of AMB operating points (bias current I_0 and air gap width δ_0).

I_0, δ_0	I_1, I_2	max. temp.
7 A, 1100 µm	9 A, 5 A	96 °C
6 A, 1100 µm	8.25 A, 3.75 A	84 °C
7 A, 800 µm	8 A, 6 A	87 °C
6 A, 800 µm	7.18 A, 4.82 A	75 °C

Table 3.5: Required actuator currents at static load $F_{\mathrm{R,stat}} = 40\,\mathrm{N}$ for different operating points and the winding temperatures reached during the long-term test.

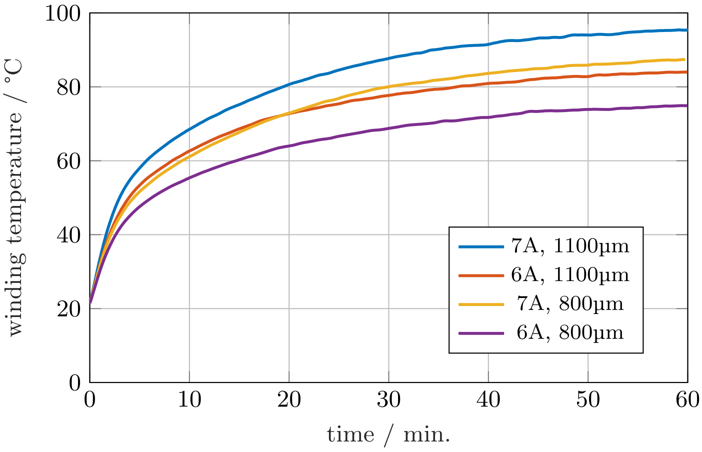

Figure 3.11: Winding temperature on the outside of the coils for different magnetic bearing operating points (I_0, δ_0).

Figure 3.11 shows the heating process of an upper coil pair, while the entire system is under a theoretical static load of $F_{\mathrm{R,stat}} = 40\,\mathrm{N}$. The (cooler) outer windings nearly reach a temperature of 100 ° °C and as

---

[31] The winding temperature is measured using the LMT87 analog temperature sensor from Texas Instruments Incorporated. Due to the size of the sensor, it is only possible to measure the winding temperature on the outside. The inside of the coil will have a higher temperature due to the absence of convection.

the stator and the bobbins are designed to withstand winding temperatures of about 150 °C, the thermal stress on the AMBs is lessened by reducing, both the bias current and air gap width.
At this early stage of the design process, before the rotor shaft is machined, this mechanical design change is not a problem. With an air gap width of $\delta_0 = 800\,\mu\text{m}$ an important parameter for the design of the AMB is now fixed.
The bias current I_0 also has an influence on the parameters k_I and k_x. In any case, implementing the current controller in software facilitates modifying the bias current with minimal effort, even during operation.

3.2.4.2 Flux density

The next step in the validation process is to measure the magnetic flux density in the air gap with a gaussmeter[32]. The flux density is the fundamental parameter that determines the force generated by the AMB on the rotor.

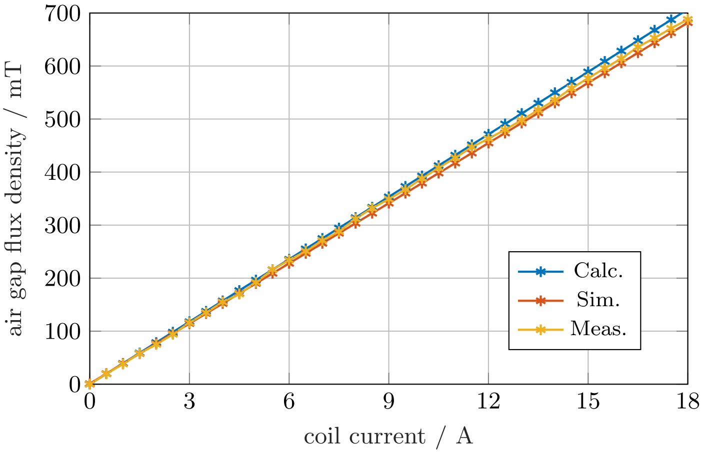

Figure 3.12: Magnetic flux density B_g in the air gap as a function of the coil current for a constant air gap length $\delta_0 = 800\,\mu\text{m}$.

Figure 3.12 shows the magnetic flux density in the air gap as a function of the coil current when the air gap is kept constant $\delta_0 = 800\,\mu\text{m}$. In the practical execution of the measurement, both pairs of coils of the actuator were supplied with the same current[33] to achieve an approximate balance of forces and thus simplify the mechanical setup[34].
The curve shows the excellent agreement between the calculated, simulated and measured values, confirming the accuracy of both the analytical and FEM models. Furthermore, a linear relationship between current and flux density is observed, indicating the absence of saturation effects, these would result in a flattening of the characteristics.

---

[32] Model 5180 Hall Effect Gauss- /Teslameter of F.W.Bell®

[33] The coils are supplied with direct current, thus ignoring the potential influence of any eddy currents that may be present.

[34] According to Equation (2.8), the measured air gap flux density of $B_\text{g} = 0.7\,\text{T}$ would result in a force of approximately 160 N.

3.2.4.3 Force measurement

The following measurements were carried out on the finalized test stand, but are already presented in this chapter as they are thematically related to the validation measurements of the magnetic bearing.

The purpose of these measurements is twofold: first, to once again facilitate a comparison between the models and the actual AMBs, and second, to derive the fundamental parameters k_{I} and k_{x}, which are essential for the subsequent design of the position controller.

Figure 3.13 shows a cross-sectional view of the test stand along the y-z plane. In addition to the sensors for rotor position measurement, the figure shows the actuators 1 and 2 in the y-direction and their currents. The parameter k_{I} corresponds to the gradient of the force-current characteristic. It can be concluded that the determination is essentially reduced to the measurement of the required control current $I_{1,\mathrm{c}}$ and $I_{2,\mathrm{c}}$ when the load F_{ext} is varied. It is essential that both the gravitational force F_{G} and the additional force F_{ext} are transformed into the magnetic bearing coordinate system to ensure accurate evaluation.

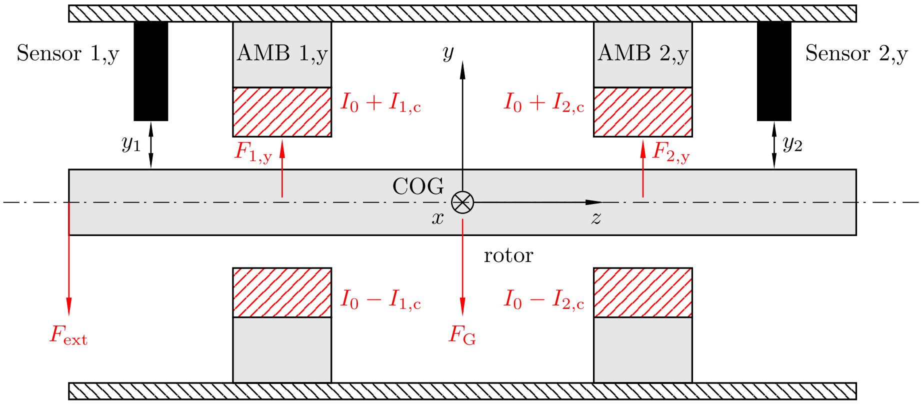

Figure 3.13: Cross-sectional view of the test stand along the y-z plane. The force-current characteristic is recorded by varying the force F_{ext} and measuring the control currents $I_{1,\mathrm{c}}$ and $I_{2,\mathrm{c}}$.

This measurement is performed for different rotor positions, x and y. The force-displacement characteristic of the magnetic bearing and thus its negative stiffness k_{x} (corresponding to the gradient of this characteristic) can be determined from this series of measurements. Additionally, each series is performed for the actuators in the x- and y-directions of the two magnetic bearings 1 and 2. This results in a total of four series of measurements, the results of which are expected to be very similar due to the symmetrical conditions. Therefore, no distinction is made between $I_{1,\mathrm{c}}$, $I_{2,\mathrm{c}}$ and the control current is labeled I_{c}. This is also true for the rotor displacements, x and y, just denoted as x.

Figures 3.14 ($I_0 = 3\,\mathrm{A}$) and 3.15 ($I_0 = 5\,\mathrm{A}$) show, that the force-current characteristic of the AMB exhibit a variation for different bias currents, with the rotor positioned in the center[35]. This proportionality between the gradient of the characteristic curves and the bias current is also ephasized by Equation 2.32. However, while the calculation and simulation show a high degree of correlation, the measured values differ slightly. This can be attributed to an eccentricity between the AMB rotor package and the rotor shaft surface in the area of the position sensors. As a result, the AMB rotor package is not perfectly aligned with the center of the AMB stator. This problem will be discussed in more detail later in the Chapter 4.

---

[35] To facilitate optimal visualization, the characteristic curves have been plotted for positive control currents only. It can be seen that the characteristics are odd functions due to the symmetrical configuration of the actuators. Consequently, they are symmetric with respect to the origin.

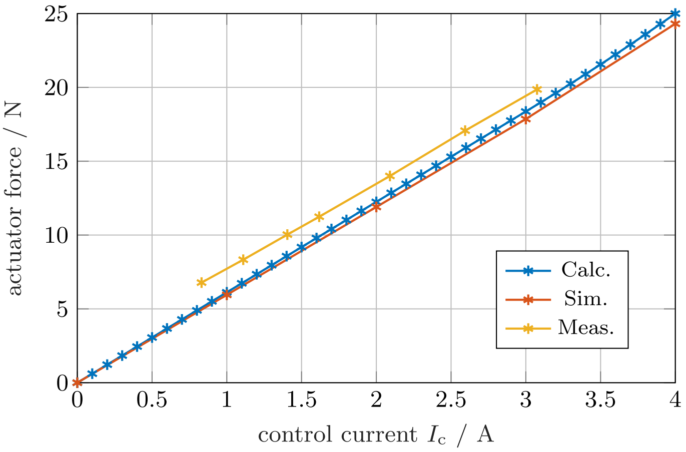

Figure 3.14: Force-current curve for a bias current of $I_0 = 3\,\mathrm{A}$ and the rotor at center position $x = 0\,\mu\mathrm{m}$.

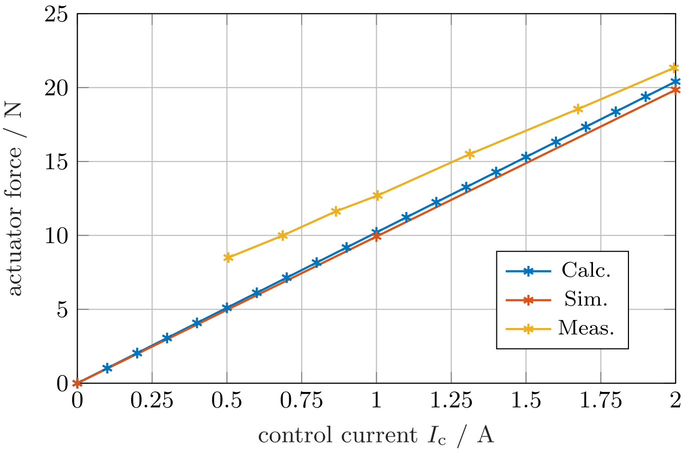

Figure 3.15: Force-current curve for a bias current of $I_0 = 5\,\mathrm{A}$ and the rotor at center position $x = 0\,\mu\mathrm{m}$.

From this series of measurements it can be shown, that the parameter k_I depends on the control current I_c and the parameter k_x on the rotor position x. This will be discussed again in the subsequent section[36].

3.2.4.4 Determination of key parameters k_I and k_x

As previously mentioned, the two parameters k_I and k_x are defined as the gradient of the force-current and force-displacement characteristics.

The determination of these parameters is achieved by approximating the corresponding characteristics by a piecewise 3rd order polynomial, followed by the formation of the derivative of this function.

Figure 3.16 illustrates the relationship between the force-current factor k_I and the control current I_c for two different bias currents. For a bias current of $I_0 = 3\,\mathrm{A}$ the measured curves show a relatively good agreement with the results of the analytical model and the simulation. However, the evaluation of the measured values for $I_0 = 5\,\mathrm{A}$ are more than 10 % below the values obtained from the calculation or simulation.

---

[36] It is noteworthy that the parameter k_I is also affected by the rotor position, while the parameter k_x is also affected by the control current. However, these dependencies remain unexamined.

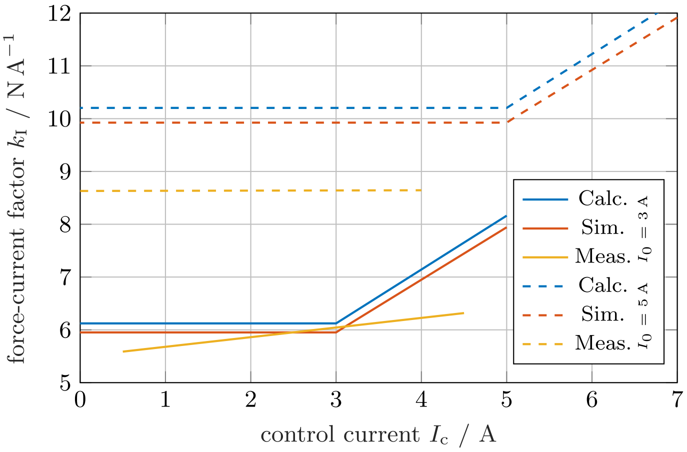

Figure 3.16: Force-current factor k_I of the AMB for bias currents $I_0 = 3\,\mathrm{A}$ and $I_0 = 5\,\mathrm{A}$.

The region in which the control current exceeds the bias current is of special interest. Since the actuator current can only take positive values, the term $(I_0 - I_\mathrm{c})^2$ in Equation (2.29) becomes zero for $I_\mathrm{c} > I_0$, and the current in one of the actuators becomes zero. This reduces Equation 2.29 to

$$F = \frac{N^2 \mu_0 A_\mathrm{g}}{4} \frac{(I_0 + I_\mathrm{c})^2}{\delta_0^2} \qquad \text{for: } x = 0,\ I_\mathrm{c} > I_0. \tag{3.17}$$

The derivation with respect to the control current I_c, as shown in Equation (2.32), yields the following

$$k_\mathrm{I} = \frac{N^2 \mu_0 A_\mathrm{g}}{4} \frac{\mathrm{d}}{\mathrm{d}I_\mathrm{c}} \left[\frac{(I_0 + I_\mathrm{c})^2}{\delta_0^2} \right] = \frac{N^2 \mu_0 A_\mathrm{g}}{4} \frac{2(I_0 + I_\mathrm{c})}{\delta_0^2} \qquad \text{for: } x = 0,\ I_\mathrm{c} > I_0. \tag{3.18}$$

This result emphasizes the linear proportionality between k_I and the control current I_c in the region, where $|I_\mathrm{c}| > I_0$.

Figure 3.17 shows the dependence of the force-displacement factor k_x on the displacement x. While the measurements are sufficient for preliminary design verification and for determining the force-displacement factor k_I, it is noticeable that the first inconsistencies become visible at this stage.

The discrepancy in the measurement results for a bias current of $I_0 = 5\,\mathrm{A}$ can be attributed to an eccentricity between the AMB rotor package and the surfaces of the rotor shaft intended for position measurement. The spatial offset of the graph (yellow dashed line) by $\approx 40\,\mathrm{\mu m}$ further supports this hypothesis.

It may be necessary to repeat the measurement for a bias current of $I_0 = 3\,\mathrm{A}$, since the deviation of the measurement results from the calculated and simulated data is greater than 50 %.

As shown in Figure 3.17, the force-displacement factor shows a significant dependence on displacement. To illustrate this dependency more clearly, the characteristic of k_x (calculated and simulated values) for a bias current of $I_0 = 5\,\mathrm{A}$ is shown in Figure 3.18 in conjunction with a quadratic function, whose purpose is to illustrate the quadratic relationship between k_x and displacement x.

The analytical derivation of the above relationship is achieved by means of the Equation (2.33), which shows the derivation of the force-displacement factor of the double reluctance actuator. The third line is

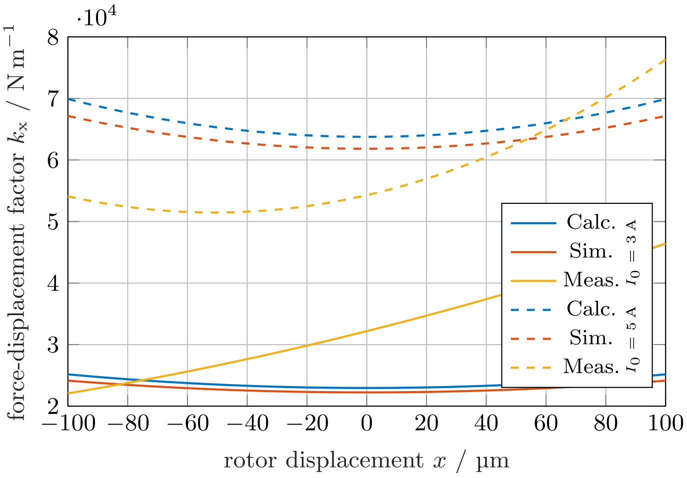

Figure 3.17: Force-displacement factor (negative stiffness) k_x of the AMB for bias current $I_0 = 3\,\mathrm{A}$ and $I_0 = 5\,\mathrm{A}$.

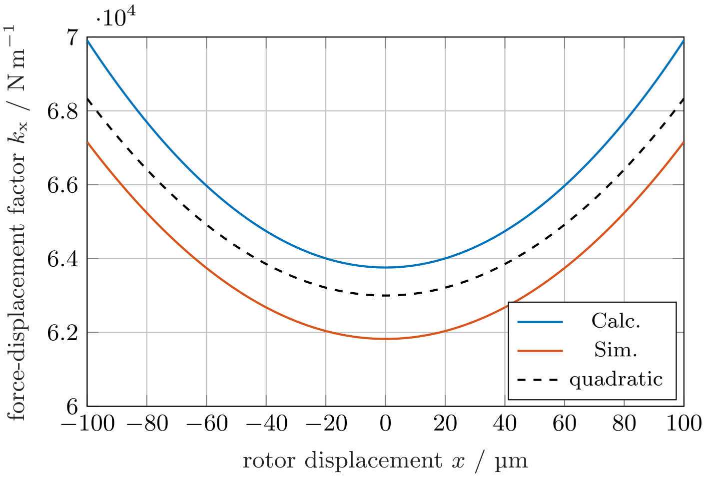

Figure 3.18: Force-displacement factor k_x for bias current $I_0 = 5\,\mathrm{A}$; comparison of the calculated and simulated curves with a quadratic one.

of particular interest

$$k_\mathrm{x} = \frac{I_0^2 N^2 \mu_0 A_\mathrm{g}}{2} \left\{ \frac{1}{(\delta_0 - x)^3} + \frac{1}{(\delta_0 + x)^3} \right\} = k_0 \left\{ \frac{1}{(\delta_0 - x)^3} + \frac{1}{(\delta_0 + x)^3} \right\} \tag{3.19}$$

Performing a Taylor series expansion of the last expression in the curved bracket around the point $x = 0$ yields

$$\frac{1}{(\delta_0 \pm x)^3} = \frac{1}{\delta_0^3} \left(1 \mp 3\frac{x}{\delta_0} + 6\frac{x^2}{\delta_0^2} \mp 10\frac{x^3}{\delta_0^3} + 15\frac{x^4}{\delta_0^4} \dots \right). \tag{3.20}$$

The sum of the two expressions results in the cancellation of all odd powers and the doubling of all even powers

$$k_\mathrm{x} \propto \frac{2}{\delta_0^3} \left(1 + 6\frac{x^2}{\delta_0^2} + 15\frac{x^4}{\delta_0^4} + \mathcal{O}(x^4) \right). \tag{3.21}$$

This Taylor series expansion shows that the characteristics of $k_\mathrm{x}(x)$ depend on the x/δ_0 ratio. For $x \ll \delta_0$, $k_\mathrm{x}(x)$ appears to be constant, but with increasing displacement x a quadratic dependence can be observed, and so on.

For the chosen air gap width $\delta_0 = 800\,\mu\mathrm{m}$ and the maximum displacement $x = 100\,\mu\mathrm{m}$ the characteristic of $k_\mathrm{x}(x)$ is mainly a quadratic one as can be seen in Figure 3.18. Hence, it can be expressed as the sum of a constant value k_0 and a quadratic function in x

$$k_\mathrm{x}(x) \approx k_0 \left(1 + 6\frac{x^2}{\delta_0^2}\right). \tag{3.22}$$

The results of the investigations show that the factors k_I and k_x are not only subject to uncertainties (due to manufacturing tolerances, saturation effects, unmodeled scattering, etc.), but also show systematic dependencies on the control current and the rotor position. It is essential to take this into account when designing a robust position controller.

3.2.5 Non-ideal Coupling and Reaction Forces

3.2.5.1 Cross coupling effects

In the previous section, the influence of the rotor displacement and the control current on the two parameters k_I and k_x was analyzed. In this section, the topic of cross couplings and the influence of a drive machine on the magnetic bearings will be briefly discussed.

In the previous analyses it was generally assumed that the rotor was at the operating point, i.e. $x = 0$. Manufacturing tolerances and inaccuracies always result in inherent unbalances and eccentricities of the rotor shaft and the magnetic bearing itself. Consequently, the rotor does not remain centered during operation, resulting in an orbit-like trajectory.

Extensive simulations have shown that if the magnetic bearing rotor is not exactly at the magnetic center, the control currents not only induce a force in the desired direction, but also generate a component orthogonal to it. This so-called cross-coupling factor k_IXY describes the relationship between the current in the x direction and the force in the y direction and vice versa, since it is a reciprocal system. The factor was found to be strongly dependent on the size and direction of the orbit; however, it was found to play a minor role for the magnetic bearing system in question compared to $k_\mathrm{I} = k_\mathrm{IXX}$.

The negative stiffnesses of the two actuators of a magnetic bearing are also coupled, i.e. a movement in the x-direction causes a force in the y-direction and vice versa due to reciprocity. Similar to k_IXY, this cross-coupling factor is also dependent on the direction and the size of the orbit[37].

3.2.5.2 Drive unit induced forces

As mentioned in the introduction of this chapter, it may occur that the drive unit exerts radial forces on the rotor shaft in addition to torque. The subsequent investigation by simulation will seek to determine the origin of these forces and identify the most effective modeled approach, using a PMSM as an example.

---

[37] Both cross-coupling factors, k_IXY and k_xXY, amount to a maximum of 20 % of the corresponding factors in the main direction, k_IXX and k_xXX. Consequently, the influence of these additional factors can be neglected in this AMB configuration.

When the rotor of a PMSM is perfectly aligned with its stator, the radial forces exerted by the magnets and the stator field cancel each other out completely, resulting in no force on the rotor shaft. However, if the rotor shaft is supported by AMBs, it may be displaced from its center position due to unbalance forces, resonance, or static eccentricity. In this case, the PMSM magnets generate radial forces because of the inverse quadratic relationship between reluctance force and distance.

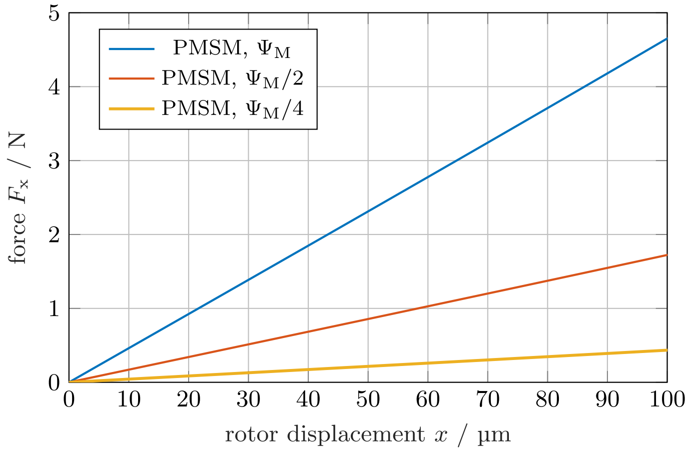

Figure 3.19: Force F_x induced on the rotor shaft by a PMSM for different permanent magnet fluxes Ψ_M.

The challenge with this simulation is that the resulting forces on the rotor shaft vary greatly depending on the PMSM design selected. In order to obtain comparable simulation results, only the permanent magnet flux Ψ_M and the phase current are varied in a specific PMSM design in such a way, that the same torque is always delivered by the machine.

Figure 3.19 shows the force-displacement diagram for the different PMSMs, all delivering the same amount of torque. The permanent magnet flux apparently has a major influence on the motor's reaction to the rotor shaft.

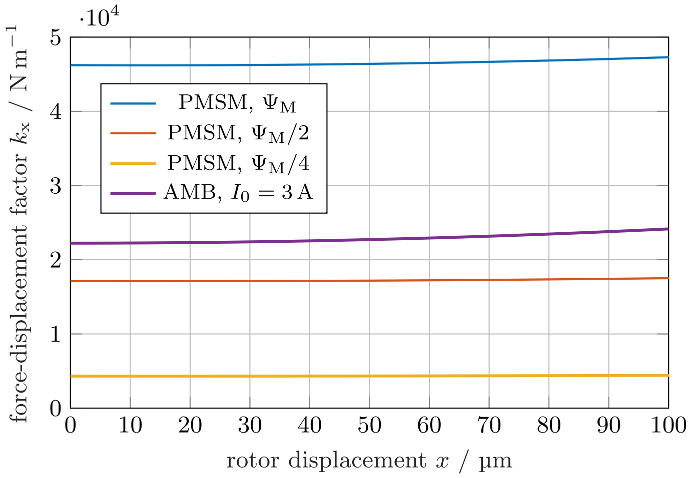

Figure 3.20: Force-displacement factor k_x induced by the drive unit compared to the negative stiffness of the magnetic bearing for a bias current $I_0 = 3$ A.

Figure 3.20 provides a comparison between the force-displacement factors of the PMSMs and the negative stiffness of the AMB, used in this test stand for a bias current of $I_0 = 3\,\mathrm{A}$. The same quadratic relationship between k_x and displacement x can be observed as in Figure 3.18. This is not surprising, since the configuration of the PMSM is analogous to a double reluctance actuator from a magnetic point of view. However, the quadratic effect is less pronounced than that observed with the AMB, which is due to the larger air gap used in the drive unit for safety reasons ($\delta_\mathrm{PMSM} = 1500\,\mu\mathrm{m}$). For this particular case, the negative stiffness of the PMSM is within the range of that of theAMB. Hence, the influence of the PMSM must be considered as an additional negative stiffness component in the design of the position controller to ensure stability, in this particular case.

Therefore, optimization can take place here between the air gap length (large air gap linearizes the course of $k_\mathrm{x}(x)$), the magnetic flux Ψ_M, and the phase current.

3.3 Position sensors

The rotor is considered a rigid body, which is permissible for frequencies far below the first bending mode[38]. Rigid bodies have six degrees of freedom - three rotational and three translational. Under the preconditions specified in Section 2.5.2, the movement of the rotor shaft in the axial and radial directions can be decoupled. Additionally, the mechanical design of the rotor packages ensures self-stabilization in the axial direction. Thus, the use of a thrust magnetic bearing and an axial position sensor is not necessary.

The remaining four degrees of freedom are the translation in x- and y-direction and the rotation around the x- and y-axes (α and β) in the COG coordinate system. Four ES-S2[39] inductive eddy current sensors are used for the non-contact measurement of these parameters. As shown in Figure 3.21, each pair of sensors arranged orthogonally to each other forms a sensor plane (1 and 2). In each plane, the position of the rotor shaft is determined - x_1, y_1 on plane 1; x_2, y_2 on plane 2. For the control strategy used, the position of the rotor shaft in the COG coordinate system is relevant. Hence, the measured distance values have to transformed from the respective sensor coordinate system into the COG to determine the rotor shaft position in the COG coordinate system. More details on the geometry and the different coordinate systems can be found in Section 2.5.3 on the dynamics of magnetically levitated rotors.

3.3.1 Principle of operation

The eddy current effect is the basic physical measuring principle of the sensor. For more details on the causes of eddy currents, see Section 2.4. The sensing element of such sensors is a reactive element, i.e. a coil, whose impedance is influenced by a nearby target [16].

Assuming the target is within the sensor's detection range, two cases can be distinguished in principle. If the target material is non-ferromagnetic but electrically conductive, e.g. aluminum, eddy currents are induced in the (electrically conductive) target object according to Faraday's law. The inductive reactance component of the impedance decreases because the magnetic field created by the eddy currents counteracts and weakens the magnetic field of the coil. If the target is an ideally non-conducting ferromagnetic material,

---

[38] According to a finite element simulation in SolidWorks® and ANSYS® Mechanical™, the frequency of the first bending mode is in the range of 800 Hz.

[39] MICRO-EPSILON-MESSTECHNIK GmbH & Co. KG, Ortenburg, Deutschland, www.micro-epsilon.de

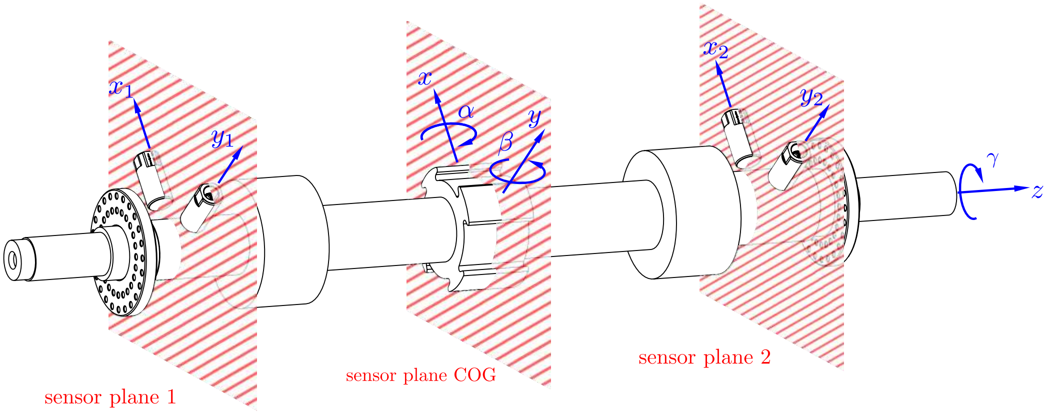

Figure 3.21: The test stand has two sensor planes 1 and 2 and with the two sensor pairs four distances (x_1, y_1, x_2, y_2) can be measured. A transformation from the respective sensor coordinate system into the COG, yields the rotor shaft position in the COG coordinate system.

then no eddy currents will be formed. Due to the material's magnetic permeability ($\mu_\mathrm{r} \gg \mu_0$), the target acts as a low reluctance path for the sensor coil's magnetic field, increasing the coil's inductive reactance component. If the target material is both conductive and ferromagnetic, the ferromagnetic and eddy current effects superimpose [17].

3.3.2 Calibration

The absolute accuracy, offset, linearity, and gain of the distance measurement all depend on a number of material parameters. The most important of these are the electrical conductivity and magnetic permeability of the target material. For this reason, the manufacturer of the measuring system provides a factory calibration for two possible reference materials - these are either steel (material designation: 1.0037) or aluminum (material designation: 3.1645). The measuring system used is equipped with a calibration board for aluminum.

Without going into too much detail on field distribution, it should be mentioned that the target's shape also has a significant influence on the measurement. Factory calibration is performed with a flat target, whose size is at least twice the sensor diameter and whose thickness is several times the penetration depth of the eddy currents.

In principle it is possible to measure on curved surfaces, but the recommended minimum diameter for this is a least ten times the sensor diameter. For the sensor, used in this application the minimum diameter is in the range of more than 100 mm. This would require the use of an aluminum sensor disc with a large diameter, mounted on the rotor shaft, to accurately measure the displacements. However, to prevent any eccentricities no discs are mounted on the rotor shaft for the position sensors. Instead, the possibility of measuring directly on the highly curved surface of the rotor shaft was investigated. In addition to the curved surface, the target material (machining steel, material designation: 1.0737) differs from the calibration material.

The following illustration in Figure 3.22 provides a brief insight into the complex relationships. It shows the qualitative magnetic field distribution between a inductive distance sensor and the rotor shaft. The simulation was performed using the FEMM[40] software.

The image shows a cross section of the magnetic field **B** along the sensor plane 1 (Figure 3.21), with the rotor shaft at the bottom and the eddy current sensor (red dashed line) with its coil (copper colored) positioned at the top at a distance of about 1 mm.

When measuring on curved surfaces, the measured distance lies somewhere in between the values of the nearest and farthest field lines. This measured value does not correspond to the actual distance between the apex and the sensor, but is larger (see also Figure 3.23). Figure 3.22 also shows that lateral movement in y_1-direction affects the distance measurement in x_1-direction when measuring on curved surfaces. This is especially true for a magnetically levitated rotor shaft, moving along an orbit as opposed to a direct line.

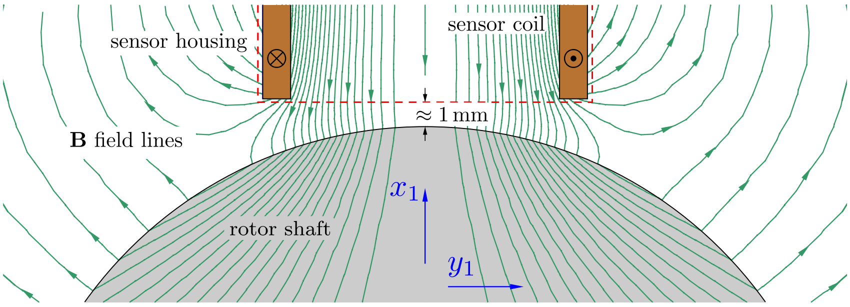

Figure 3.22: Finite element simulation of the magnetic field lines **B** between the ES-S2 sensor and the test stand's rotor shaft (section along sensor plane 1).

Due to material and shape deviations from the reference target, some recalibration is required. This is usually done using a special test stand equipped with a micrometer screw gauge. For simplicity, several plastic films of known thickness are used to adjust the distance between the sensor and the target. The measurement results for different target materials and shapes are summarized in Figure 3.23. For the flat aluminum target (electrical conductivity: $\sigma_{\mathrm{Al}} = 37.7\,\mathrm{MS\,m}$) the measurement results agree well with the expected behavior according to the data sheet. At an actual distance of 200 µm (start of measuring range)

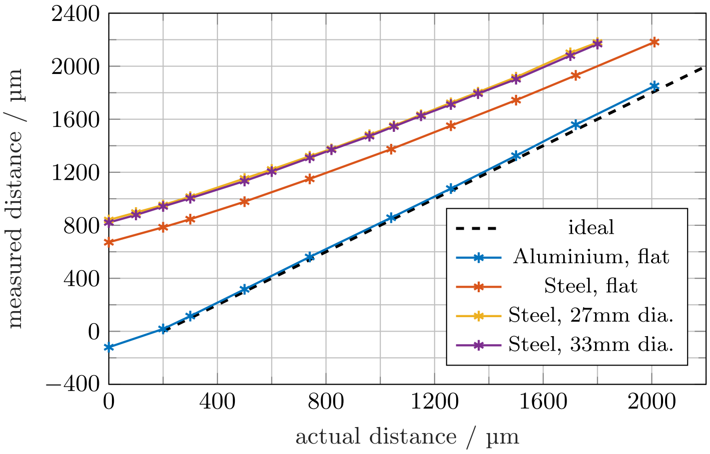

Figure 3.23: Recalibration measurement of inductive position sensor ES-S2 for different target materials and shapes.

---

[40] FEMM, Finite Element Method Magnetics - David Meeker, Ph.D., dmeeker@ieee.org

the output is zero, while at a distance of 2200 µm (end of measuring range) the output, i.e. the measured distance, is about 2000 µm. The slight deviation from the ideal curve (black dashed line) may be due to thickness tolerances of the plastic films or a slightly too small target, i.e. less eddy currents are induced and therefore the distance is overestimated.

The red curve shows the measurement values for a flat steel target. The curve shows an offset, gain, and linearity error. The target material (machining steel, electrical conductivity: $\sigma_{\mathrm{St}} = 8.3\,\mathrm{MS\,m}$) is ferromagnetic and conductive, so the ferromagnetic and eddy current effects occur [17].

However, the eddy current effect is less pronounced because the electrical conductivity of machining steel is only about one-fifth that of aluminum. Therefore, the distance is overestimated by the measurement system. In addition, the ferromagnetic property of the target material partially compensates for the field weakening of the eddy currents, but further investigation would be required to clearly separate the two superimposed effects on the sensor characteristic.

The yellow and purple graphs show the values for the round target material (27 mm and 33 mm). When compared to the flat target of the same material (red graph), curved surfaces cause additional distance error (increased values).

3.3.3 Linearization

For the intended application, only a relative distance measurement is sufficient, so the error in both offset and gain is not a significant issue.

To investigate the linearity error, Figure 3.24 shows the gain error as a function of the distance. In essence, this is the deviation of the slope of the characteristic curve (see Figure 3.23) from the ideal, expressed as a percentage. At first glance, the distance measurement appears to be of limited use due to the significant gain variations that are evident across the measurement range for the machining steel target, both flat and curved. Since the gain of the sensor directly affects the gain of the entire system (see the Section 3.5 on controller design for details), this could lead to problems in robustness.

Despite the fact mentioned above, the use of this measuring configuration is still feasible. First, the maximum possible radius of the rotor shaft orbit is limited to about 300 µm by the mechanical air gap. And second, the sensors are mounted in such a way that when the rotor shaft is floating in the approximate center of the auxiliary bearings, the actual distance between the sensors and the rotor shaft is about 1 mm each.

Assuming that it is possible to keep the trajectory in the range of maximum 100 µm to 200 µm, the gain error varies less than 6 % to 7 %. Therefore, it is possible to linearize the sensor characteristic from Figure 3.23 around a suitable chosen setpoint, e.g. 1 mm actual distance between the sensor and the rotor shaft apex. As shown in Figure 3.23 and 3.24, there is minimal difference between the two round target materials with diameters of 27 mm (yellow graph) and 33 mm (purple graph). Thus, a single gain value is sufficient for all four sensors if the actual distance between the rotor shaft and each sensor can be accurately set (±200 µm).

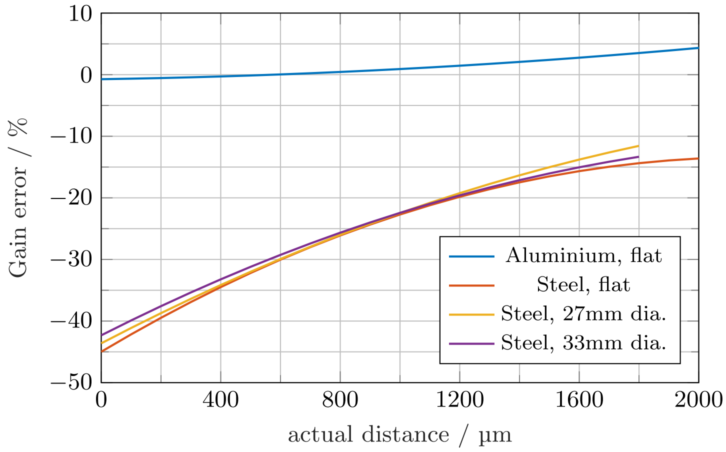

Figure 3.24: Gain error in percentage as a function of actual distance for different target materials and shapes.

3.4 Mechanical Design

This chapter provides a brief overview of the key steps and considerations involved in the mechanical design of the test stand. The drawings of the individual components can be found in the appendix.

A major design challenge is the need for modularity and flexibility to adapt the test stand to different applications. It is essential that the design is open to allow both the position sensors and the magnetic bearings themselves to be positioned in a variety of locations. In addition, the design must allow for testing with different rotor shafts. This applies in particular to their length, the frequency of the first bending mode, and the axial and polar moments of inertia.

The following design decisions were made in close consultation with the in-house workshop. The usability of the test stand is influenced by the practicability of manufacturing and the alignment of the individual components with as few tolerances as possible.

3.4.0.1 Housing

In order to achieve the required flexibility, it is essential that the stators of the drive unit and the magnetic bearings, as well as the auxiliary bearings, are accommodated in individual housings. The axial position of these housings can be chosen as required. This configuration also allows for the integration of additional drive units, thus increasing the torque. In addition, the design facilitates the installation of the position sensors on both sides of the housings.

A significant drawback of this modular approach in mechatronic systems of this type is that it significantly reduces the rigidity of the mechanical structure. The individual housings are therefore designed with a wide support base and are connected by a solid base and cover plate to avoid inherent bending vibrations. Radial alignment is a major challenge in magnetic bearing systems, and the problem is further complicated by the design, as a total of five housings (one motor stator, two AMB stators, two auxiliary bearings) must be aligned with each other. The feasible mechanical air gap is limited upward by the allowable power loss in the magnetic bearings and downward by the achievable tolerance limits and alignment quality.

There are two consequences of misalignment. First, the allowable rotor shaft orbit is reduced and second, static eccentricity is introduced into the magnetic bearings. This means that the AMB rotor package is not located at the magnetic center of the AMB stator. Due to the difference in air gap lengths, there is asymmetry in the operating points, which affects the actuator parameters k_I and k_x. To achieve the best possible alignment in the radial direction, the housings are aligned along a guide rail made of key steel.

3.4.0.2 Rotor shaft

The rotor shaft consists of several sections, including the surfaces of the auxiliary bearings, the surfaces on which the position is measured, and the rotors of the magnetic bearings. If these sections do not have the same axis of rotation, an eccentricity will occur. To be used as a test stand for investigating the dynamic effects of rotors, these eccentricities must be avoided. Therefore, the rotor shaft was designed to allow as many sections as possible to be machined in a single operation and there are no discs mounted on the rotor shaft for the position sensors to prevent any additional eccentricities.

3.4.0.3 Rotor lamination stack

The rotor packages or lamination stacks for the magnetic bearings and the drive unit are made of electrically insulated steel sheets, a measure taken to prevent the occurrence of eddy currents. Figure 3.25 shows the technical drawings of the rotors. The sheet metal blanks were precisely cut in an external workshop using a metal laser cutter.

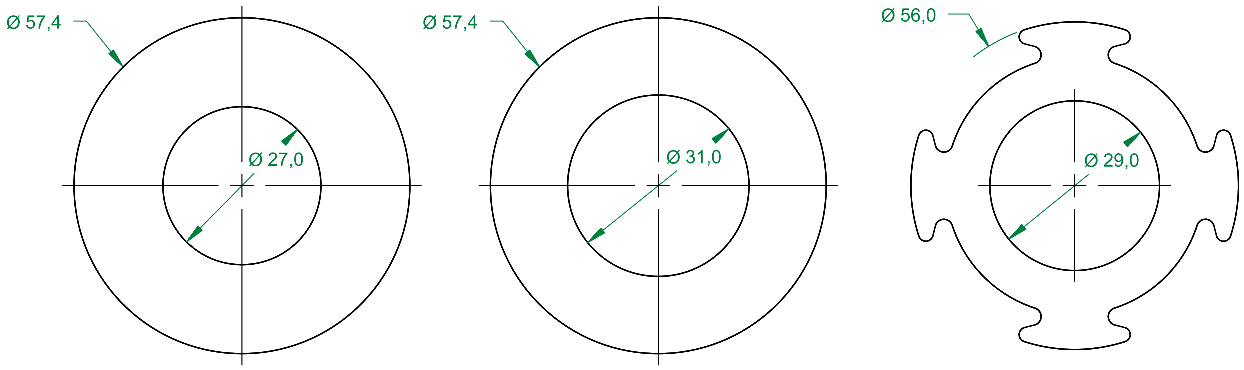

(a) Rotor of AMB A (b) Rotor of AMB B (c) Rotor of the SynRM

Figure 3.25: Drawings of magnetic bearing rotors and drive unit SynRM rotor - all dimensions in millimeters.

This raises the question of how much the cutting process negatively affects the sheets' magnetic properties. To make an estimation on this matter, test coils with toroidal cores made from sheet packages were fabricated and measured. For the toroidal cores, the test process involved the use of sheets of different thicknesses (0.5 mm, 0.2 mm) and different manufacturing methods. These methods included laser cutting of the entire sheet package, which would greatly simplify the packaging process, or packaging of individually cut sheets. In the frequency range of 10 Hz to 10 000 Hz the impedance and inductance characteristics of the coils were measured using OMICRON Lab's Vector Network Analyzer - Bode 100[41]. Without going into further detail, it should be mentioned that these results can be used to estimate the frequency range in which the test coil exhibits inductive behavior, as well as the frequency at which eddy currents become noticeable.

The results are not presented in detail here. Instead, the most important findings and conclusions are outlined briefly. As mentioned in the introductory Chapter 2.4 on eddy currents, lamination thickness significantly affects eddy current formation. The measurement results demonstrate that the thinner the electrical steel sheet, the less eddy current formation occurs and this is consistent with the findings in [7] and [8]. The cutting process itself also affects the impedance characteristics. The higher the required laser power, the smaller the frequency range within which the test coils exhibit inductive behavior.

The best results in terms of inductance and frequency response are achieved by using thin sheets that are packaged after the cutting process. However, a compromise was made regarding the rotor packages used in this thesis, so they are packaged from pre-cut sheets with a thickness of 0.5 mm.

The AMB rotor packages are most likely eccentric to the remaining surfaces of the rotor shaft after being glued to it. To overcome this issue, the sheet metal cuts for the magnetic bearing are cut with a larger outside diameter. They are then packaged and glued onto the rotor shaft. Subsequently, they are machined on the lathe to the final diameter. This was done to improve the concentricity of the AMB rotor packages with respect to the rotor shaft.

3.5 Hardware- and Firmware Architecture

This section provides a brief overview of the essential hardware components of the test stand. It shows how the individual components are connected to each other to form the overall system. A flow chart is used to present the firmware developed for the test stand, and the most important blocks are briefly explained. Finally, the structure and design of the linear position controller are described.

3.5.1 Hardware

As shown in Figure 3.26, the essential components of the test stand besides the mechanical construction are the AMBs, SynRM, position sensors, and the rotary position sensor (decoder). The hardware itself, includes inverters and various DSPs.

The DSP Leader is responsible for facilitating communication with the PC, receiving commands and parameters, and sending measurement data to the PC via MATLAB®[42]. This allows measurements to be taken and controller and filter parameters to be changed while the test stand is running.

This DSP is also responsible for processing the signals from the two pairs of sensors (1 and 2), calculating the required control variables (i.e., the target currents in the magnetic bearings), and transmitting them via the serial communications interface (SCI) to the two DSPs denoted, Follower AMB 1 and 2. These three DSPs are synchronized with each other by a synchronization signal called Sync.

The DSP Leader is connected to the DSP Follower SynRM by an additional SCI. This is used to specify

---

[41] OMICRON Lab is a division of OMICRON electronics GmbH, Oberes Ried 1, 6833 Klaus, AUSTRIA

[42] The MathWorks, Inc., 1 Apple Hill Drive, Natick, MA 01760 USA, 508-647-7000.

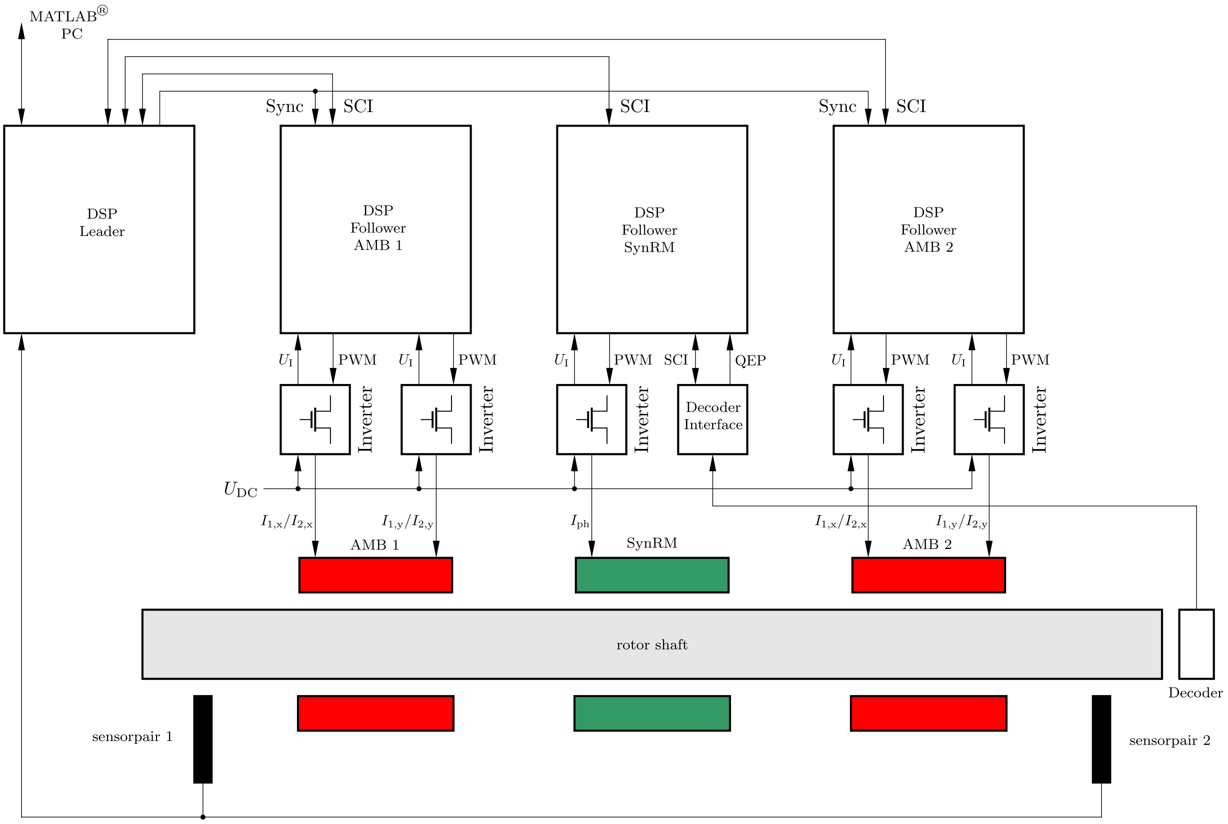

Figure 3.26: Schematic of the essential hardware components of the test stand.

a target speed and to read back the rotor angle γ.

The DSP Follower AMB 1/2 can be considered a type of intelligent current controller. The application of the specified current is achieved by controlling its two inverters using a PWM pattern. The output feedback loop of the current control is closed by measuring and feeding back the actual current in the electromagnets of the magnetic bearing ($I_{1,x}/I_{2,x}$ and $I_{1,y}/I_{2,y}$) via the voltage signal U_I - see Figure 3.8.

The FOC of the drive motor (SynRM) is implemented in the DSP Follower SynRM. The control mechanism depends on three primary variables: the speed setpoint (via SCI from the DSP Leader), the phase currents, and the rotor angle γ. The DSP reads the latter from the rotary position sensor via a decoder interface (see Section 3.1.1 on the drive unit for details).

The test stand consists of a mechanical structure with the rotor shaft as the central element to be positioned and stabilized. The position of the rotor in the sensor coordinate system is determined by the two pairs of sensors (1 and 2) and transmitted to the DSP Leader. After calculating the necessary control signals, the magnetic bearings' currents are regulated according to the application of the necessary forces (in the magnetic bearing coordinate system).

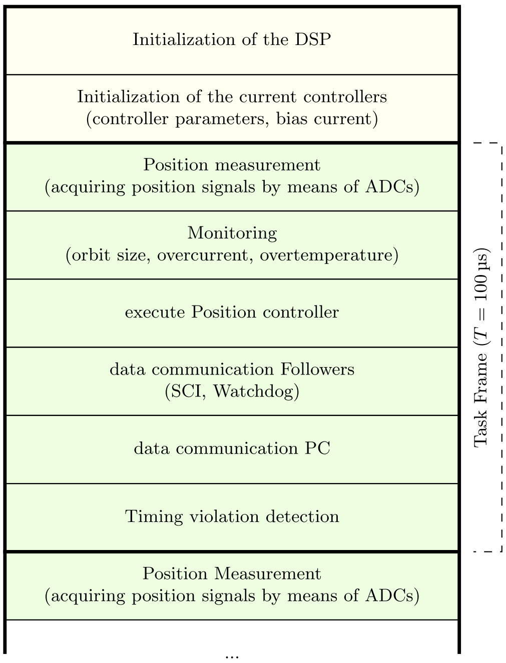

Figure 3.27: Sequential firmware execution in the DSP Leader

3.5.2 Firmware

3.5.2.1 DSP Leader

The firmware is executed sequentially in the DSP leader as shown in Figure 3.27. After initializing the DSP's peripherals and components, the controller parameters and the desired bias current are transferred to the two DSPs, responsible for current control (Follower AMB 1 and 2).

Upon successful completion of the initialization process, the task frame is processed repeatedly, its length determining the cycle time of the position controller.

The task frame consists of three basic processes: first, reading and filtering the sensor values (via ADC), second, calculating the corresponding control variables (current values) in the position controller, and third, transmitting them to the corresponding DSPs via SCI.

In addition, a monitoring process is performed within each frame. The purpose of this procedure is to verify whether the rotor orbit size[43] is within the permissible range and to ensure that both the winding temperature and the magnetic bearing current are within the permissible range.

The current control DSPs respond to the successful receipt of the target current values by returning the actual current values. If there is no response for several frames, the two magnetic bearings are deactivated (SCI watchdog).

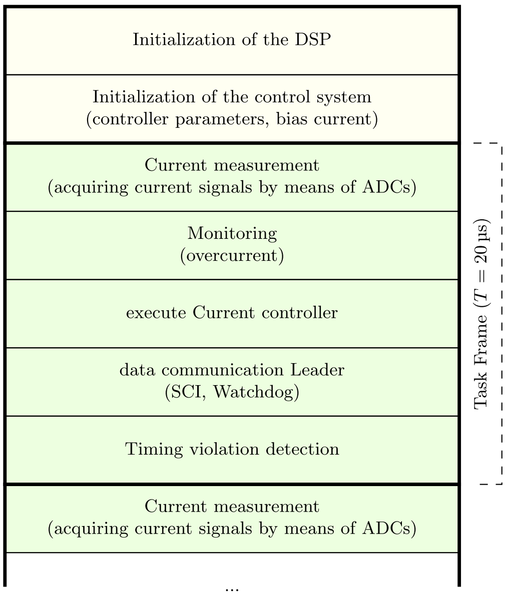

Figure 3.28: Sequential firmware execution in the DSP Follower AMB

3.5.2.2 DSP Follower AMB

Each current controller DSP goes through an initialization process with its own peripherals and components, just like the DSP leader. The controller parameters and bias current are then configured according to the requirements of the DSP leader.

The task frame, which is subject to constant repetition[44], again consists of three basic steps. First, the actual value of the variable to be controlled must be determined. In this case, the actual value of the current is read via an ADC. Then the current controller calculates the control error and uses this information to generate an appropriate pulse pattern.

Similar to the DSP Leader, the DSPs Follower AMB 1/2 monitor the magnetic bearing current and any timeout in communication with the DSP Leader (SCI watchdog).

For further analysis, the actual value of the magnetic bearing current is returned to the DSP Leader via SCI.

3.5.3 Position Controller

To perform further measurements and validate the design of the magnetic bearings, the test stand must be started up. Due to the inherent instability of AMBs, magnetic bearings must be integrated into a control loop to stabilize and control the rotor shaft's position. Of the various possible controller structures, this thesis implements a decoupled controller structure according to a procedure demonstrated, for example, in [1]. In the test stand's feedback loop (see Figure 3.26 and 3.29), position sensors measure the deflection of the rotor in the two orthogonal directions in the two sensor planes 1 and 2. These four signals are combined via a coordinate transformation into two "parallel" (translation) and two "conical" (rotation)

---

[43] For a magnetic bearing supported rotor, the orbit is simply the path that the centerline of the rotor takes in the transverse plane of the bearing as it rotates.

[44] The duration of the task frame determines the current controller cycle time.

modal or generalized coordinates, which decouples the rigid body rotor modes.

This decoupling allows the design of completely independent controllers. For the initial tests and measurements, a decoupled proportional-derivative (PD) controller with an integral part has been implemented for each of the modal channels. Therefore, a control law of the following type is designed:

Parallel (translation) mode: $$F_{\text{par}} = -I_{\text{par}} \int x \, \mathrm{d}t - P_{\text{par}} x - D_{\text{par}} \dot{x}$$

Conical (tilt) mode: $$F_{\text{con}} = -I_{\text{con}} \int \alpha \, \mathrm{d}t - P_{\text{con}} \alpha - D_{\text{con}} \dot{\alpha}.$$

The PD control law allows intuitive access via mechanical equivalents. While the proportional component (P) acts like a virtual spring ($F_{\text{par}} \propto x$ and $F_{\text{con}} \propto \alpha$), the differential component (D) acts proportional to the speed ($\dot{x}$ and $\dot{\alpha}$) and thus has a damping effect. The P-control compensates the negative stiffness k_{x} of the magnetic bearings and determines the resulting system stiffness[45], while the D-control introduces the required damping. The integral component (I) can be considered as a superspring and eliminates a steady-state control error but has no stabilizing effect [3].

In [3] it is shown how the poles of the initially unstable magnetic bearing can be shifted in the complex plane by applying a PD control law. The P-control shifts the poles from the right half-plane to the imaginary axis. When the D-control is added and damping is introduced, the poles are finally shifted to the left half-plane and the system is stabilized. For magnetically levitated rotors, the position of these poles also depends on the rotor speed due to the gyroscopic effect.

The design procedure and the specifics of magnetic bearings are not described in detail here, and can be found in [3] and [1]. The result of the design is a set of diagonal "equivalent stiffness" and "equivalent damping" matrices in COG coordinates

$$\begin{aligned} \mathbf{P} &= \operatorname{diag}[P_{\text{con}},\, P_{\text{par}},\, P_{\text{con}},\, P_{\text{par}}] \\ \mathbf{D} &= \operatorname{diag}[D_{\text{con}},\, D_{\text{par}},\, D_{\text{con}},\, D_{\text{par}}] \\ \mathbf{I} &= \operatorname{diag}[I_{\text{con}},\, I_{\text{par}},\, I_{\text{con}},\, I_{\text{par}}], \end{aligned} \tag{3.23}$$

which allows independent tuning of each mode's bandwidth and damping ratio.

It is important to note that the measured distance values must be transformed from the sensor coordinate system to the rotor COG system (see Equation 2.44). Conversely, the bearing forces are calculated by the controller in the COG system and must be transformed to the bearing coordinate system (see Equation 2.40).

To be precise, this still does not achieve complete decoupling for asymmetrical magnetic bearing systems[46]. Without going into the details, the reader should note that an additional decoupling matrix must be included in the control law to achieve complete decoupling of both modes [1].

---

[45] Negative stiffness sets a lower limit on the proportional component of the controller and thus on the bandwidth of the closed loop. However, the disadvantage of a high control bandwidth is greater amplification of noise and the need for a higher sampling rate in digital control loops [18].

[46] In this context, symmetry refers to the parameters k_{I} and k_{x} of AMBs 1 and 2 and the distances between the magnetic bearings and the rotor COG. For further details, the reader is referred to [1]

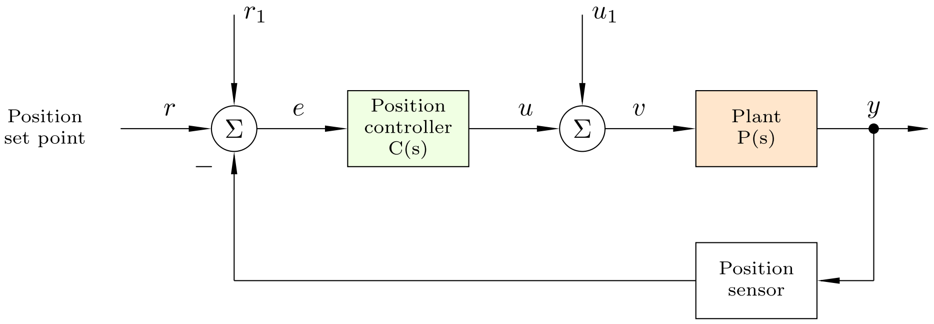

Figure 3.29: Schematic representation of the position control loop. The position controller $\mathbf{C}(s)$ is implemented in a DSP. The plant $\mathbf{P}(s)$ comprises the amplifiers, the magnetic bearings and the rotor shaft.

symbol	value	units
rotor weight m	3.452	kg
moment of inertia $\Theta_x = \Theta_y$	$40952 \cdot 10^{-6}$	$\mathrm{kg\,m^2}$
moment of inertia Θ_z	$880 \cdot 10^{-6}$	$\mathrm{kg\,m^2}$
bearing distance a	$108 \cdot 10^{-3}$	m
bearing distance b	$96 \cdot 10^{-3}$	m
sensor distance c	$154 \cdot 10^{-3}$	m
sensor distance d	$137 \cdot 10^{-3}$	m
force-current factor $k_{I,1} = k_{I,2}$	5.8	$\mathrm{N\,A^{-1}}$
force-displ. factor $k_{x,1} = k_{x,2}$	-32000	$\mathrm{N\,m^{-1}}$
bias current I_0	3	A
prop. gain P_{trans}	231000	$\mathrm{A\,m^{-1}}$
prop. gain P_{tilt}	2411	$\mathrm{A\,m^{-1}}$
deriv. gain D_{trans}	2143	$\mathrm{A\,s\,m^{-1}}$
deriv. gain D_{tilt}	24	$\mathrm{A\,s\,m^{-1}}$
int. gain I_{trans}	2000000	$\mathrm{A\,m^{-1}\,s^{-1}}$
int. gain I_{tilt}	20000	$\mathrm{A\,m^{-1}\,s^{-1}}$

Table 3.6: Test stand and position controller parameter set, used for the concluding measurements.

4 Measurements

The research group has already implemented MATLAB® software routines for the communication with the DSP and execution of various measurements. Using these pre-designed scripts is essential and greatly reduces the workload. Numerous measurements were carried out to facilitate the startup of the individual test stand components and optimize the position controller while the rotor was levitating. In the final chapter of this thesis, the results of selected measurements are presented. These are intended to demonstrate the robustness of the implemented position control system (output sensitivity and Campbell diagram) and to analyze the usability of the test stand itself (waterfall diagrams and eccentricity).
Figure 4.1 shows a photograph of the test stand designed as part of this thesis. The black cables are position sensor cables and the blue cables in the background are the power cables for the AMBs. The green printed circuit boards on the front surfaces of the stators connect the coils accordingly.

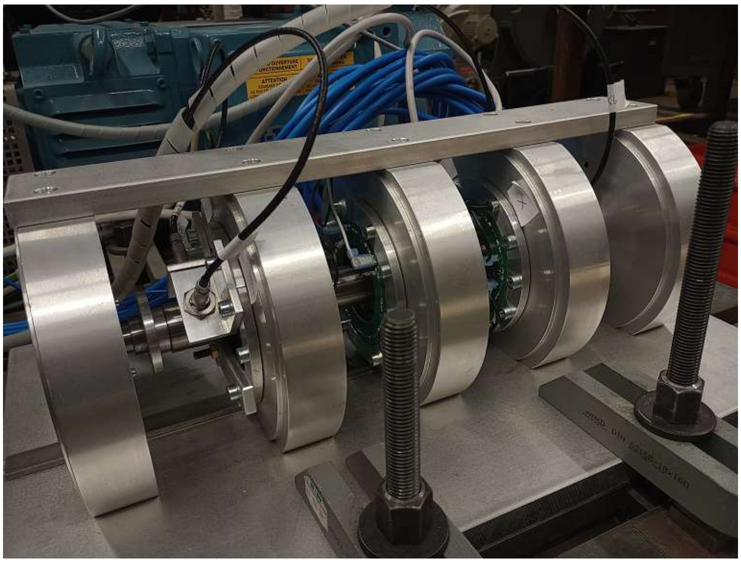

Figure 4.1: This is a photograph of the test stand designed as part of this thesis. To prevent vibrations, it was bolted to a machine bed in the machine hall of the Institute of Energy Systems and Electric Drives at TU Wien.

4.1 Output Sensitivity

In an AMB system, the output sensitivity matrix plays a key role in determining how effectively the system rejects external disturbances (unbalance forces, shaft-housing interactions, aerodynamic loads) and how well it can tolerate uncertainties (rotor mass or stiffness variations, changes in magnetic circuit parameters). In contrast to a single input single output (SISO) loop, most AMB applications are multiple input multiple output (MIMO) systems. This work uses radial active magnetic bearings, each of which consists of two orthogonally arranged radial actuators. The system has a total of four inputs (the forces of the magnetic bearings) and four outputs (the generalized coordinates, i.e. the rotor shaft position in the COG coordinate system). Therefore, the use of transfer function matrices is required.

The output sensitivity matrix $\mathbf{S}_{\mathrm{O}}(s)$ for the electromechanical system of this thesis (see Figure 3.29), is defined as the 4×4 transfer function matrix[1]

$$\mathbf{S}_{\mathrm{O}}(s) = [\mathbf{I} + \mathbf{P}(s)\mathbf{C}(s)]^{-1}. \tag{4.1}$$

Its elements represent the gains from disturbance inputs to measured outputs, both of which are in generalized coordinates. Hence, the output sensitivity matrix $\mathbf{S}_{\mathrm{O}}(j\omega)$ directly indicates for each frequency, the extent to which an external disturbance (on the rotor shaft position) is amplified or attenuated by the closed-loop system. For a robust MIMO control design, the approach would be to limit the peak singular value of $\mathbf{S}_{\mathrm{O}}(j\omega)$, a strategy that would ensure both disturbance rejection and robust margins. To calculate the singular values of the matrix $\mathbf{S}_{\mathrm{O}}(j\omega)$ for a real system, all of its entries $S_{\mathrm{O,kl}}(j\omega)$ have to be measured over the entire frequency range of interest. Since this would require a lot of measurements, the corresponding International Organization for Standardization (ISO) has introduced a standard [19], which significantly simplifies this process. According to this standard, a certain class of AMB systems achieves sufficient disturbance rejection and robust margins if the values of the output sensitivity matrix's main diagonal elements remain below the threshold of 3. In this thesis these elements are denoted as S_{xx}, S_{yy}, $S_{\alpha\alpha}$ and $S_{\beta\beta}$. To determine the robustness of the implemented PD position control, these elements are measured for different directions (translation x, y and rotation α, β), rotor speeds Ω and variations of the controller gain.

In Figure 4.2, the magnitude of the elements $S_{xx}(j\omega)$ and $S_{\alpha\alpha}(j\omega)$ is plotted as a function of frequency for the translational and rotational modes at rotor speed $\Omega = 0$. The graphs remain well below the threshold of 3 over the entire frequency range of interest. For the chosen control parameters, the values of the rotational mode are slightly higher than those of the translational mode in the lower frequency range. But conversely, their peak value in the upper frequency range is lower. Accordingly, the focus of further analysis will be limited to the translation mode, the element $S_{xx}(j\omega)$, because its peak value is the highest of all.

Despite the ISO standard's restriction to the main diagonal elements of $\mathbf{S}_{\mathrm{O}}(j\omega)$, it should be noted that the secondary diagonal elements may still be of interest. This is especially true for the elements describing cross-coupling between the two rotational degrees of freedom, $S_{\alpha\beta}(j\omega)$. These degrees of freedom are coupled with each other via the gyroscopic effect. Since this effect is small for the elongated rotor shaft designed in this thesis, the cross-coupling is correspondingly low. Nevertheless, to validate this statement

---

[1] $\mathbf{I}$ represents the unity matrix in this context.

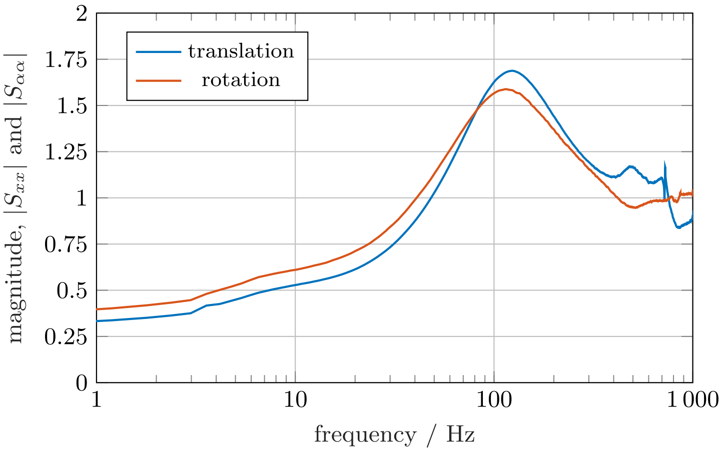

Figure 4.2: Measurement of the two diagonal elements $|S_{xx}(j\omega)|$ and $|S_{\alpha\alpha}(j\omega)|$ (translational and rotational DOF), performed at rotor standstill ($\Omega = 0$).

for this particular rotor shaft, the secondary diagonal elements, $S_{xy}(j\omega)$ and $S_{\alpha\beta}(j\omega)$, were also measured. A comparison with the corresponding main diagonal elements showed that these secondary diagonal elements do not have a significant influence.

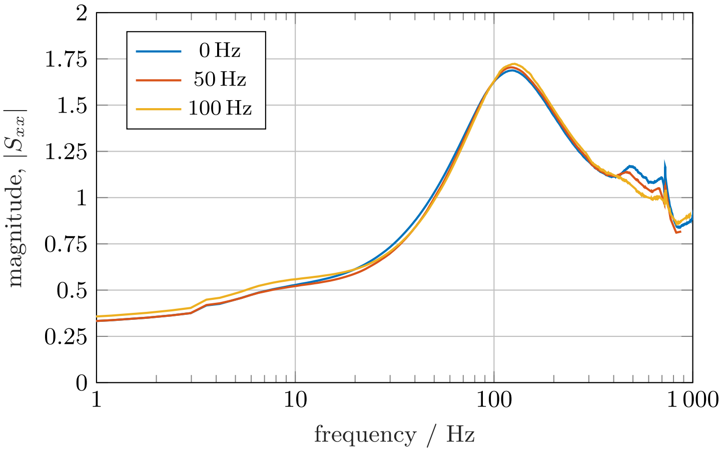

Figure 4.3: Measurement of the diagonal element $S_{xx}(j\omega)$ for the translational DOF for different rotor speeds Ω (0 Hz, 50 Hz, 100 Hz).

To investigate how rotor speed influences sensitivity, the element $S_{xx}(j\omega)$ is measured at different rotor speeds Ω. Figure 4.3 shows the $S_{xx}(j\omega)$ curve as a function of frequency for different rotor speeds, emphasizing that the influence is negligible for the translational DOF. The measurement is performed for $S_{\alpha\alpha}(j\omega)$ to confirm that its peak value is smaller.

Parameter uncertainties and variations have the potential to occur at a number of points within the control loop. Sensors and amplifiers may have some uncertainty in their gain, and the force-current and force-displacement factors of the AMBs show a dependence on the operating point, which has been discussed in more detail in Section 3.2.4. To account for all of these influences, Figure 4.4 shows how the values of $S_{xx}(j\omega)$ are related to varying controller gain (deviation of $\pm 20\,\%$ from the nominal gain value). It can be observed that a higher controller gain ($120\,\%$ of the nominal value) improves the suppression of disturbances in the lower frequency range, but at the cost of the ability to suppress disturbances at frequen-

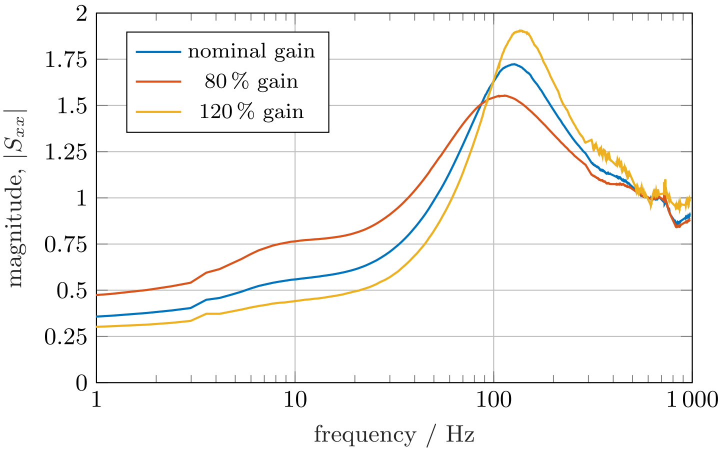

Figure 4.4: Measurement of the diagonal element $S_{xx}(j\omega)$ for the translational DOF at rotor speed $\Omega = 100\,\mathrm{Hz}$. To illustrate the influence of parameter variations, the controller gain is varied (nominal, 80 %, 120 %).

cies around 100 Hz. Therefore, a careful trade-off must be made when designing controllers for magnetic bearings, especially under conditions where the parameters are subject to uncertainty and variation.

4.2 Campbell Diagram

The magnetically levitated rigid rotor can be thought of as a simple mass-spring-damper system whose modes of motion are basically translational and rotational[2]. The undamped natural frequencies and the damping factor of these modes are determined by the corresponding eigenvalues of the system's dynamic matrix. The closed-loop system in Figure 3.29 is a MIMO system with a 8×8 dynamics matrix, hence with eight eigenvalues, denoted $\lambda_1 ... \lambda_8$. A Campbell diagram is the primary tool in rotor dynamics to visualize how these eigenvalues vary with rotor speed Ω and to identify where dynamic instabilities or resonances will occur. It provides a clear representation of the interaction between rotor modes and excitation harmonics, facilitates the identification of critical speeds, and serves as a basic framework for designing new machines and diagnosing vibration problems in the field.

To obtain the Campbell diagram of the actively magnetically levitated rotor shaft, a complete mathematical model must first be developed, which includes all components of the control loop (see Figure 3.29). The electromechanical model, shown in Equation 2.42, comprises the rotor shaft and the AMBs. Table 3.4 contains the electrical model of the magnetic bearings, and Equation 3.14 shows the current controller transfer function. The position- and current sensors, as well as the magnetic bearing amplifiers are essentially regarded as having constant gain and no dynamics. The position controller transfer function is derived in Section 3.5.3.

Figure 3.29 illustrates how these transfer functions are combined to a closed-loop system. The resulting state-space model includes all the components needed to mathematically describe the motion of the rigid rotor shaft, suspended by the active magnetic bearings. This state-space model's dynamic matrix

---

[2] To be precise, the decoupling of translational and rotational modes only applies when they are actually decoupled. However, this is not entirely the case with this test stand. In Section 2.5.2 it is explained why movement in the axial direction does not need to be taken into consideration in this thesis.

determines the dynamics of the rigid rotor's motion. The eigenvalues of the matrix can be calculated as a function of the rotor speed Ω, to yield the values for the Campbell diagram (see Figure 4.5). The parameter set of the plant and the position controller is listed in Table 3.6.

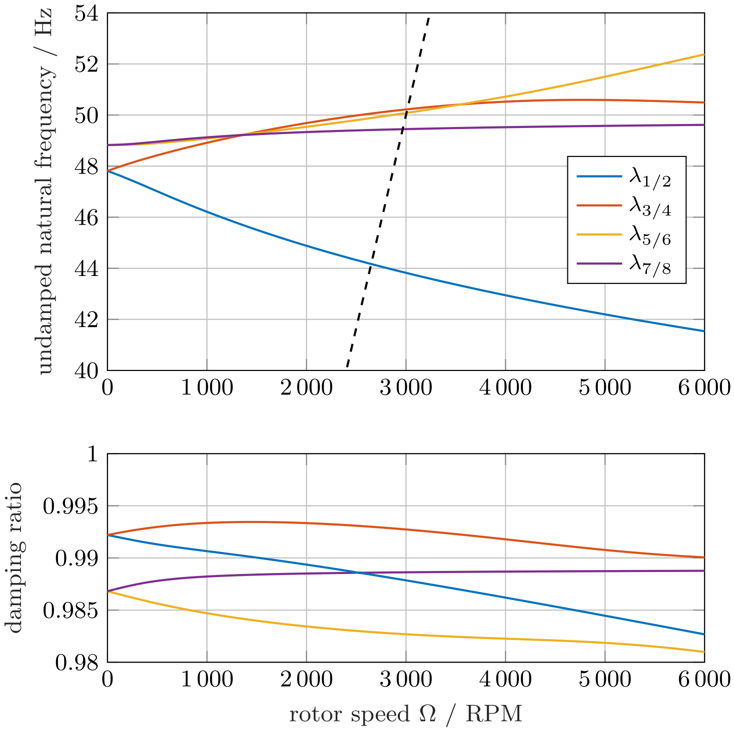

Figure 4.5: Simulation of the Campbell diagram (rigid body closed-loop eigenfrequencies as a function of rotor speed - top, corresponding damping ratio of the eigenvalues - bottom) for decoupled PD control of translational and rotational modes.

The eight eigenvalues of the dynamic matrix come in four conjugate complex pairs, i.e. $\lambda_1 = \bar{\lambda}_2$, $\lambda_3 = \bar{\lambda}_4$, $\lambda_5 = \bar{\lambda}_6$, $\lambda_7 = \bar{\lambda}_8$. The undamped natural frequency of an eigenvalue is calculated from its magnitude, $\omega_0 = |\lambda|$, and the damping ratio by $\zeta = -\mathfrak{Re}(\lambda)/|\lambda|$. Hence, the eight eigenvalues result in a total of four different curves in the Campbell diagram.

The four coloured curves in the upper diagram in Figure 4.5 represent the rotor's rigid body natural frequencies, otherwise referred to as mode lines. The eigenvalue damping ratio as a function of rotor speed Ω is shown in the graphs below.

Because of the coupling via the gyroscopic effect and the asymmetrical design of the test stand, the undamped natural frequencies of all the eigenvalues depend on the rotor speed. In this context, asymmetry refers to the distances between the magnetic bearings and the rotor COG and/or the parameters k_I and k_x of AMBs 1 and 2. During the design validation of the AMBs, in particular the measurement of the force-current and force-displacment factors, it could be shown, that the corresponding factors are all equal. For further details, the reader is referred to [1]. The natural frequencies of the two eigenvalues, $\lambda_{3/4}$ and $\lambda_{7/8}$, appear to asymptotically approach a constant final value. However, the natural frequencies of the eigenvalues $\lambda_{1/2}$ and $\lambda_{5/6}$ split as the rotor speed Ω increases, which can cause problems with certain position controller architectures. This is further explained in [18] and [1].

The intersection points of the mode lines with the black dashed line in the above illustration correspond to theoretical critical rotor speed frequencies. However, in this context, the decisive value is the damped natural frequency of the eigenvalues (see Equation 4.2). When the rotor is operated at these speeds, significant vibrations can occur due to synchronous excitation (rotor speed frequency is equal to the damped natural frequency of the eigenvalue) caused by unbalance forces.

4.3 Waterfall plots of Position and Bearing Current

Waterfall plots constitute a further highly efficacious tool for analysis in the domain of rotors and rotating machinery. There, the frequency spectrum of the measured variable is displayed as a function of the rotor speed. The purpose of this illustration is to provide a visual representation of the changes in, for example, the rotor orbit[3] and the magnetic bearing current as the rotor speed is varied.

But for the sake of a clearer illustration, in this work only the values corresponding to the single, double and triple harmonics of the rotor speed Ω are taken. In Figure 4.6, this partial waterfall plot presents the amplitude of the rotor orbit as a function of different rotor speeds. It appears that a rigid body mode is being excited in the lower frequency range at around 8 Hz to 10 Hz. The Campbell diagram can be used to check for this resonance. In Figure 4.5, the dashed line intersects the mode lines at a rotor speed of $\Omega \approx 45\,\mathrm{Hz}$ to 50 Hz, and this would cause the undamped rotor shaft to vibrate at this frequency. However, due to damping, it is necessary to distinguish between the natural frequency ω_0 and the damped natural frequency $\omega_{\mathrm{d,n}}$. The following relationship connects these two frequencies

$$\omega_{\mathrm{d,n}} = \omega_0 \sqrt{1-\zeta^2} \tag{4.2}$$

with the damping ratio ζ of the corresponding eigenvalue. Hence, the damped natural frequency decreases below the natural frequency with increasing damping, until it becomes zero at $\zeta = 1$ [3]. Inserting the values obtained from the Campbell diagram into (4.2) yields the following for the damped natural frequency

$$\omega_{\mathrm{d,n}} = 2\pi\, 50\,\mathrm{rad\,s^{-1}} \sqrt{1-0.987^2} = 2\pi\, 8\,\mathrm{rad\,s^{-1}} \tag{4.3}$$

and this supports the assumption that a rigid body mode is excited at a frequency of approximately 8 Hz.

As the rotor speed increases, the amplitude of the orbit decreases and remains constant up to rotor speeds of $\Omega = 100\,\mathrm{Hz} = 6000\,\mathrm{RPM}$. The constant orbit is likely caused by an eccentricity between the AMB rotor package (rotor lamination stack) and the rotor shaft. Possible displacements due to unbalance forces are undetectable because they are completely masked by the eccentricity.

The current in the magnetic bearings shows a completely different pattern, as shown in Figure 4.7. All three rotor frequency harmonics of the bearing current increase with speed. It appears that the controller has to exert an increasing amount of effort to keep the rotor on its rather constant orbit.

With increasing rotor speeds, unbalance compensation measures may be needed in the controller, as the required current might exceed the maximum permissible limits of the amplifier. For example, a current-nulling method can be used, which causes a reduction in the required current [20].

---

[3] For a magnetic bearing supported rotor, the orbit is simply the path that the centerline of the rotor takes in the transverse plane of the bearing as it rotates.

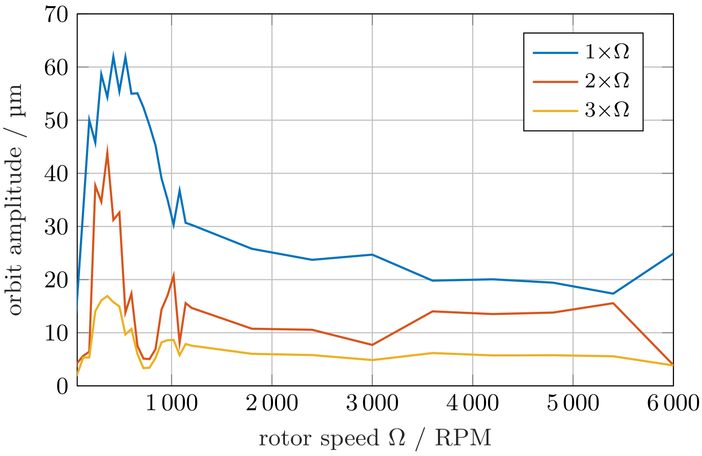

Figure 4.6: The plots show the first three rotor frequency harmonics of the orbit amplitude as a function of rotor speed Ω. A rigid body mode is excited at $\omega_{\mathrm{d,n}} = 2\pi\, 8\,\mathrm{rad\,s^{-1}}$.

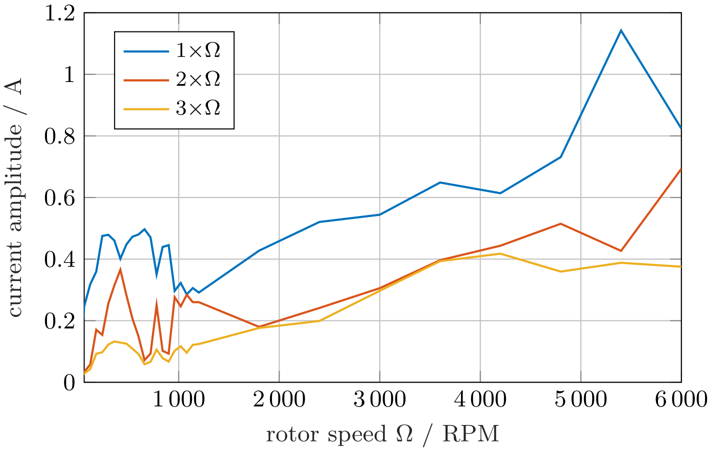

Figure 4.7: The graphs show the first three harmonics of the bearing current with respect to the rotor speed Ω. With increasing rotor speed, the harmonic components of the magnetic bearing currents increase as well.

4.4 Eccentricity

This measurement aims to verify the presence of any eccentricity between the AMB rotor package and the rotor shaft. To determine the eccentricity, the rotor is rotated at a slow speed by the drive unit, $\Omega \approx 0.2\,\mathrm{Hz}$. This is to ensure that the position controller is able to keep the rotor exactly at the desired reference position in the center. The magnetic bearing currents and the rotor angle are then recorded simultaneously.

The results are plotted in Figure 4.8, and it is immediately apparent that the magnetic bearing current curve appears to be off-center when compared to its mean value, indicating the presence of eccentricity.

The results of the force-displacement factor determination can now be used to calculate the factor by which a change in current can be converted into a change in air gap length or position. Due to the geometric conditions inherent in the electromagnetic actuator configuration, the eccentricity exhibited in a magnetic bearing manifests itself in its two actuators with a spatial offset of 90°. Therefore, for cross-validation

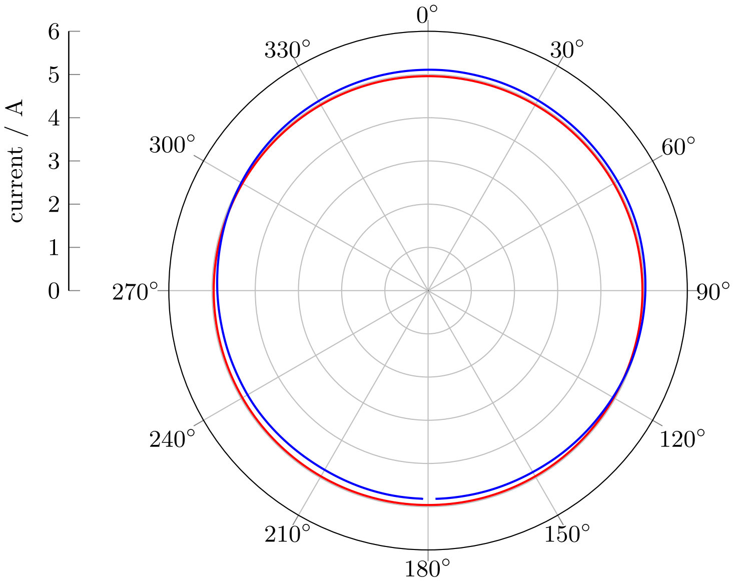

Figure 4.8: Magnetic bearing current (in blue) compared to its mean value (in red) during a complete rotation of the rotor shaft. The angle in the polar plot is the rotor shaft angle γ.

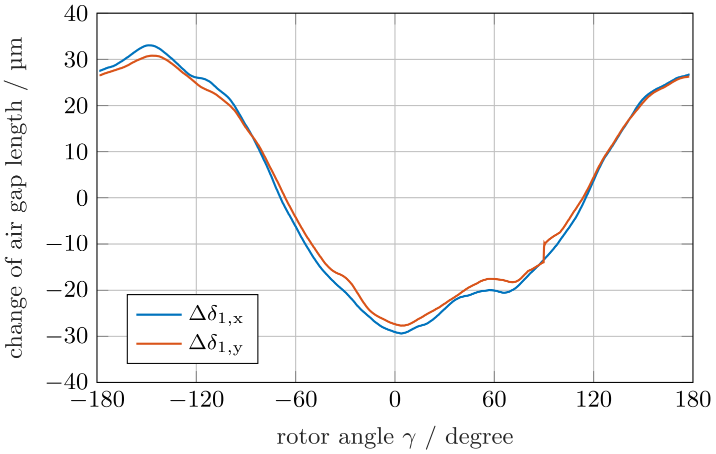

Figure 4.9: The graphs show the change in the air gap length detected by the two actuators (x- and y-axes) as a function of rotor angle. This change can be attributed to the eccentricity between the AMB rotor package (rotor lamination stack) and the rotor shaft axis. The data from the y-axis are shifted by 90° to facilitate comparison.

purposes, the evaluation is performed for both the x- and y-axes.

The results, which show the change in air gap length as a function of rotor angle γ, are shown in Figure 4.9. To facilitate comparison of the findings from both axes, the data from the y-axis are shifted by 90°. The results for the two axes show substantial congruence, supporting the eccentricity hypothesis. They are also consistent with the data presented in the waterfall plot of the rotor orbit.

Evaluation of the measurement results indicates the need for cylindrical grinding. It would be a very promising finishing technique with regard to the concentricity of the individual rotor shaft sections in relation to each other and it is a process that can still be performed.

5 Conclusion and Outlook

5.1 Conclusion

Active magnetic bearings are a class of non-contact rotor bearings in which electromagnetic forces - generated by actively controlled stator coils - suspend and center a rotor shaft entirely without the need for physical contact. This makes this bearing technology particularly suitable for use in high-speed machines such as turbo compressors, flywheel energy storage systems and turbomolecular pumps. Operating these machines can be challenging and requires the implementation of advanced control algorithms.

This thesis presents the design, realisation and experimental validation of a test stand for an active magnetic bearing system, which will serve as a foundation for future research on rotor dynamics and advanced control algorithms.

A modular layout was aimed for. Thereby the test stand is adaptable to the various requirements of these scientific investigations. The major challenge is to design the individual mechanical components and aligning them posed a major challenge. The engineering of the active magnetic bearings was based on the fundamentals of the double reluctance actuator, and validation measurements accompanied the process. This ensured that the requirements are met and guarantees largely linear operation of the actuators. The rotor shaft design is free of position sensor target discs, an approach taken to circumvent the occurrence of additional eccentricities. So the commercial eddy current position sensors are used under unspecified operating conditions and exhibiting non-linear characteristics. However, measurements showed that the sensors have nearly linear characteristics within the operating area defined by the mechanical air gap in the auxiliary bearings. Simple linear control structures could be used since both the position sensors and the active magnetic bearings behave largely linearly. In particular, a decentralized PD controller was implemented. Designing a model-based controller required knowledge of the mathematical models of both the active magnetic bearing and the rotor. The magnetic bearing model results from the electromagnetic fundamentals and the validation measurements. Specifically, the force-current and force-displacement factors are used for the description. The rotor shaft's mathematical model was created based on the principles of rigid rotor dynamics. Finally, numerous measurements were performed with the levitating rotor shaft to validate the entire system.

In conclusion, the successful and robust control of an exemplary rotor shaft on this test stand with a simple linear controller structure was demonstrated. This was shown by measuring the output sensitivity of the closed-loop system. During the magnetic bearings' validation process, the force-current and force-displacement factors were measured in both directions of actuation. Because the factors agree well, it can be assumed that static eccentricity is negligible. Hence a satisfactory radial alignment was achieved through careful consideration and sequencing of all necessary mechanical manufacturing steps.

However, eccentricities of the various rotor sections could not be completely avoided. To make the test stand utilizeable for some specific further studies, these eccentricities must be minimized through cylindrical grinding.

5.2 Outlook

The final validation measurements for eccentricity indicate that, despite the careful design and manufacture of the rotor shaft, eccentricity could not be fully prevented. This eccentricity must be minimized as much as possible through circular grinding because it hinders further scientific studies. For example, unbalance detection requires that the relevant rotor shaft sections be as concentric as possible with respect to each other.

Each active magnetic bearing uses eight of the 12 available stator coils for its two actuators. The remaining four coils are arranged so that it is conceivable to take a differential measurement of the radial rotor position. However, the practicality of this approach still needs to be investigated.

Given the current configuration of the test stand and the rotor shaft design, the self-stabilizing effect of the active magnetic bearings in the axial direction is sufficient. However, it was observed that the drive motor caused destabilization in the axial direction when the torques were too high. To counteract this, an active magnetic thrust bearing can be added to the test stand.

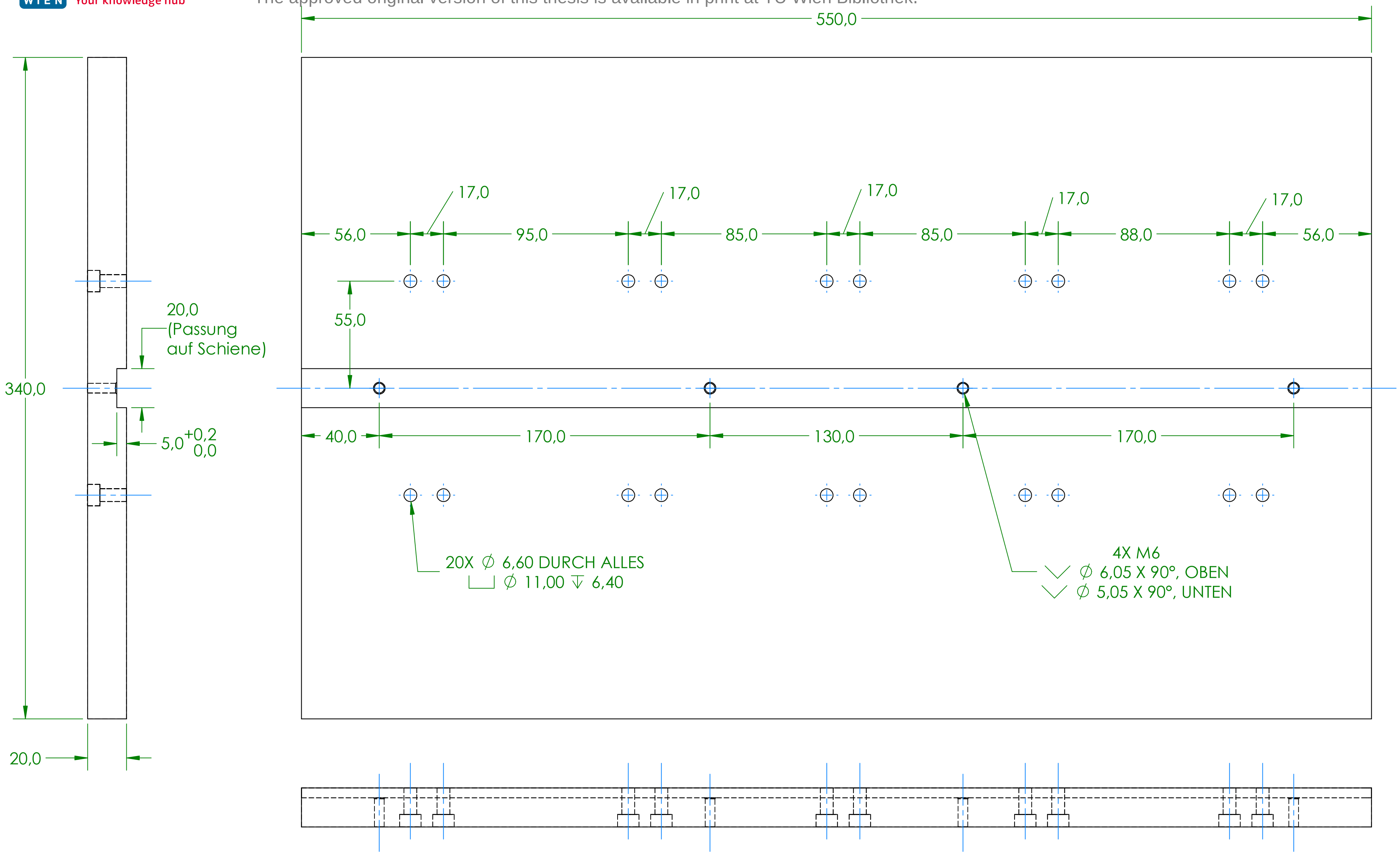

WENN NICHT ANDERS DEFINIERT:
BEMASSUNGEN SIND IN MILLIMETER
OBERFLÄCHENBESCHAFFENHEIT:
TOLERANZEN:
LINEAR: +/-0.1mm
WINKEL: +/-0.5°

OBERFLÄCHENGÜTE:

ENTGRATEN
UND SCHARFE
KANTEN
BRECHEN

ZEICHNUNG NICHT SKALIEREN

ÄNDERUNG

	NAME	SIGNATUR	DATUM
GEZEICHNET	MSO		
GEPRÜFT			
GENEHMIGT			
PRODUKTION			
QUALITÄT			

BENENNUNG:

WERKSTOFF:
Aluminium Blech/Platte
AlMg4,5Mn, EN AW-5083

ZEICHNUNGSNR.
Bodenplatte

A3

GEWICHT: 3643g

MASSSTAB:1:2

BLATT 1 VON 1

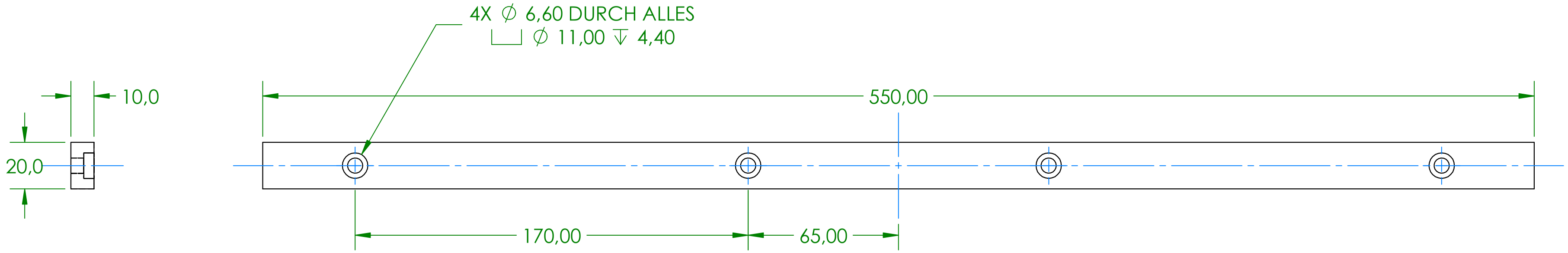

WENN NICHT ANDERS DEFINIERT: BEMASSUNGEN SIND IN MILLIMETER OBERFLÄCHENBESCHAFFENHEIT: TOLERANZEN: LINEAR: +/-0.1mm WINKEL: +/-0.5°	OBERFLÄCHENGÜTE:	ENTGRATEN UND SCHARFE KANTEN BRECHEN	ZEICHNUNG NICHT SKALIEREN	ÄNDERUNG
	NAME	SIGNATUR	DATUM	BENENNUNG:
GEZEICHNET	MSO			
GEPRÜFT				
GENEHMIGT				
PRODUKTION				
QUALITÄT			WERKSTOFF: Aluminium AlMgSi0.5 Winkelprofil, gepresst F22, EN AW-6060	ZEICHNUNGSNR. Führungsschiene
			GEWICHT: 290g	MASSSTAB:1:2
				BLATT 1 VON 1
				A3

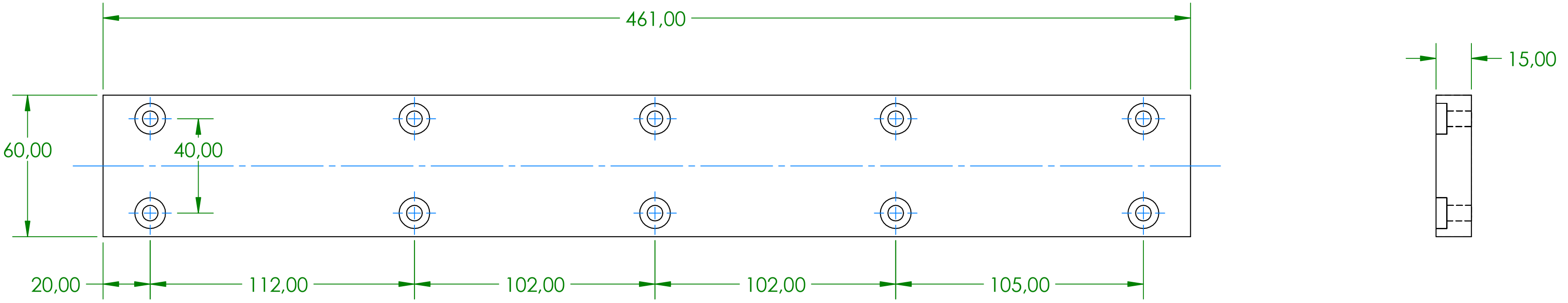

WENN NICHT ANDERS DEFINIERT:
BEMASSUNGEN SIND IN MILLIMETER
OBERFLÄCHENBESCHAFFENHEIT:
TOLERANZEN:
LINEAR: +/-0.1mm
WINKEL: +/-0.5°

OBERFLÄCHENGÜTE:

ENTGRATEN
UND SCHARFE
KANTEN
BRECHEN

ZEICHNUNG NICHT SKALIEREN

ÄNDERUNG

	NAME	SIGNATUR	DATUM
GEZEICHNET	MSO		
GEPRÜFT			
GENEHMIGT			
PRODUKTION			
QUALITÄT			

BENENNUNG:

WERKSTOFF:
AlMgSi0.5 Stab rechteckig,
gepresst T66, EN AW-6060

ZEICHNUNGSNR.
Verstrebung

A3

GEWICHT: 1094g

MASSSTAB:1:2

BLATT 1 VON 1

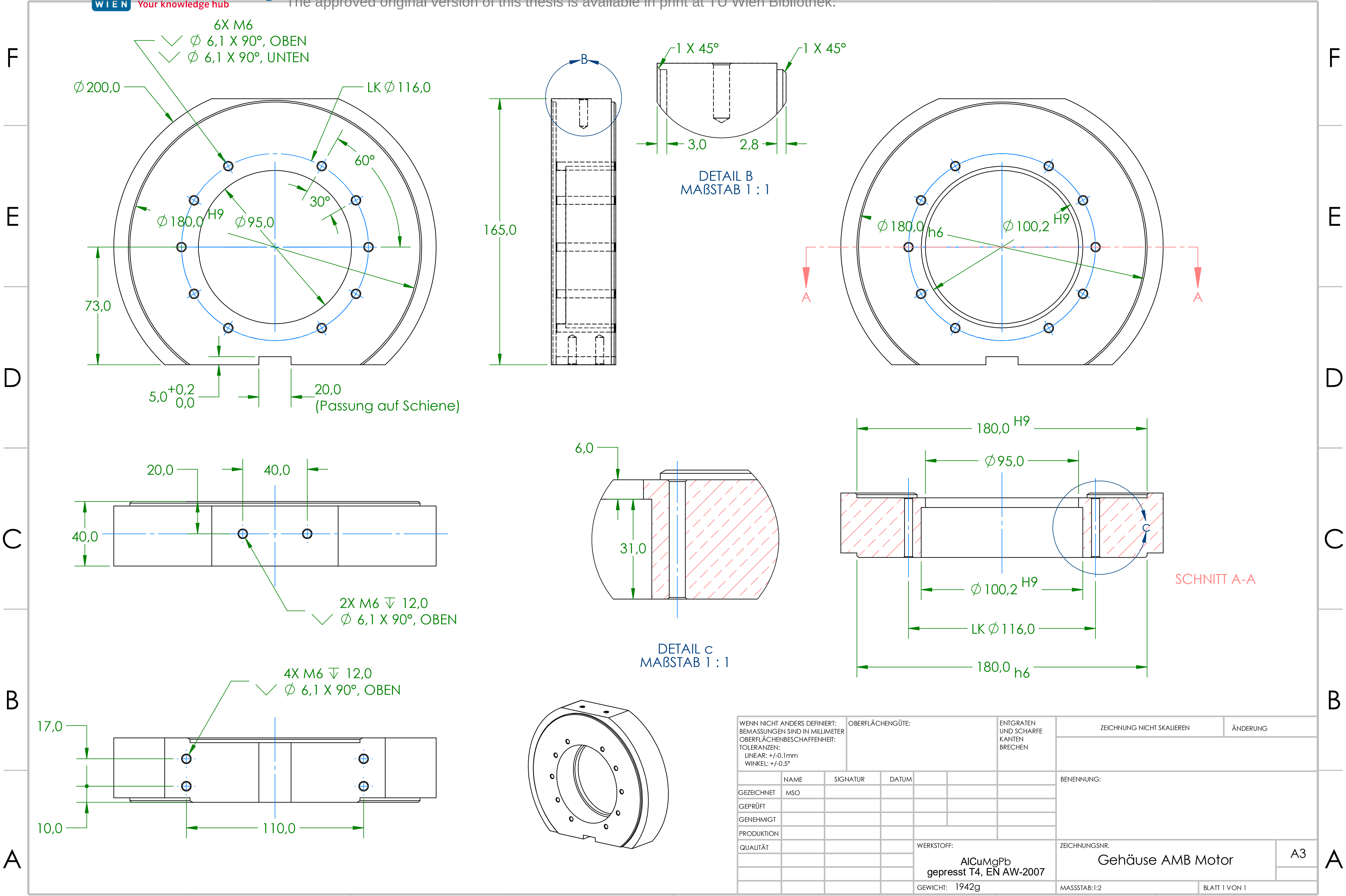

WENN NICHT ANDERS DEFINIERT:
BEMASSUNGEN SIND IN MILLIMETER
OBERFLÄCHENBESCHAFFENHEIT:
TOLERANZEN:
LINEAR: +/-0.1mm
WINKEL: +/-0.5°

OBERFLÄCHENGÜTE:

ENTGRATEN UND SCHARFE KANTEN BRECHEN

ZEICHNUNG NICHT SKALIEREN

ÄNDERUNG

	NAME	SIGNATUR	DATUM
GEZEICHNET	MSO		
GEPRÜFT			
GENEHMIGT			
PRODUKTION			
QUALITÄT			

BENENNUNG:

WERKSTOFF: AlCuMgPb gepresst T4, EN AW-2007

ZEICHNUNGSNR. Gehäuse AMB Motor

A3

GEWICHT: 1942g

MASSSTAB:1:2

BLATT 1 VON 1

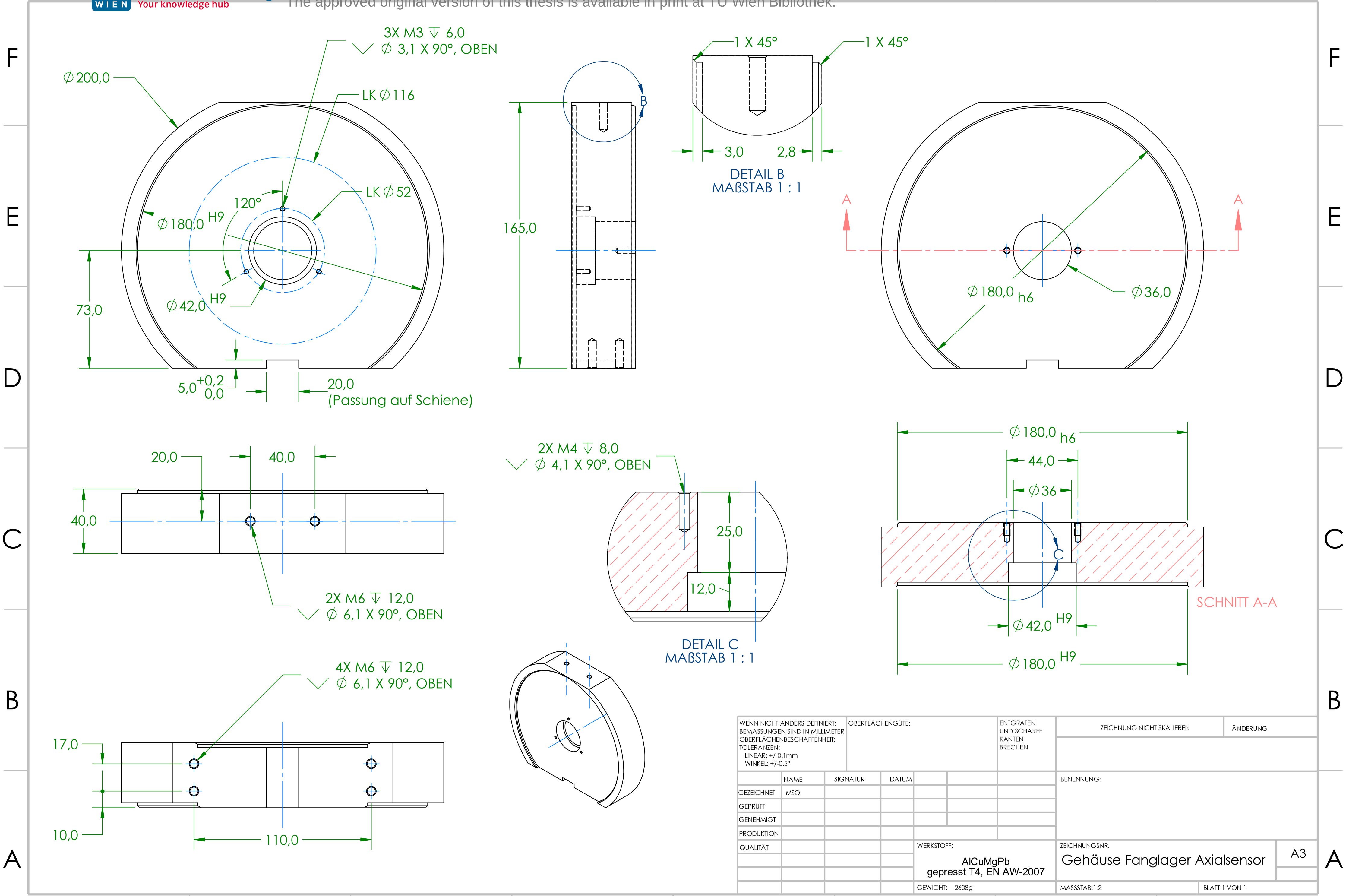

WENN NICHT ANDERS DEFINIERT: BEMASSUNGEN SIND IN MILLIMETER OBERFLÄCHENBESCHAFFENHEIT: TOLERANZEN: LINEAR: +/-0.1mm WINKEL: +/-0.5°	OBERFLÄCHENGÜTE:	ENTGRATEN UND SCHARFE KANTEN BRECHEN	ZEICHNUNG NICHT SKALIEREN	ÄNDERUNG

	NAME	SIGNATUR	DATUM
GEZEICHNET	MSO		
GEPRÜFT			
GENEHMIGT			
PRODUKTION			
QUALITÄT			

BENENNUNG:

WERKSTOFF:
AlCuMgPb
gepresst T4, EN AW-2007

ZEICHNUNGSNR.
Gehäuse Fanglager Axialsensor

A3

GEWICHT: 2608g

MASSSTAB:1:2

BLATT 1 VON 1

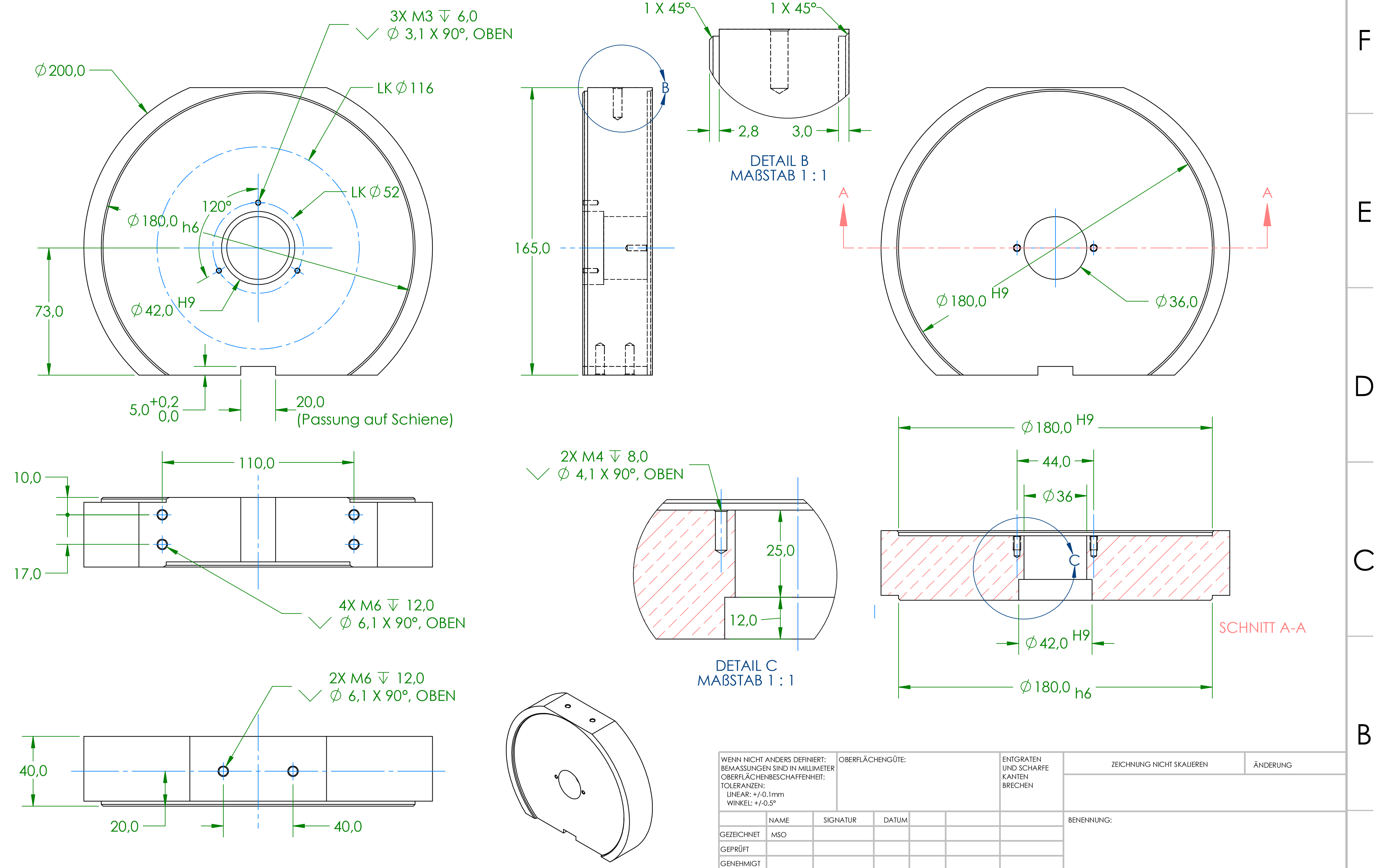

WENN NICHT ANDERS DEFINIERT: BEMASSUNGEN SIND IN MILLIMETER OBERFLÄCHENBESCHAFFENHEIT: TOLERANZEN: LINEAR: +/-0.1mm WINKEL: +/-0.5°		OBERFLÄCHENGÜTE:		ENTGRATEN UND SCHARFE KANTEN BRECHEN	ZEICHNUNG NICHT SKALIEREN	ÄNDERUNG
	NAME	SIGNATUR	DATUM		BENENNUNG:	
GEZEICHNET	MSO					
GEPRÜFT						
GENEHMIGT						
PRODUKTION						
QUALITÄT				WERKSTOFF: AlCuMgPb gepresst T4, EN AW-2007	ZEICHNUNGSNR. Gehäuse Fanglager Drehgeber	A3
				GEWICHT: 2608g	MASSSTAB:1:2	BLATT 1 VON 1

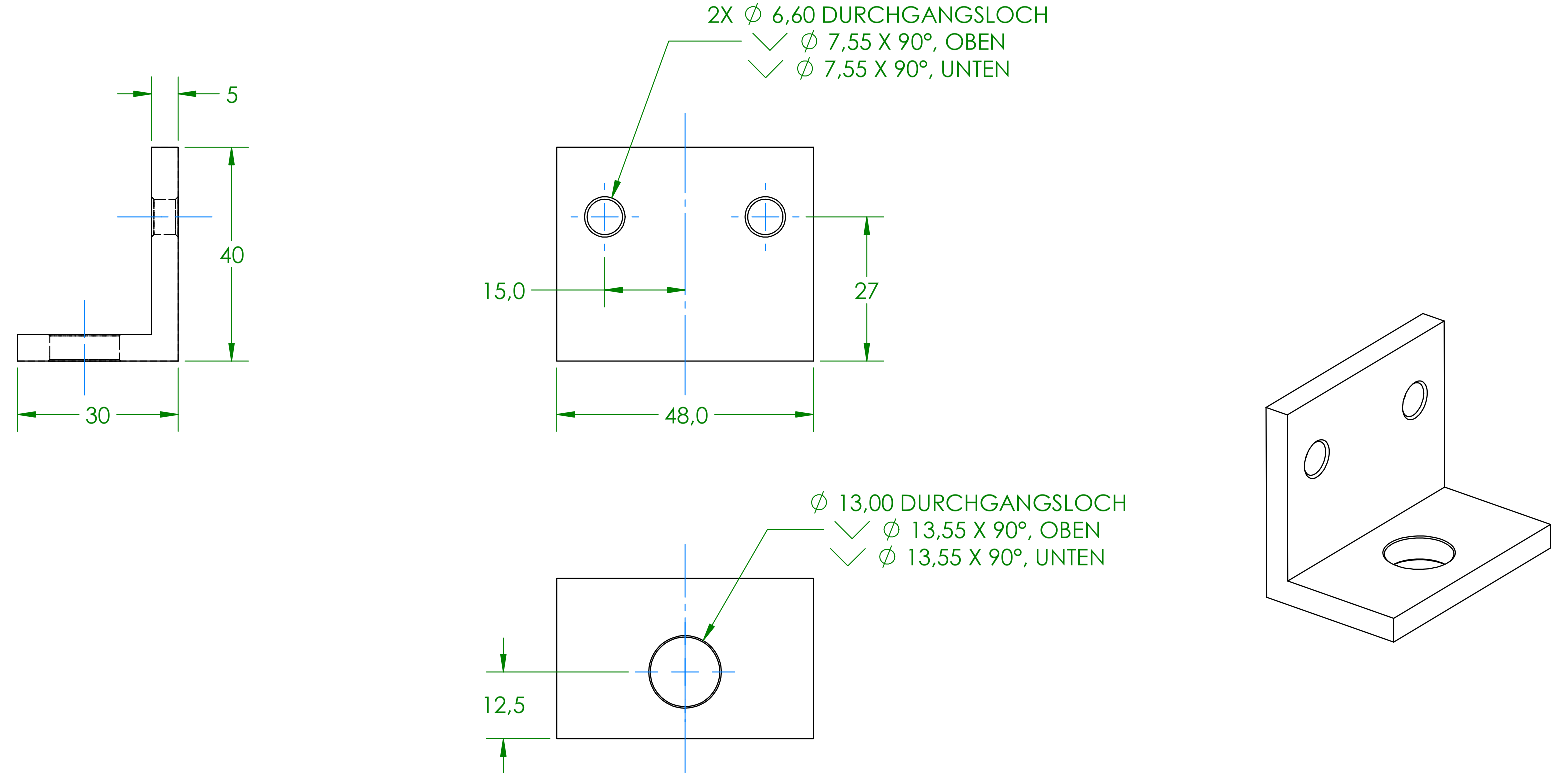

WENN NICHT ANDERS DEFINIERT:
BEMASSUNGEN SIND IN MILLIMETER
OBERFLÄCHENBESCHAFFENHEIT:
TOLERANZEN:
LINEAR: +/-0.1mm
WINKEL: +/-0.5°

OBERFLÄCHENGÜTE:

ENTGRATEN UND SCHARFE KANTEN BRECHEN

ZEICHNUNG NICHT SKALIEREN

ÄNDERUNG

	NAME	SIGNATUR	DATUM
GEZEICHNET	MSO		
GEPRÜFT			
GENEHMIGT			
PRODUKTION			
QUALITÄT			

BENENNUNG:

WERKSTOFF:
Aluminium AlMgSi0.5 Winkelprofil, gepresst F22, EN AW-6060

ZEICHNUNGSNR.
Sensorhalter

A3

GEWICHT: 39g

MASSSTAB:1:1

BLATT 1 VON 1

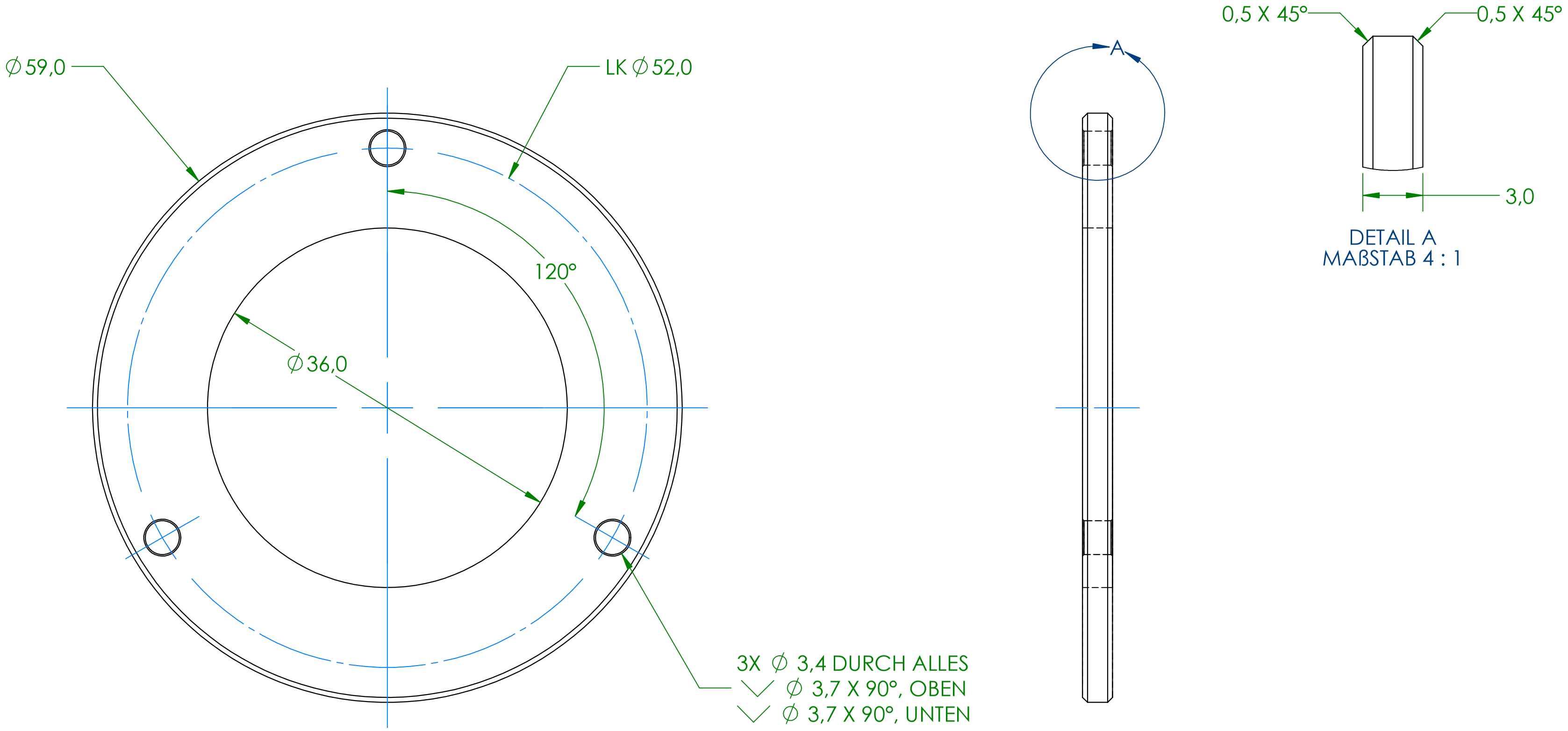

WENN NICHT ANDERS DEFINIERT: BEMASSUNGEN SIND IN MILLIMETER OBERFLÄCHENBESCHAFFENHEIT: TOLERANZEN: LINEAR: +/-0.1mm WINKEL: +/-0.5°	OBERFLÄCHENGÜTE:	ENTGRATEN UND SCHARFE KANTEN BRECHEN	ZEICHNUNG NICHT SKALIEREN / ÄNDERUNG

	NAME	SIGNATUR	DATUM
GEZEICHNET	MSO		
GEPRÜFT			
GENEHMIGT			
PRODUKTION			
QUALITÄT			

BENENNUNG:

WERKSTOFF: AlCuMgPb gezogen T3, EN AW-2007

ZEICHNUNGSNR. Klemmring Fanglager

A3

GEWICHT: 14g

MASSSTAB:2:1

BLATT 1 VON 1

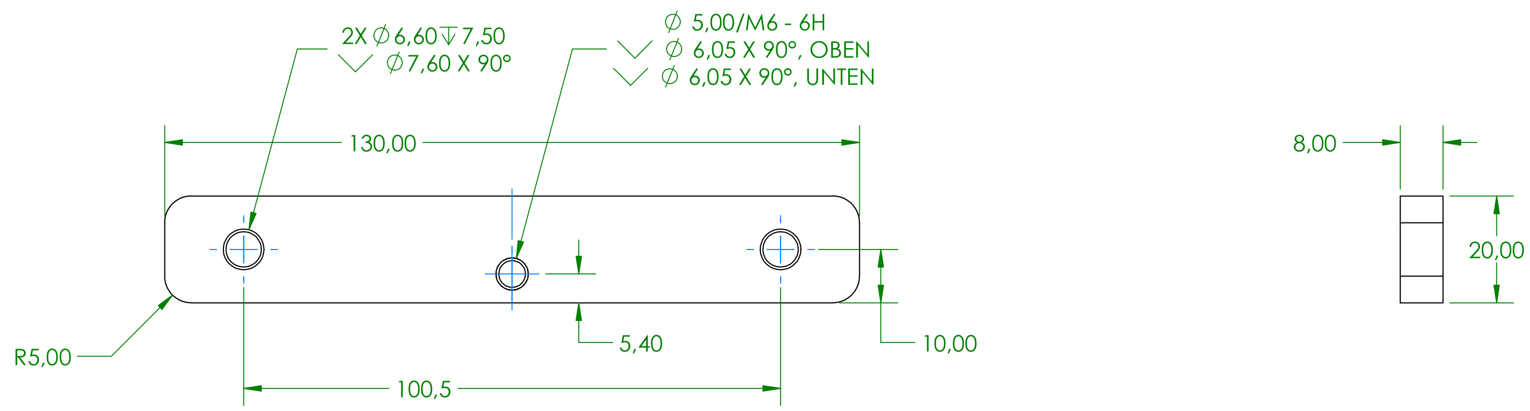

WENN NICHT ANDERS DEFINIERT:
BEMASSUNGEN SIND IN MILLIMETER
OBERFLÄCHENBESCHAFFENHEIT:
TOLERANZEN:
LINEAR: +/-0.1mm
WINKEL: +/-0.5°

OBERFLÄCHENGÜTE:

ENTGRATEN
UND SCHARFE
KANTEN
BRECHEN

ZEICHNUNG NICHT SKALIEREN

ÄNDERUNG

	NAME	SIGNATUR	DATUM
GEZEICHNET	MSO		
GEPRÜFT			
GENEHMIGT			
PRODUKTION			
QUALITÄT			

BENENNUNG:

WERKSTOFF:
AlMgSi0.5 Stab rechteckig
gepresst T66, EN AW-6060

ZEICHNUNGSNR.
Axialanschlag

A3

GEWICHT: 54g

MASSSTAB:1:1

BLATT 1 VON 1

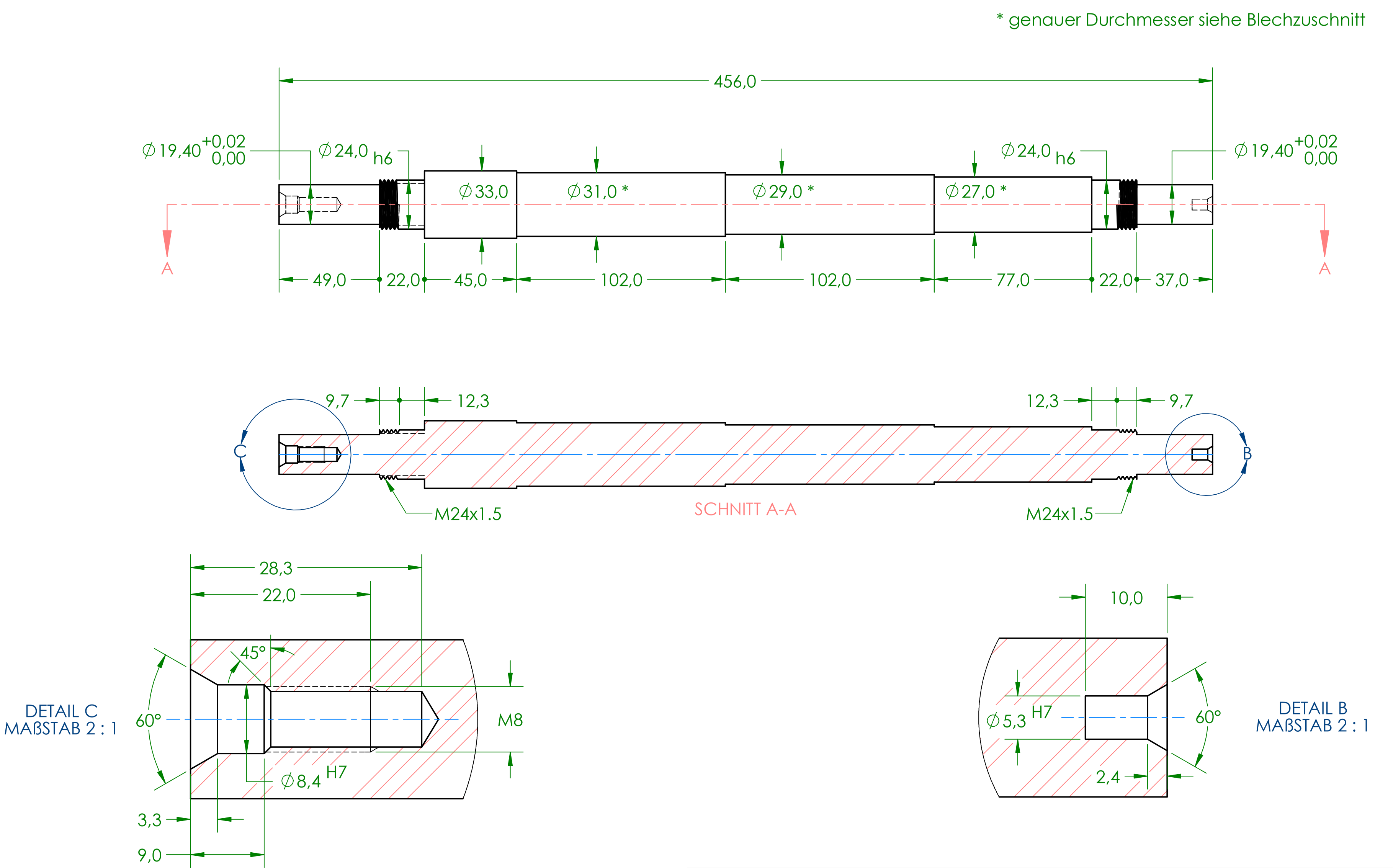

WENN NICHT ANDERS DEFINIERT:
BEMASSUNGEN SIND IN MILLIMETER
OBERFLÄCHENBESCHAFFENHEIT:
TOLERANZEN:
LINEAR:
WINKEL:

OBERFLÄCHENGÜTE:

ENTGRATEN
UND SCHARFE
KANTEN
BRECHEN

ZEICHNUNG NICHT SKALIEREN

ÄNDERUNG

	NAME	SIGNATUR	DATUM
GEZEICHNET	MSO		07.12.2023
GEPRÜFT			
GENEHMIGT			
PRODUKTION			
QUALITÄT			

BENENNUNG:

WERKSTOFF:
11SMnPb30/37
blankgezogen h9

GEWICHT: 2105g

ZEICHNUNGSNR.
Rotorschaft

A3

MASSSTAB:1:2

BLATT 1 VON 1

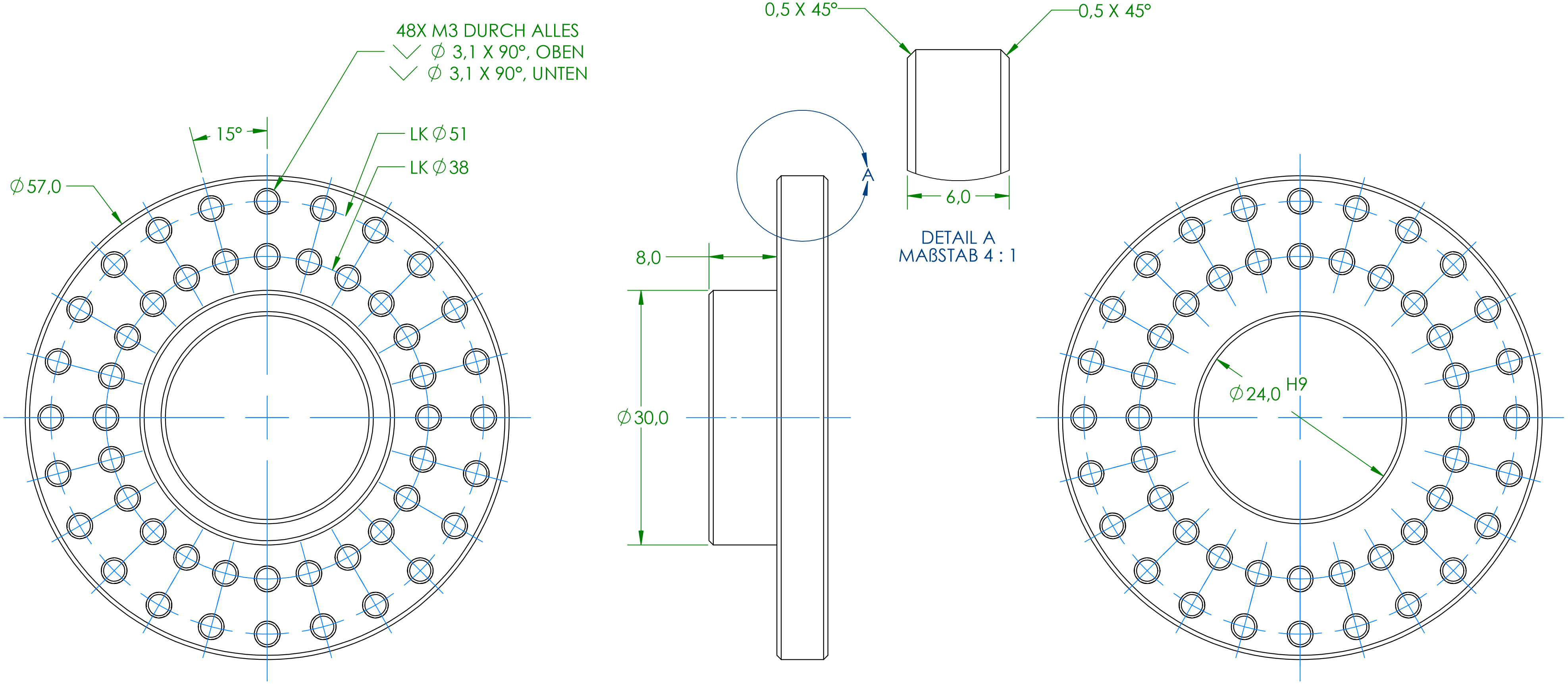

WENN NICHT ANDERS DEFINIERT:
BEMASSUNGEN SIND IN MILLIMETER
OBERFLÄCHENBESCHAFFENHEIT:
TOLERANZEN:
LINEAR: +/-0.1mm
WINKEL: +/-0.5°

OBERFLÄCHENGÜTE:

ENTGRATEN
UND SCHARFE
KANTEN
BRECHEN

ZEICHNUNG NICHT SKALIEREN

ÄNDERUNG

	NAME	SIGNATUR	DATUM
GEZEICHNET	MSO		
GEPRÜFT			
GENEHMIGT			
PRODUKTION			
QUALITÄT			

BENENNUNG:

WERKSTOFF:
AlCuMgPb
gezogen T3, EN AW-2007

ZEICHNUNGSNR.
Wuchtscheibe

A3

GEWICHT: 14g

MASSSTAB:2:1

BLATT 1 VON 1

List of Figures

References

[1] Eric H. Maslen and Gerhard Schweitzer. *Magnetic Bearings. Theory, Design, and Application to Rotating Machinery*. Springer Berlin, Heidelberg, 2009.

[2] Richard Spießberger. “Berechnung einer Synchron-Reluktanzmaschine für einen magnetgelagerten Antrieb”. Bachelor’s thesis, TU Wien. 2015.

[3] Robert Munnig Schmidt, Georg Schitter, and Adrian Rankers. *The Design of High Performance Mechatronics. High-Tech Functionality by Multidisciplinary System Integration*. 2nd. Delft University Press, 2014.

[4] Adalbert Prechtl. *Vorlesungen über Elektrodynamik*. TU Wien, 2012.

[5] Adalbert Prechtl. *Vorlesungen über die Grundlagen der Elektrotechnik. Band 2*. Springer Vienna, 2008.

[6] Felix Betschon. “Design Principles of Integrated Magnetic Bearings”. PhD thesis. 2000.

[7] Wan-Ying Huang et al. “Optimization of Magnet Segmentation for Reduction of Eddy-Current Losses in Permanent Magnet Synchronous Machine”. In: *IEEE Transactions on Energy Conversion* 25.2 (June 2010), pp. 381–387. URL: `https://centralesupelec.hal.science/hal-00491390`.

[8] Konstantina Bitsi, Damian Kowal, and Reza-Rajabi Moghaddam. “3-D FEM Investigation of Eddy Current Losses in Rotor Lamination Steel Sheets”. In: *2018 XIII International Conference on Electrical Machines (ICEM)*. 2018, pp. 1047–1053. DOI: `10.1109/ICELMACH.2018.8507048`.

[9] Wolfgang Demtröder. *Experimentalphysik 1. Mechanik und Wärme*. Springer-Verlag Berlin Heidelberg, 2013.

[10] Robert Gasch, Rainer Nordmann, and Herbert Pfützner. *Rotordynamik*. Springer-Verlag Berlin Heidelberg NewYork, 2006.

[11] Andreas Binder. *Elektrische Maschinen und Antriebe. Grundlagen, Betriebsverhalten*. 1st ed. Springer Berlin, Heidelberg, 2012. DOI: `https://doi.org/10.1007/978-3-540-71850-5`.

[12] Joachim Specovius. *Grundkurs Leistungselektronik. Bauelemente, Schaltungen und Systeme*. Vieweg+-Teubner Verlag Wiesbaden, 2010.

[13] Zaidong Hu. “A Common-leg Power Electronics Converter for Multi-axis Active Magnetic Bearing Drive”. In: *Proceedings of ISMB16* (2018).

[14] Kezhen Yang and Yefa Hu. “Evaluation of Switching Power Amplifier Topology for Active Magnetic Bearings”. In: *Actuators* 10.6 (2021). DOI: `https://doi.org/10.3390/act10060131`.

[15] Andreas Kugi. *Automatisierung*. Institut für Automatisierungs- und Regelungstechnik, TU Wien, 2023.

[16] *Messobjektdicke bei Wirbelstromsensoren*. Tech. rep. MICRO-EPSILON MESSTECHNIK GmbH & CO. KG, 2010.

[17] Regine Mallwitz. “Analyse von Wirbelstromsignalen mit problemangepaßten Funktionen für die zerstörungsfreie Materialprüfung”. PhD thesis. Universität Kassel, 1999.

[18] Markus Hutterer. “Regelung von magnetgelagerten Rotor für den Einsatz in Turbomolekularpumpen”. PhD thesis. 2018.

[19] *ISO 14839: Mechanical vibration — Vibration of rotating machinery equipped with active magnetic bearings. Part 3: Evaluation of stability margin*. Standard. Geneva, CH: International Organization for Standardization, Sept. 2006.

[20] David Trauner. “Entwurf und Vergleich verschiedener Unwuchtkompensationen für einen magnetgelagerten Rotor”. MA thesis. TU Wien, 2017.

Erklärung

Hiermit erkläre ich, dass die vorliegende Arbeit gemäß dem Code of Conduct – Regeln zur Sicherung guter wissenschaftlicher Praxis, insbesondere ohne unzulässige Hilfe Dritter und ohne Benutzung anderer als der angegebenen Hilfsmittel, angefertigt wurde. Die aus anderen Quellen direkt oder indirekt übernommenen Daten und Konzepte sind unter Angabe der Quelle gekennzeichnet.

Die Arbeit wurde bisher weder im In– noch im Ausland in gleicher oder in ähnlicher Form in anderen Prüfungsverfahren vorgelegt.

Wien, am 22.05.2025

Sonnleitner Markus